

Structures, Circuits and Architectures for Molecular Scale Integrated

Sensing and Computing

by

Constantin Pistol

Department of Computer Science
Duke University

Date: _____
Approved: _____

Alvin R. Lebeck, Advisor

Christopher Dwyer, Advisor

Alexander Hartemink

Jungsang Kim

Dissertation submitted in partial fulfillment of
the requirements for the degree of Doctor
of Philosophy in the Department of
Computer Science in the Graduate School
of Duke University

2009

ABSTRACT

Structures, Circuits and Architectures for Molecular Scale Integrated

Sensing and Computing

by

Constantin Pistol

Department of Computer Science
Duke University

Date: _____

Approved: _____

Alvin R. Lebeck, Advisor

Christopher Dwyer, Advisor

Alexander Hartemink

Jungsang Kim

An abstract of a dissertation submitted in partial
fulfillment of the requirements for the degree
of Doctor of Philosophy in the Department of
Computer Science in the Graduate School
of Duke University

2009

Copyright by
Constantin Pistol
2009

Abstract

Nanoscale devices offer the technological advances to enable a new era in computing. Device sizes at the molecular-scale have the potential to expand the domain of conventional computer systems to reach into environments and application domains that are otherwise impractical, such as single-cell sensing or micro-environmental monitoring.

New potential application domains, like biological scale computing, require processing elements that can function inside nanoscale volumes (e.g. single biological cells) and are thus subject to extreme size and resource constraints. In this thesis we address these critical new domain challenges through a synergistic approach that matches manufacturing techniques, circuit technology, and architectural design with application requirements. We explore and vertically integrate these three fronts: a) *assembly methods* that can cost-effectively provide nanometer feature sizes, b) *device technologies* for molecular-scale computing and sensing, and c) *architectural design* techniques for nanoscale processors, with the goal of mapping a potential path toward achieving molecular-scale computing.

We make four primary contributions in this thesis. First, we develop and experimentally demonstrate a scalable, cost-effective DNA self-assembly-based fabrication technique for molecular circuits. Second, we propose and evaluate Resonance Energy Transfer (RET) logic, a novel nanoscale technology for computing based on single-molecule optical devices. Third, we design and experimentally demonstrate selective sensing of several biomolecules using RET-logic elements. Fourth, we explore the architectural implications of integrating computation and molecular sensors to form nanoscale sensor processors (nSP), nanoscale-sized systems that can sense, process, store and communicate molecular information. Through the use of self-assembly manufacturing, RET molecular logic, and novel architectural techniques, the smallest nSP design is about the size of the largest known virus.

Contents

Abstract	iv
List of Tables	ix
List of Figures	x
Acknowledgements	xii
1 Introduction	1
1.1 Molecular Assembly.....	2
1.2 Nanoscale Computing and Sensing Technology	3
1.3 Architectural Design of Nanoscale Sensor Processors	4
1.4 Thesis Contribution and Organization.....	4
2 Nanoscale Structures for Circuit Substrates	6
2.1 Design Automation for DNA Self-Assembled Nanostructures.....	8
2.1.1 DNA Self-Assembly	9
2.1.1.1 Thermodynamics	10
2.1.1.2 Sequence Design	11
2.1.2 DNA Motifs	11
2.1.3 Metrics and Design Rules	13
2.1.3.1 Metrics.....	13
2.1.3.2 Design Rules.....	15
2.1.3.3 Corrugation.....	15
2.1.3.4 Thermal Ordering.....	16
2.1.4 Target Nanostructure.....	16
2.1.5 Design Automation Methods	18
2.1.5.1 Thermodynamic Optimization Tool	19

2.1.5.2	Alternative Designs	21
2.1.6	Analytic Evaluation.....	24
2.1.7	Experimental Evaluation.....	31
2.1.8	Summary	31
2.2	Scalable, Low-cost, Hierarchical Assembly of Programmable DNA Nanostructures .	32
2.2.1	Generic linkers	34
2.2.2	Fully specific linkers.....	35
2.2.3	Polymer-mediated connectivity	37
2.2.4	Chemically programmable structures.....	38
2.2.5	Experimental Procedures	40
2.3	Conclusion.....	42
3	Nanoscale Optical Circuits using RET Logic	44
3.1	Resonance Energy Transfer Logic	46
3.1.1	Resonance Energy Transfer	47
3.1.2	Gates.....	49
3.1.3	Wires	52
3.2	Integrated RET Technology	54
3.2.1	Insulators	54
3.2.2	Signal Restoration: Energy Supply and Feedback	54
3.2.3	Memory cells.....	56
3.2.4	Decoders, Multiplexers and Adders.....	57
3.2.5	Macroscale Input /Output.....	57
3.3	Analysis	58
3.4	Application Domains.....	60
3.5	Towards a prototype	61

3.6	Related Work.....	63
3.7	Conclusion.....	64
4	Nanoscale Sensing	66
4.1	Resonance energy transfer.....	67
4.2	DNA self-assembled RET circuits	70
4.3	RET logic gates and sensing.....	71
4.4	Underlying mechanism for sensing.....	79
4.5	Scaling to larger circuits.....	81
4.6	Related Work.....	83
4.7	Conclusion.....	84
5	Nanoscale Sensor Processors	85
5.1	Enabling Technology.....	87
5.1.1	RET-logic Circuits	89
5.1.2	RET-based Sensing	90
5.1.3	Preliminary Experimental Results.....	90
5.2	nSP Applications	91
5.3	An nSP Architecture.....	96
5.3.1	Qualitative Architectural Implications	96
5.3.2	nSP Overview.....	97
5.3.3	Integrated Sensing.....	98
5.3.4	The nSP ISA.....	99
5.3.5	Discussion	102
5.4	Evaluation.....	102
5.4.1	Node Size	102
5.4.2	Program Size	103

5.4.3	Impact of Instruction-Fused Sensing.....	105
5.4.4	Application Simulation Results.....	108
5.5	Related Work.....	111
5.6	Conclusion.....	112
6	Conclusion	114
6.1	Thesis Summary	114
6.2	What's Next?.....	115
Appendix A		118
A.1	Optical Gates	118
A.1.1	Chromophore functionalization.....	118
A.1.2	Gate configuration on 4x4 grid.....	119
A.1.3	DNA sensing gates and target analytes	120
A.1.4	RNA sensing gate and target analytes	121
A.1.5	Protein sensing gate and target analytes.....	121
A.2	Sensing	122
A.2.1	Melting: increasing binding site accessibility	123
A.2.2	Sensing procedure	124
A.2.3	Impact of structural configuration on sensing	125
A.2.4	Grid concentration	127
A.3	Data Fit	127
References		130
Biography		139

List of Tables

Table 2-1: 20-Arm and 96-Arm results. *No 96-arm original exists.....	25
Table 2-2: Upper bounds on TLM and SEM with 5-nt sticky-ends	26
Table 2-3: The best 160x5-nt arm sequences found by AB-Core method.....	30
Table 3-1: Parameters that impact RET efficiency.....	48
Table 3-2: RET path model.....	59
Table 3-3: Estimate node power consumption.....	60
Table 3-4: Observed RET output.....	63
Table 5-2: Our nSP ISA.....	100

List of Figures

Figure 2-1: Schematic of a cruciform composite motif	12
Figure 2-2: 4x4 grid with 16 cruciform tile motifs	16
Figure 2-5: The arm-less motif	23
Figure 2-6: AB Core, AB Split Passive, random and original 20-arm sets	27
Figure 2-7: Specificity in arm space with different fixed seq. sets	28
Figure 2-8: a) B-only, AB Cores and Random for 96-arm sets b) AB Cores and AB Split Passive SF 0.7	28
Figure 2-9: Trade-off: specificity can be traded for stability	29
Figure 2-10: 20-arm designs balanced for TLM and SEM metrics	29
Figure 2-11: AFM image of a) single DNA grid and b) typical deposition of multiple grids	31
Figure 2-12. The hierarchical approach	33
Figure 2-13. (a) Schematic and (b) AFM image of a two-grid (4x8) assembly	34
Figure 2-14. (a) An AFM scan of the 2x2 array of grids.	36
Figure 2-15. Histogram of identifiable structures as observed by AFM (N=73)	36
Figure 2-16. Histogram of un-identifiable structures as observed by AFM (N=43)	36
Figure 2-17. AFM image of grids connected by polymer track	38
Figure 2-18. AFM images of streptavidin patterned 4x4 DNA grids. Scale bar is 20 nm.	39
Figure 2-19. AFM scans of 4x4 DNA grids with bound streptavidin	39
Figure 2-20. AFM images of SA line patterns on 4x4 DNA grid	40
Figure 3-1: Transition energy diagram and expression for RET.	47
Figure 3-2: Schematic of inverting pass-gate using RET.	50
Figure 3-3: Plot of pass gate input-channel-output transfer efficiency	51
Figure 3-4: Schematic of AND, OR and NOT gates	52
Figure 3-5: Schematic of (a) a 3-step RET cascade and (b) a RET/EM wire on a DNA grid.	53

Figure 3-6: Set of RET gates including restoration gate R for feedback and energy supply.....	55
Figure 3-7: Memory latch 20nm x 40nm (left) and memory cell 40nm X 60nm (right)	56
Figure 3-8: (a) MUX4 40nm x 60nm (b) DEC2-to-4 40nm x 60nm (c) 1-bit FA 20nm x 20nm ..	57
Figure 3-9: Latency and power dissipation analysis.....	58
Figure 3-10: AFM images of DNA grids patterned with chromophore-functionalized proteins...	61
Figure 3-11: Schematic of OR gate.	62
Figure 4-1: Cruciform tiles.	70
Figure 4-2: Chromophores are attached to 5' and 3' ends of shell strands.....	72
Figure 4-3: Sensing process overview	73
Figure 4-4: Two AND-gate response across DNA, RNA, and protein analytes.....	77
Figure 4-5: Sensitivity to various analyte concentrations.	78
Figure 4-6: Fitting results.....	81
Figure 5-1: RET logic circuit layouts on DNA substrate.....	89
Figure 5-5: Code size impact of IFS on the multi-analyte probe.....	106
Figure 5-6: Impact of using IFS on the memory requirement of target nSP applications.	106
Figure 5-7: Comparison of IFS and LD/ST implementations of applications.....	107
Figure 5-8: Influenza-A virus counting simulation.	109
Figure 5-10: Multi-analyte probe simulation.....	111

Acknowledgements

Throughout my PhD studies I received the support, friendship and guidance of many people. I now have a chance to thank them.

First, and most important, is my fiancée Anita. Her encouragement and support was always with me.

My parents and my brother were a continuous source of help and encouragement.

My advisors, Alvin Lebeck and Chris Dwyer, provided guidance and inspiration at each step of my PhD. I am grateful that I had the opportunity to have them as mentors.

I would like to thank Dan Sorin, Alex Hartemink and Jungsang Kim for advice and support throughout most of graduate studies.

My colleagues Jaidev Patwardhan, Albert Meixner and Vincent Mao were the source of many stimulating conversations and a great sounding board for ideas.

Finally, the members of the Duke Computer Architecture group provided support, open discussions and valuable feedback with many unique perspectives.

1 Introduction

Two driving forces on computer architecture are technology change and application requirements. Nanotechnology is an example of technological advance with the potential to enable a new era in computing. Device sizes at the molecular-scale can provide computer architects with a plethora of devices to utilize (e.g., for million core designs) in traditional computing applications. At the same time, new application domains can emerge when a significant amount of computational circuitry can be placed in an area smaller than a typical biological cell.

An example of a potential new computation domain is in the life sciences, where understanding molecular scale phenomena is a critical component and the diversity of molecular components and interaction dynamics within environments like a cell make it difficult to monitor and quantify the underlying processes. The ability to utilize programmable devices at molecular scales may enable life scientists to perform hypothesis testing previously thought impossible or prohibitively expensive to do with traditional techniques like molecular probe methods, which require costly equipment, highly specialized training and can often span several days [92]. For example, at home early disease detection could be achieved with a low-cost device capable of monitoring important markers of bioactivity and cellular health, such as concentrations of specific proteins or small messenger RNA molecules [23].

To enable new application domains like biological scale computing, processing elements must be capable of functioning inside nanoscale volumes (e.g. single biological cells). This requirement places extreme constraints on processor size, power, communication, and sensing capabilities. The hypothesis we explore in this thesis is that it is possible to address these critical constraints, and thus enable new computing domains, through a synergistic approach that combines innovations in manufacturing techniques, circuit technology, and architectural design.

We explore and vertically integrate three fronts: a) *assembly methods* that can cost-effectively support meaningfully complex circuits with nanometer feature sizes, b) *device technologies* for molecular-scale computing and sensing, and c) *architectural design* techniques for nanoscale processors, with the goal of mapping a potential path toward achieving molecular-scale computing.

1.1 Molecular Assembly

The self-assembly of nanoscale logic circuits has great potential as an economical and massively parallel method to create computer systems. In the future self-assembly techniques can play an increasingly important role in technology as the resolution and manufacturability of current microelectronics processes begin to reach fundamental limits. DNA is an attractive substrate to investigate for applications in molecular-scale computing because it can form controlled, precise nanostructures. The binding rules that govern DNA self-assembly enable the creation of nanostructures with a minimum pitch of a few nanometers. Further, these nanostructures can organize active circuit components with molecular-scale precision. Thus, DNA self-assembly has the potential to expand the domain of conventional computer systems to reach into nanoscale environments.

To support nanoscale computing systems, can we cost-effectively make DNA substrates that are both chemically addressable at molecular level and also sufficiently large to organize complex circuits? Complex designs are often created hierarchically, using a relatively small set of common building blocks. Using this design principle, we propose a scaleable, hierarchical assembly method that can create complex aperiodic DNA structures while keeping the assembly cost low through the reuse of building blocks. This method uses DNA design automation and thermodynamic analysis techniques to increase the probability of assembling correct structures. We validate the method experimentally by assembling a 140nmx140nm DNA grid, one of the

largest aperiodic synthetic nanostructures ever synthesized, and demonstrate the nanoscale substrate capability of aperiodic DNA grids by assembling arbitrary circuit-type patterns of small molecules.

1.2 Nanoscale Computing and Sensing Technology

A scalable, cost-effective molecular-scale fabrication technique is necessary, but not sufficient to achieve molecular-scale computing. The fabrication method must be accompanied by the appropriate molecular-scale active devices that enable computation and sensing.

There are many examples of nanotechnology devices (e.g. carbon nanotubes, silicon nanorods, DNA/enzymatic reactions) that can provide both a logic system and sensing ability. However, the overall system must also provide appropriate abstractions for computing. For instance, we need to consider how well the target technology enables wires, gates, and insulators and facilitates input and output to the macroscale. Also, are the power supply and the power delivery compatible with the target applications? Using the nanometer-placement capabilities of self-assembly fabrication methods, we propose a new nanoscale device based on Resonance Energy Transfer (RET), a single-molecule optical phenomenon. We show how RET devices address the above challenges and enable a complete integrated technology for computing and sensing with wireless power delivery and I/O signals. The experimental demonstration of RET devices includes a sample sensing method which uses RET gates to detect biomolecules in small volumes at the nanoscale. The assembled circuits can detect femtomole quantities of label-free biomolecules like proteins and short fragmentary nucleic acids in solution. This method, which creates up to twenty-four 8-nm^3 logic gates on a $60\text{nm} \times 60\text{nm}$ DNA grid, is a scalable step toward nanoscale logic capable of interfacing computers with biological processes.

1.3 Architectural Design of Nanoscale Sensor Processors

Nanotechnology only provides the potential to create appropriately sized processors. To meet the severe size constraints of new domains, like biological scale computing, even molecular logic systems must be carefully architected.

There are many questions to consider in this design process. How are the application characteristics, coupled with the small size requirement, influencing the architectural design space of nanoscale processors? Is general-purpose computation desirable for nanoscale processors? Are traditional architectural trade-offs changing with the shift to nanoscale? In this context we explore the architectural implications of integrating computation and molecular probe sensors to form nanoscale sensor processors (nSP). nSPs are nanoscale sized systems that can sense, process, store, and communicate molecular information. We present an nSP design that includes a simple accumulator-based instruction set architecture, sensors, limited memory, and communication transceivers. Furthermore we show how nSPs enable new computing domains and automate classes of life-sciences applications that currently require expert scientific training and costly equipment. Through the use of DNA self-assembly manufacturing, RET molecular digital logic, and novel architectural techniques, like instruction-fused sensing, the smallest nSP design is about the size of the largest known virus.

1.4 Thesis Contribution and Organization

The main goal of this thesis is to map a potential path toward achieving molecular-scale computing. We make the following primary contributions:

1. we develop and experimentally demonstrate a scalable, cost-effective DNA self-assembly-based fabrication technique for molecular circuits,
2. we propose and evaluate RET-logic circuits, a novel nanoscale technology for computing based on single-molecule optical devices,

3. we design and experimentally demonstrate selective sensing of several biomolecules using RET-logic on DNA substrate, and

4. we explore the architectural implications of integrating computation and molecular sensors to form nanoscale sensor processors (nSP), nanoscale-sized systems that can sense, process, store and communicate molecular information.

This thesis is organized as follows. In Chapter 2 we provide background on DNA-based self-assembly and describe the design and experimental validation of a scaleable, fully programmable DNA grid substrate. In Chapter 3 we propose and evaluate RET-Logic, a candidate digital logic technology based nanoscale optical phenomena. In Chapter 4 we detail and experimentally demonstrate a method of sensing various biomolecules using RET-Logic gates integrated on self-assembled DNA grids. In Chapter 5 we explore the architectural design space for nanoscale sensor processors (nSP) and we conclude in Chapter 6.

2 Nanoscale Structures for Circuit Substrates

The application of nanoscale phenomena in photonic and electronic devices is widely considered to be an important development for the future of computer systems. However, few methods exist that can organize nanoscale and molecular components with the control and degree of asymmetry required to yield usefully complex circuit topologies in a scalable and low-cost manner.

Conventional top-down fabrication techniques are costly and increasingly complex. Scalable lithographic techniques require costly manufacturing lines and achievable feature sizes are still orders of magnitude from molecular resolution. Sub-nanometer manufacturing precision can be attained with methods that use scanning probe microscopes to move individual atoms one at a time; however such methods are expensive, time-intensive and scale poorly with the number of devices to be assembled.

Bottom-up chemical self-assembly techniques are a promising alternative that require less energy and time to create complex molecular patterns. Furthermore, self-assembly enables fabrication through composition and hierarchies. Different types of molecules can be fabricated independently using the most cost-effective method for each type of molecule. Larger molecular motifs can then be created through the composition of heterogeneous molecules.

DNA and RNA have gained popularity as a material system for creating complex, aperiodic nanostructures with bottom-up techniques due to the ease with which these materials can be synthesized and controlled [15, 22, 46, 59, 64, 72]. The precise binding rules of DNA enable creation of nanostructures with minimum pitch on the order of a few nanometers which can be used to place and interconnect active nanoscale components (e.g., optical chromophores, crossed carbon nanotube FETs, ring-gated FETs, nanowires) with molecular-scale precision. The

ability to organize active circuit elements in precise configurations makes DNA an attractive substrate to investigate for applications in molecular-scale computing.

In this chapter we explore the potential of DNA structures to provide scaffolding for the assembly of molecular scale circuits and sensors. This target application requires an assembly method that is cost-effective, can scale to large-size designs and provides full chemical addressability in the resulting structures. We propose a method that is a low cost synthetic mechanism because of motif and strand re-use, can achieve through hierarchical motifs the fabrication of larger programmable structures than have been previously demonstrated by tile- or motif-based methods and provides full chemical programmability that enables the assembly of arbitrary circuit patterns.

In Section 2.1 we show how we apply design automation techniques to generate optimized sequences for the experimental assembly of a fully programmable 60nm x 60nm DNA grid substrate. The grid can be “functionalized” (i.e., arbitrary single molecules can be attached) at several locations near each intersection in a fully “addressable” manner (i.e., each location is chemically distinct and thus “programmable”). In Section 2.2 we extend this method and leverage sequence re-use in a hierarchical fashion to reduce the cost of fabrication by building larger complexes from smaller precursors. We assemble a fully programmable 8,960 kD molecular weight 140nm x 140nm DNA grid, one of the largest synthetic nanostructures ever synthesized, demonstrate the chemical programmability of DNA grids by creating arbitrary circuit-type patterns of small molecules (proteins), and show that it is feasible to scale this method further for circuit substrate applications in complex nanoscale system fabrication.

2.1 Design Automation for DNA Self-Assembled Nanostructures

The challenge in creating DNA nanostructures is to specify the appropriate DNA sequences such that the desired structure (geometry) forms and is thermodynamically stable. Double stranded DNA is stable when the base pairs are “complementary”, i.e., if A pairs with T and G pairs with C. The central theme in applied self-assembly is to exert control over an otherwise spontaneous reaction to direct its outcome [100]. This control directs the assembly of materials into structures that are interesting and relevant to a given application. We can control the reaction by designing synthetic DNA strands to interact at specific temperatures (called melting temperatures) by careful choice of their base sequences. Specification of the strand sequences can create a specific topology through base complementarity and the ability of DNA strands to fold (e.g., like tying a knot). Thus, sequence design is important because the interaction between strands must be thermodynamically favorable and result in a specific topology.

To meet the sequence design challenge DNA self-assembly can exploit the common technique of composing a small set of relatively simple motifs to create more sophisticated structures. Many parts of this design process can benefit from design automation. However, in this work we focus on the key aspect of designing the DNA sequences that control how motifs can bind with each other. Specifically, we seek to find DNA sequences that minimize the strength of unintentional interactions with the other motifs in the set while maximizing the strength of intentional interactions.

In this section we present our approach to evaluate the sequence design space to create a fixed size, 60nm X 60nm grid with 20nm pitch. This structure is composed through a hierarchical assembly of motifs. We focus on the design of the final assembly step that combines 16 cruciform tile motifs (arranged 4x4) to form the final grid structure. For this structure, we must

determine the best 96 sequences that satisfy the structural and stability metrics. To accomplish this we implemented an optimization algorithm that is aware of both intentional and unintentional interactions and exploits parallelism to rapidly evaluate the large sequence design space.

We have experimentally verified our method by designing, synthesizing, and assembling the target nanostructure and characterizing it with atomic force microscopy (AFM). We also show that our optimization algorithm produces superior sequences for a 2x2 grid than sequences produced using conventional text-based sequence comparison or random sequence selection.

We start with a brief background on DNA Self-Assembly and DNA motifs before describing in more detail our target nanostructures and the metrics we define for self-assembling DNA designs.

2.1.1 DNA Self-Assembly

DNA is an acronym that stands for a class of chemicals known as deoxyribonucleic acids and is widely studied in the context of molecular genetics. We are concerned primarily with DNA as a substrate for fabricating nanostructures, and thus provide a brief review in this context.

DNA's basic building blocks—called a nucleotide—are composed of a phosphodiester covalently bound to a nucleoside or a derivative of a deoxyribose sugar and either a purine or pyrimidine nucleobase. The nucleobases commonly used in DNA self-assembly are the purines: adenine (A) and guanine (G), and the pyrimidines: thymine (T) and cytosine (C). The nucleotides bind to each other to form a linear chain through the phosphodiester bonds. This represents a so-called single-stranded DNA molecule.

Single strands of DNA with custom sequences are synthesized using a cyclic process in which nucleobases are added one by one starting from the 3'-end. The first base is covalently attached to a solid support. The next base is added through a four-step chemical reaction (deblocking, base condensation, capping and oxidation). The process is repeated until the

complete sequence is synthesized. The strands are then detached from the solid support and purified according to their length. Each cycle is approximately 98-99% efficient and commercially available DNA synthesizers can efficiently assemble single strands 100-150 nucleobases long.

Single strands can wrap around each other to form the well-known helical structure, or double stranded molecule (i.e., a double helix). The double stranded DNA structure is most stable when the pairwise nucleobase interactions are “complementary”, i.e., if A pairs with T and G pairs with C. Under these conditions each base pair (bp) is approximately 2 nm wide (diameter of the helix) and on average 0.34 nm long (along the strand, per base). The helical twist of the two strands (in the most common form) is such that a full turn occurs between every 10th and 11th base. Further, the stability of this interaction is only approximately linear per base and depends on neighboring mismatch or complementary interactions [63]. The stability and exact dimensions, orientation, and form of the nucleobase interaction depend on several factors including the pH of the solution and local properties of the DNA.

2.1.1.1 Thermodynamics

The central theme in the use of static self-assembly for nanoscale fabrication is the application of an external control over an otherwise spontaneous reaction to direct its outcome [100]. This control directs the assembly of materials into structures that are interesting and relevant to a target design problem. In the context of computer system fabrication the self-assembly is used to direct the formation of switching devices (e.g., transistors and wires) to create logic circuitry, memory, and I/O interfaces.

The temperature of the reaction volume (i.e., the solution) is a simple control in DNA self-assembly. This follows from the experimental evidence that demonstrates the formation of double helices from single strands of complementary DNA as the solution temperature is changed

from high to low. The melting temperature (T_m) of a DNA strand is the temperature at which the transition from single strands to double strands has reached 50%. That is, half of the single strands in solution are bound to their complementary strand when the solution temperature is exactly the melting temperature of the strand. The T_m of two strands is dependent on their sequences and the degree to which they are complementary. This simple picture is complicated by the introduction of multiple sequences in solution. Further, the time evolving dynamics of these interactions are still under study [98]. It is the richness of this interaction that is at the root of why DNA can be used to form complex nanostructures.

2.1.1.2 Sequence Design

A strand of DNA obeys certain thermodynamic behavior, most importantly that double strands form at temperatures below the T_m of the constituent single strands, and this interaction can be complex if multiple unique (sequences) DNA strands are in solution. Specification of the strand sequences provides external control over the self-assembly process (through temperature control) and determines the formation of structures (through complementarity). Good sequence design leads to a minimization of sequence mismatches, or unintentional interactions between strands of similar but not perfectly complementary sequences, at a given temperature and therefore produces a higher yield of the target structures.

Sequence design is important because it determines many aspects of the target DNA nanostructure (e.g., geometry and stability). Therefore it is critical to have good methods for choosing sequences. One approach is to use abstractions to create increasingly sophisticated structures.

2.1.2 DNA Motifs

Complex designs are often created using a relatively small set of common building blocks—called motifs. DNA self-assembly can exploit this same design principle to

hierarchically create more sophisticated aperiodic structures. For DNA there are many possible motifs, however we focus on only a few in the context of our target nanostructure (see Section 2.1.4). Motifs include junctions that enable three or more double stranded helices of DNA to interact and thus form specific structures (e.g., a triangle, a corner, etc.) Another important motif is a single strand of DNA protruding from a double stranded helix—called a sticky-end.

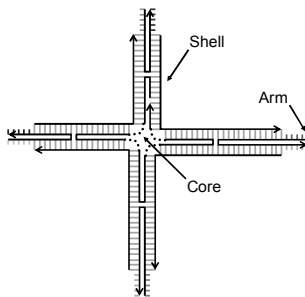


Figure 2-1: Schematic of a cruciform composite motif

Two motifs with complementary sequences on their sticky-ends will bind to form a composite motif. These composite motifs may also have embedded sticky-end motifs and thus can also bind with other composite motifs to form another, larger, composite motif. This results in a hierarchical structure for motifs.

The cruciform tile motif is composed from three smaller motifs: a core, 4 shells, and 4 arms each with two 5-nucleotide (5-nt) sticky-ends. Figure 2-1 shows a schematic of the cruciform motif.

Although motifs provide an easy abstraction for reasoning about DNA nanostructures, there are many potential issues related to sequence dependent physical (structural) properties. For example, the cruciform tile motif has a slight curvature in three-space, thus composite motifs formed with this motif must account for this curvature to ensure the desired final geometry is formed. Furthermore, the structural properties of DNA sequences can create strain in the final structure which can prohibit proper formation.

There are many design considerations that must be accounted for in creating a DNA nanostructure. When combined with the vast sequence space, these considerations motivate the need for computer aided design methods.

2.1.3 Metrics and Design Rules

The number of possible nanostructures that can be fabricated by motif-based DNA self-assembly is large. However, not all nanostructures can be synthesized efficiently due to the geometric and thermodynamic limitations of DNA hybridization. Such limitations require a set of experimentally verified design rules to act as templates for new designs. In this section we describe the metrics and design rules we have used to design and evaluate new nanostructures.

2.1.3.1 Metrics

Metrics enable meaningful comparisons between designs and when coupled with baseline or reference designs can be used to predict fabrication yields. Experimental data indicates that these metrics are correlated with high yields. The two metrics we use to evaluate a design are: (i) the average single-interaction energy measure (SEM) and (ii) the target-interaction likelihood measure (TLM).

SEM— The average single-interaction energy measure is an estimate of the thermal stability of the motif interactions in a design. The SEM can be used as a relative measure of stability in terms of temperature.

$$SEM_{set} = \frac{\sum_{i=1}^N T_m[seq_i, comp(seq_i)]}{N}, \text{ where } T_m \text{ is the nearest-neighbor melting}$$

temperature as function of the nucleotide sequence seq_i and its complement $comp(seq_i)$.

For example, a design with a large SEM will be stable at higher temperatures than a design with a low SEM. The SEM is calculated by averaging the melting temperature of each

interaction between the motifs in a design. Therefore, a large SEM indicates that the average interaction strength between motifs is also large.

While the thermal stability of a structure is important it is clear that if the structure forms incorrectly, yet with high stability, the fabrication process will produce a large fraction of flawed or defective structures. Therefore, a measure of how likely a structure will form must be coupled with the SEM to obtain a complete measure of the assembly process.

TLM— The cross-interaction likelihood measure is an estimate of the potential for a design to assemble a correct structure. The larger this value the less likely it is that a design will form incorrectly. This metric is calculated as the average distance from the diagonal on a non-specific vs. specific melting temperature plot for each motif against all other motifs. Motifs that are close to the diagonal (i.e., motifs with strong non-specific interactions) should be avoided since they will likely contribute to the formation of defective structures. This metric will always be positive.

$$TLM_{set} = \frac{\sum_{i=1}^N \max\{T_m[seq_i, seq_j] \mid j = 1..S \wedge i \neq j\}}{N}, \text{ where } S \text{ is the upper index of the}$$

sequences to consider within the current set.

Thus, the SEM and TLM are metrics that enable a consistent thermodynamic framework in which to compare candidate designs. However, they do not provide insight into the geometric or structural quality of a design. The complexity of this problem motivates the use of design rules in choosing the structure and assembly order for a design. The design rules provide a template for the creation of structures from motifs and can guarantee geometric properties when the design is fabricated.

2.1.3.2 Design Rules

We have identified two design rules that enable the fabrication of complex nanostructures. The first is the use of a “corrugation” scheme that alternates the direction of each motif’s normal vector across the structure. The second design rule describes a “thermal ordering” of motif interactions based on melting temperatures and the desired structure.

2.1.3.3 Corrugation

The term “corrugation” was first introduced by Liu et al. [50] to describe a method to combat a curling effect observed in large periodic nanostructures. Each motif has an intrinsic curvature that is sequence dependent and may or may not be approximately zero. Further, the curvature can generate a strained structure if a curved motif is forced (by adjacent motifs) into a planar shape.

A sufficiently large accumulation of strain along a vector that crosses the structure can curl the structure into a tubule. To avoid this strain the corrugation design rule specifies that motifs must be placed into the structure with alternating normal vectors such that their sum over the entire structure is minimal. Regardless of the curvature (or lack thereof) in the motif, the accumulation of strain can be minimized by symmetrically arranging motifs in this way. For example, consider a linear array of identical motifs each with some positive curvature. The structure will curl on itself if the motifs are aligned with each other. Instead, if the motif alignment alternates they will form a straight line.

We have generalized this rule for 2D planar structures and apply it as a template for new designs. The remaining design task (Section 2.1.5) is to render the generic template into real nucleotide sequences that can be used to fabricate the target structure. While the corrugation design rule will ensure that the resulting structure is planar, we have found that the order in which

motifs assemble into the final structure plays a significant role in the defect rate of the fabrication process. This has led us to apply a second design rule that specifies the motif assembly order.

2.1.3.4 Thermal Ordering

The DNA of each motif has a specific melting temperature below which an interaction (with other motifs) can take place and will be stable. These melting temperatures (estimated by the SEM) can be ordered from high to low and used as a criterion for picking a given arm sequence and motif. Since we can physically constrain the assembly temperature to be monotonically decreasing we can control the order in which motifs will assemble by choosing sequences with descending SEMs.

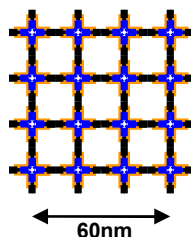


Figure 2-2: 4x4 grid with 16 cruciform tile motifs

Similar to the corrugation design rule, the thermal ordering design rule provides a template (in this case an assembly order) for the nanostructure and must ultimately be rendered into real nucleotide sequences. In the next section we describe our target nanostructure and how the metrics and design rules are applied.

2.1.4 Target Nanostructure

For the design target, consider a planar grid of motifs like the ones shown in Figure 2-1. The cruciform tile motif described in Section 2.1.2 is the basic element for the grid and the design must completely specify the nucleotide sequence for each motif. Using the hierarchical strategy

we can reduce the complexity of this problem by using known nucleotide sequences for the cruciform motif and focus on the arm sequences.

A 4x4 grid (see Figure 2-2) has 16 cruciform tile motifs and each cruciform requires four pairs of sequences (one pair for each arm per motif). Since the motifs only bind on the interior of the grid a total of 96 arm sequences are required (96-arm). Prior work has been limited to periodic structures where as many as four or five motifs polymerize into 2D arrays; such systems require fewer arm sequences due to the periodic reuse of motifs [105]. A classic example of this is the “AB” system that requires 20 distinct arm sequences for 2 motifs (20-arm). The sequences in the 96-arm system must be designed to ensure that each tile motif will bind in only 1 of 16 positions in the grid. We can apply the corrugation and thermal ordering design rules as templates for the grid at the outset and use the SEM and TLM estimates to choose from all candidate arm sequences. Figure 2-3 and Figure 2-4 show the specific design rules we use for the 4x4 grid.

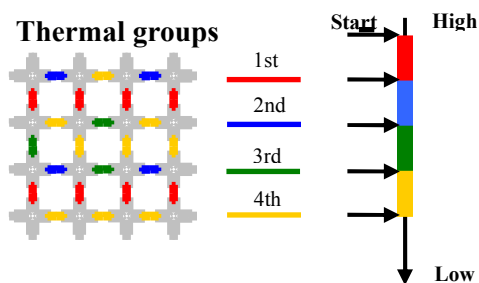


Figure 2-3: Thermal ordering design rule for the 4x4 grid

The thermal ordering design rule partitions the internal sticky-ends into four thermal groups based on their SEM (melting temperature with their target complements). The four groups are ordered high to low, with the first group having the highest SEM (most stable) and the fourth having the lowest (least stable). By controlling the reaction temperature process we can induce a level of order in the assembly of the 4x4 grid. As the annealing temperature drops the interactions inside different thermal groups become thermodynamically stable and cruciform motif monomers

can successively form stable dimmers, tetramers and more complex structures up to the final 4x4 grid.

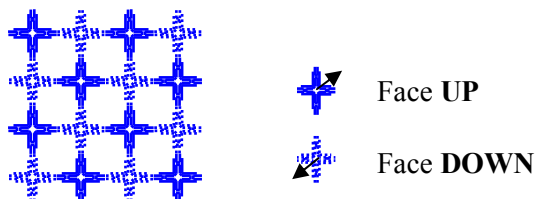


Figure 2-4: Corrugation design rule for the 4x4 grid: motif normals are alternated in both x and y coordinates

The corrugation design rule ensures planarity of the grid by alternating cruciform motif normals in both vertical and horizontal directions. The inherent cruciform motif curvature cancels out over the length of the 4x4 grid.

To maintain an optimal solution we evaluate all possible 5-nt sticky-end arm sequences. Section 2.1.5 describes the sequence design process in detail and Section 2.1.6 evaluates the designs.

2.1.5 Design Automation Methods

Given the importance of sequence design for self-assembled systems there are a variety of available tools for this purpose [26, 38, 77, 82, 106]. However, these tools use heuristics, simplified interaction models (e.g., sequence text distance) or no hierarchies which make them unable to design large systems (i.e., our systems require non-interacting sequences with >1200 base pairs). Even for small problems these solutions do not generate a sufficient set of sticky-ends. For example, the 96-arm motif structure is too large for these methods.

An alternative, but trivial, method is to randomly select sequences. Using a random sequence generator, thermodynamic analysis can be used to evaluate the design. The

computational effort is low in this case but there are obviously no guarantees on the optimality of the resulting design.

2.1.5.1 Thermodynamic Optimization Tool

To overcome the limitations of text distance and random sequence generation we have implemented a new optimization tool. The tool is a parallel implementation of an exhaustive thermodynamic search that can optimize a target design given a target topology and basic motif design against both the SEM and TLM estimators described in Section 2.1.3. The outcome is a set of arm sequences that can be used to generate a set of motifs that are optimized to reduce non-specific interactions during the assembly process. The algorithm evaluates each possible arm sequence against all other candidate sequences and motif sequences and maps their mutual interaction. Self-binding and region mismatching of up to 6 consecutive nucleotides are included in the evaluation.

To calculate the thermodynamic interaction of candidate strands (needed for both the TLM and SEM estimators) we used a modified nearest-neighbor algorithm based on the freely available MELTING4 tool [49]. MELTING4 calculates the melting temperature for any given pair of nucleic acid strands of the same length. The algorithm uses experimentally derived enthalpy and entropy values to estimate the interaction energy of each base-pair and accounts for the effects of neighboring bases and variable salt concentrations. The original code was modified to handle internal and terminal base pair mismatches [63, 73]. Terminal mismatches are treated by “padding” all evaluated sequences with a complementary 3-bp region. This better simulates the motif environment and ensures that the ends are complementary. The padding artificially increases the stability of a configuration (slightly) due to the additional matching base-pairs. This systematic bias means that the calculated values are more reliable as a relative measure of sequence melting temperature.

Given the vast sequence interaction space that must be covered, the execution time on a single processor can quickly become prohibitively large as the size of the target structure increases. To overcome this limitation the algorithm partitions the problem into sub-parts which are then executed in parallel on computing clusters and multi-processor machines. This greatly reduces the time needed to perform an optimization run and allows the application to target larger and more complex DNA nanostructures.

The following pseudo-code generates a TLM-optimized sticky-end solution arm set for the 20-arm or 96-arm systems:

```

1: FindDNASet(seq_length, set_size, fixed_seq)
2: {
3:   arms = generate_all_seq(seq_length);
4:   arms = remove_verboten(arms);
5:   seq_set = concat_set(arms, fixed_seq)
6:   results = cross_melt(seq_set);
7:   results = remove(results, fixed_seq);
8:   results = rank_seq(results);
9:   results = sort_by_TLM(results);
10:  top = head(results, set_size);
11:  return = top; }

```

The parameters are the target sticky-end length (5 for the cruciform motif), the target sequence set size (20 and 96 respectively) and the fixed sequence set which is pre-defined and held constant through the optimization process (the A and B cores, shells and arm stub strands).

The first step is to generate all possible sequences of the target sticky-end length. The size of this set is 4^n , where n is the target sticky-end length. In the next step, several “verboten” sequences are removed from the problem space [102]. Verboten sequences are known to have unfavorable properties for self-assembly (one example are guanine-only sequences which tend to distort the standard B-form double-helix).

The parallel cross-melt algorithm is executed on the resulting set of sequences (including fixed sequences). Each sticky-end sequence is evaluated against all other sequences in the set. When mismatches are included the evaluation of each sticky-end pair has a computational complexity of $O(n^2)$. The resulting overall complexity of cross-melt is $O(4^{2n}n^2 + 4^n km^2)$, where k is the length and m the width of the fixed sequence set. This assumes that fixed sequences have the

same length and calls to MELTING4 single sequence pair evaluation function have $O(1)$ complexity.

The cross-melting algorithm is embarrassingly parallel and we generate a workload unit for the analysis of each sticky-end against the other sequences in the set. Units are distributed to the cluster for simultaneous processing; the degree of parallelization is $O(4^n)$, proportional to the size of the sticky-end set.

The resulting aggregated interaction data is used to rank the strands based on their specificity (TLM). The top sequences represent the TLM-optimized solution set.

The algorithm presented implements a basic approach to sequence set optimization using thermodynamic analysis. Improvements can be made in functionality as well as efficiency. One example is the final sequence set selection (line 10), which does not account for the different context generated by the selection of a sub-set of the original sticky-end list. An optimal sub-set selection could enable further improved result metrics, especially for small target sets. Such optimal selection would be in NP and thus computationally expensive, but the problem is amenable to near-optimal greedy algorithms.

2.1.5.2 Alternative Designs

Single Core— The quality of the solution set will improve if the number of fixed motif strands is minimized. This is intuitive, given that each fixed strand adds additional constraints on the solution space. For our target system we apply this by using a single core on all motifs rather than the original dual core motifs (A-type and B-type). The tool can optimize for a single core (e.g., A-only or B-only) system by simply modifying the set of fixed sequences dedicated to the motifs (cores, shells, and arms).

Split Core— Our second approach to improve the design method makes use of the two motif types (A and B) in the context of hierarchical assembly. Both the 20-arm and 96-arm

systems are assembled in two separate hierarchical steps. In the first step single strands assemble into motifs. In the second step motifs are mixed and due to their sticky-ends they assemble into the target grid-like structure. Thus, the interaction between the sticky-ends and the fixed strands (cores/shells) is critical in the first level of the hierarchy, when motifs are annealed. In the second step (grid anneal) the motifs are assumed to be thermodynamically stable and the major factor becomes the motif sticky-end interactions.

We use this to generate an optimized set of sticky-ends for each motif type separately. This is equivalent to applying the Single Core method for both A and B motif types. The final set is obtained by combining the results of the two optimization runs with common sequences used only once. The A-type sticky-ends will have sub-optimal interaction with the B core/shells (and vice versa), but the hierarchical assembly process guarantees that they are only simultaneously in assembly solution in the second step.

Since the sticky-ends must be unique across the whole system, the effectiveness of this approach depends on the TLM estimates of the resulting solution sets for the A and B motifs. However, the sequences for the A and B core and shell strands were originally designed to be as different as possible in order to minimize their mutual interaction (i.e., large TLM for each motif type). We expect that this will also translate into significantly different solution sets for each core.

The pseudo-code for the Split A/B design is the following:

```

SplitDesign(set_size)
{
  setA = FindDNASet(5,set_size,A_CoreShells);
  setB = FindDNASet(5,set_size,B_CoreShells);
  setA = sort_by_TLM(setA);
  setB = sort_by_TLM(setB);
  for (i=0;i<(set_size/2);i++) {
    seq = head(setA,1);
    ret_setA = concat_set (ret_setA,seq);
    setA = remove(setA, seq);
    setB = remove(setB, seq);
    seq = head(setB,1);
    ret_setB = concat_set (ret_setB,seq);
    setA = remove(setA, seq);
    setB = remove(setB, seq);
  }
  return = concat_set(ret_setA, ret_setB); }

```

The solution sets for each core are separately computed and the final set is assembled from the top sequences of the two sets.

Passive Core— The third method uses hierarchical assembly to significantly reduce the fixed sequence set. Instead of a single assembly step in which nine single strands (one core, four shells and four arms with sticky ends) hybridize to form the cruciform motif we design a two step process to form the same structure.

In the first step the core and the four shell strands hybridize to form an arm-less motif. At this point we permanently bind the hybridized core-shell areas of this structure using a crosslinking agent such as psoralen [36]. In the second step the arms are added to the intermediate motif to form the target cruciform motif. Since the core-shell portions are permanently bound together, these sequence areas become passive elements in the second hybridization step.

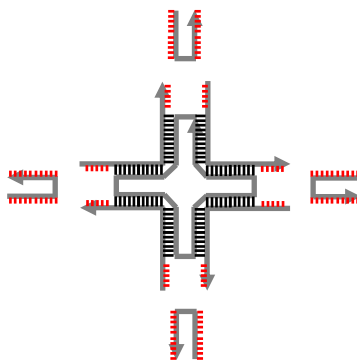


Figure 2-5: The arm-less motif has a passivated core-shell region (interior) and four active shell regions (distal) that can bind the arms.

The reduced active areas in the second step result in a significantly smaller fixed sequence set. We optimize the target arm sticky-end set in the second step and the reduced fixed sequence set imposes fewer constraints on the thermodynamic optimization process and facilitates improved results compared to the one-step assembly.

SEM Optimization— The above methods were presented in the context of obtaining TLM-optimal sequence sets for low assembly error rates. However, improved structural stability (SEM) could also be an important design goal. For example, the self-assembled system might need to be stable in certain temperature ranges in order to interface with other systems. Our design tool can optionally trade TLM-optimality for SEM-optimality. This trade-off is controlled with an SEM factor (SF) that expands the candidate set (proportionally) of TLM ranked sequences for subsequent ranking by their SEM estimates. The pseudo-code below illustrates this process:

```
FindDNASet(seq_length, set_size, fixed_seq,
  sem_factor)
{
  ... (lines 3 to 11 from the original FindDNASet)
  ex_set_size = set_size * (1 + sem_factor);
  top = head (results, ex_set_size);
  top = sort_by_SEM(top);
  final = head (top, set_size);
  return = final;
}
```

2.1.6 Analytic Evaluation

We evaluate the results of each presented method (AB, A-only, B-only, Split A/B and Passive Core) in terms of specificity and stability (TLM and SEM estimates) as applied to a small 20-arm system and a structurally similar but larger 96-arm system (as described earlier). The results are compared with the expected values for a random sequence design as well as the original 20-arm set from [105] which was generated with the widely used text-distance tool SEQUIN [77]. Table 2-1 shows the results in terms of SEM, average non-specific T_m (NST_m) and TLM for each method.

20-Arm	SEM	NST _m	TLM
AB Core	7.12	-6.87	9.81
AB Core Original*	11.77	4.83	4.24
AB Random	10.04	4.01	3.32
A-Only	7.66	-6.44	9.82
B-Only	9.75	-4.68	10.00
B-Only SF=4	14.08	-0.08	9.65
AB Split	9.75	-4.74	9.99
AB Passive	9.92	-4.28	9.93
A-Only Passive	10.67	-3.90	10.05
B-Only Passive	10.68	-3.87	10.06
B-Only Pass SF=4	15.51	1.78	9.60
AB Split Passive	10.83	-3.95	10.15
AB Split Pass SF=7	15.67	1.97	9.60
96-Arm			
AB Core	6.66	-6.65	9.25
AB Random	10.04	4.01	3.32
A-Only	7.80	-5.83	9.44
B-Only	8.17	-5.68	9.52
AB Split	8.28	-5.54	9.57
AB Passive	8.05	-5.64	9.52
A-Only Passive	8.23	-5.62	9.58
B-Only Passive	8.74	-5.13	9.61
AB Split Passive	8.63	-5.34	9.67
AB Split Pass SF=.7	11.88	-2.04	9.43

Table 2-1: 20-Arm and 96-Arm results. *No 96-arm original exists.

To evaluate the upper bounds for the SEM and TLM of each method we remove all fixed sequences (cores/shells) and evaluate the best possible sets for each metric. This simulates a theoretical system in which the core and shells do not interact with the sticky-ends. To obtain the highest SEM design we use a large SF factor. The results are shown in Table 2-2.

20-Arm	SEM	NST _m	TLM
No Core – rank by TLM	11.93	-3.29	10.47
No Core – rank by SEM	18.94	6.95	7.22
96-Arm			
No Core – rank by TLM	8.96	-5.16	9.77
No Core – rank by SEM	15.90	3.39	8.05

Table 2-2: Upper bounds on TLM and SEM with 5-nt sticky-ends

The random sequence method results show a high SEM, which translates into good expected stability for the target assembly. However the overall specificity (TLM) is very low, suggesting that the system is likely to form defective structures when self-assembling.

The SEQUIN-generated 20-arm original design shows a slight increase in both TLM and SEM when compared to random. However, the TLM is still low and this shows that using simple text-distance metrics and heuristics for optimizing sequence sets can lead to uncertain results if low error rates are desired.

The AB Core set generated with our tool shows a significant improvement in specificity. The target structure is thus much more likely to form correctly when using this method. The stability estimate is lower than the original design which means that the system will disintegrate at slightly lower temperatures. However, the SEM factor (SF) can be used to trade specificity for stability and can be used to balance the design.

A-Only, B-Only and SplitA/B show further improvement for both SEM and TLM metrics. Combining both SplitA/B and Passive Core methods yields the highest TLM metric, close to the theoretical upper bound for the 20-Arm and 96-Arm systems.

Figure 2-6 shows scatter plots of four sequence sets for the 20-arm system. The diagonal represents the line of zero specificity (TLM=0) where specific T_m equals non-specific T_m . The distance to this line from any given point (sequence) is the TLM. The AB Core sequences are

clustered in a series of points situated at roughly similar TLMs. The random and original designs do not show this pattern and include sequences that are situated on the diagonal itself: these sequences are just as likely to base-pair with the core/shells as they are with their complements! These strands are likely to have a particularly disruptive effect on structure formation in their sets and there is some evidence that this is the case [59].

Compared to the AB Core the higher-performing AB Split Passive method creates a cluster that is further away from diagonal and has a higher specific T_m average. This corresponds to an increase in both TLM and SEM.

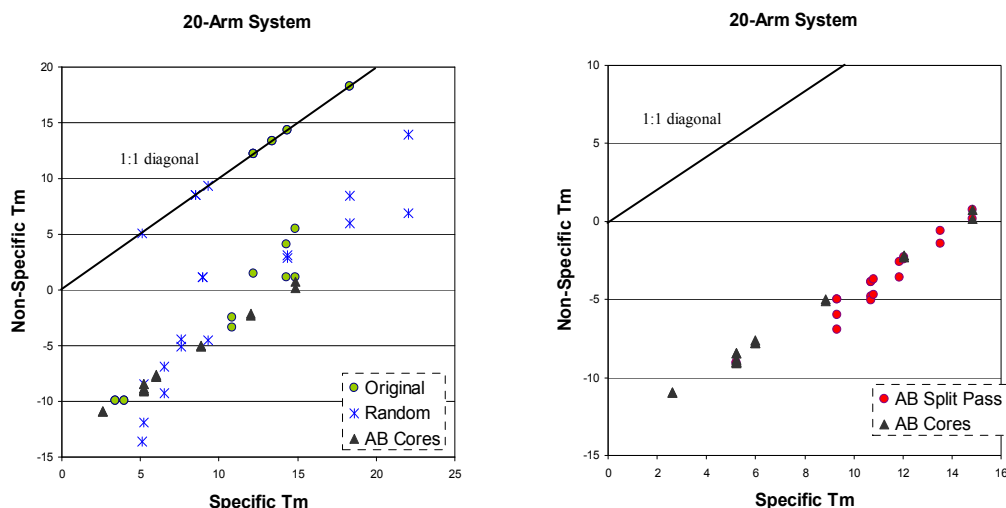


Figure 2-6: AB Core, AB Split Passive, random and original 20-arm sets

Figure 2-7 shows that when the number of fixed sequences (cores/shells active areas) decreases (B-only Passive vs. B-only vs. AB Cores) the average specificity of the system increases. The specificity of each arm is defined as the minimum of its TLM and the TLM of its complement. (In all 5-nt arm systems there are 600 candidate sequences because 524 of the total possible 1024 sequences are verboten and removed.) This result verifies the intuition that fixed sequences in the motifs restrict the number of high quality (i.e., high specificity) arm sequences.

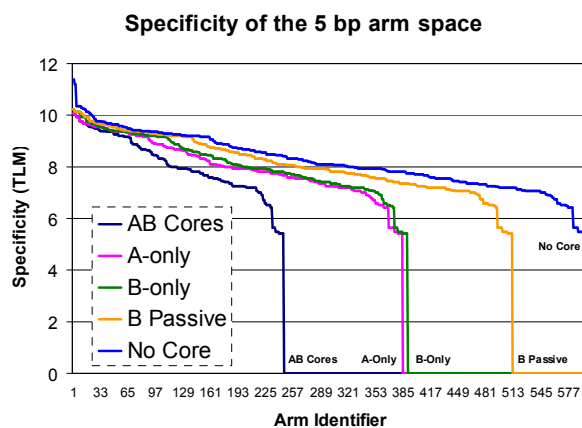


Figure 2-7: Specificity in arm space with different fixed seq. sets

Figure 2-7 also shows the systematic bias induced by the thermodynamic optimization tool due to sequence padding. There is an offset of ~ 5.4 for non-zero TLM values for all the designs due to the always-complementary 3-bp pads used by our tool.

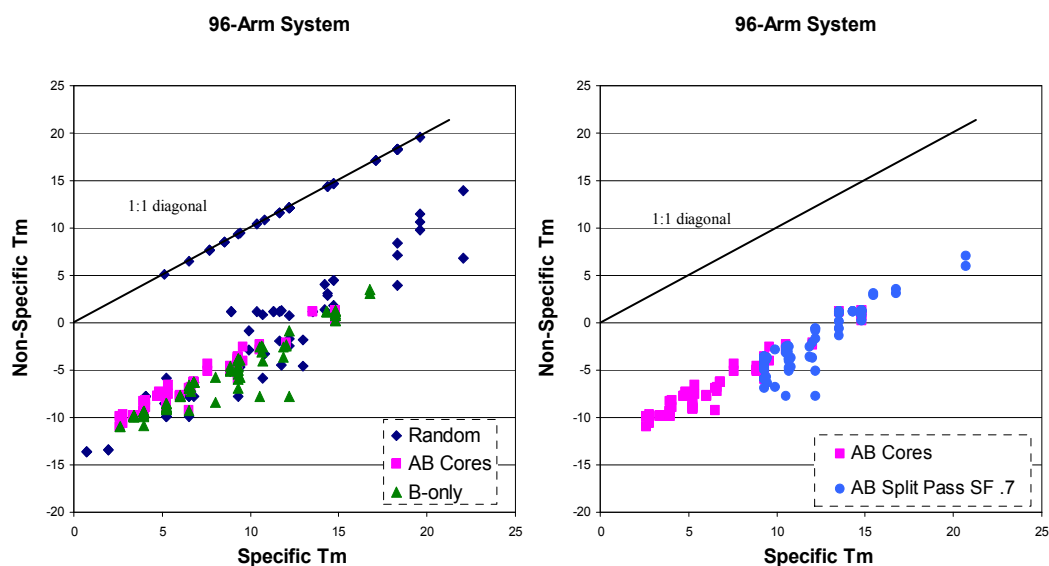


Figure 2-8: a) B-only, AB Cores and Random for 96-arm sets b) AB Cores and AB Split Passive SF 0.7

The results of B-only, AB Cores and random methods for the 96-arm design are presented in Figure 2-8a. Random has many arms that strongly interact with the core/shells

(mapped on the diagonal). B-only shows the same clustering as AB Cores, but it is on average slightly farther away from the diagonal (higher specificity). Figure 2-8b contrasts the AB Core with the superior AB Split Passive. The latter shows improved distance to diagonal and at the same time significantly higher specific T_m (SEM) due to the applied $SF=0.7$.

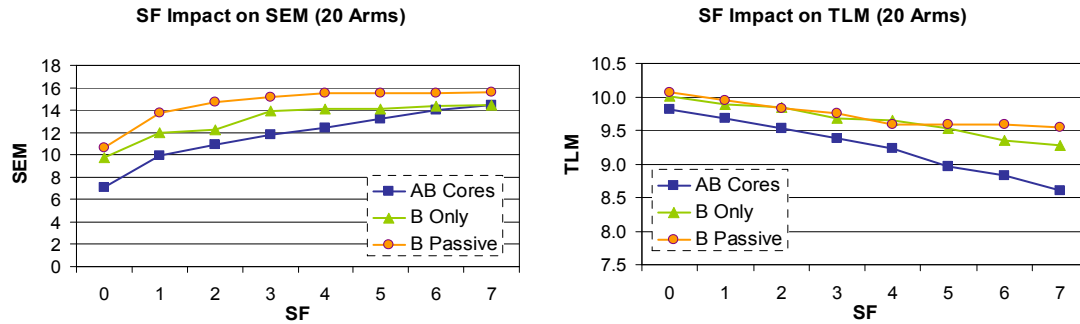


Figure 2-9: Trade-off: specificity can be traded for stability

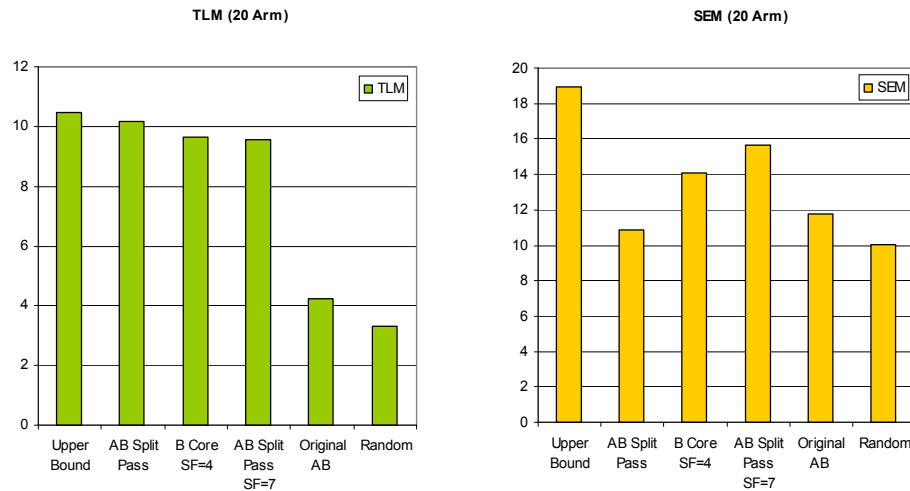


Figure 2-10: 20-arm designs balanced for TLM and SEM metrics

The Split AB Passive Core design is the best performer for TLM-optimized designs, outperforming all other methods. The scatter-plot is similar to the B-only set in fig. 8 and we omit it for brevity. Figure 2-9 shows how the SF factor can be used to increase the SEM of a design at the expense of a slightly lower TLM. In Figure 2-10 two such balanced designs, one based on the

B-only method and one on Split AB Passive are contrasted with the text-based design of the original AB and with the random method, as well as the unbalanced, TLM-oriented AB Split Passive. The theoretical maximum SEM and TLM for 5-nt sticky-end designs are included for comparison. Table 2-3 lists our best *AB-Cores* arm sequences.

Arm	Comp.	Arm	Comp.	Arm	Comp.
CGTGC	GCACG	CCTCG	CGAGG	TATGT	ACATA
CAAGC	GCTTG	ACGAC	GTCGT	TGTAT	ATACA
ACGTC	GACGT	CAGAC	GTCTG	TTAGA	TCTAA
ACAGC	GCTGT	ACTGC	GCAGT	TTACT	AGTAA
TGCAG	CTGCA	TGCTG	CAGCA	TAAGA	TCTTA
CTGTG	CACAG	TGCAC	GTGCA	AATAG	CTATT
AGCTC	GAGCT	AGAGC	GCTCT	AATTC	GAATT
CATGG	CCATG	CTTGG	CCAAG	ATACT	AGTAT
CAATC	GATTG	CATTC	GAATG	TAACT	AGTTA
AATGC	GCATT	ATTGC	GCAAT	TTAGT	ACTAA
AACGT	ACGTT	CTAAC	GTTAG	TACTT	AAGTA
CTTAC	GTAAG	TTACG	CGTAA	TAAGT	ACTTA
TAACG	CGTTA	CATTG	CAATG	TAGAT	ATCTA
ATGAC	GTCAT	ATGCT	AGCAT	TAGAC	GTCTA
TCATG	CATGA	TTGCT	AGCAA	TTCAT	ATGAA
TTGAG	CTCAA	AAGCT	AGCTT	ATTCT	AGAAT
TGCTT	AAGCA	ACTGT	ACAGT	TCAAT	ATTGA
TCACA	TGTGA	AGTAC	GTA CT	TTAAC	GT TAA
TACGT	ACGTA	TGTAG	CTACA	AATCT	AGATT
TACTG	CAGTA	AAGTG	CACTT	TGATT	AATCA
TCAAC	GTTGA	TCTGA	TCAGA	TCATT	AATGA
TCTAG	CTAGA	TAGCT	AGCTA	TATGA	TCATA
AATGT	ACATT	ATGTT	AACAT	TTAAG	CTTAA
ATTGT	ACAAT	TTCAA	TTGAA	TTACA	TGTAA
GTTAT	ATAAC	AATAC	GTATT	TTGTA	TACAA
TAATG	CATTA	CAATA	TATTG	TTGAT	ATCAA
TTATG	CATAA	AATTG	CAATT		

Table 2-3: The best 160x5-nt arm sequences (and complements) found by our AB-Core method. These arm sticky-ends are compatible with our tile motif and system described partly in [59].

2.1.7 Experimental Evaluation

Figure 2-11 shows AFM images of assembled 4x4 grids that use the optimized *AB-Cores* arm sequence set from Table 2-3.

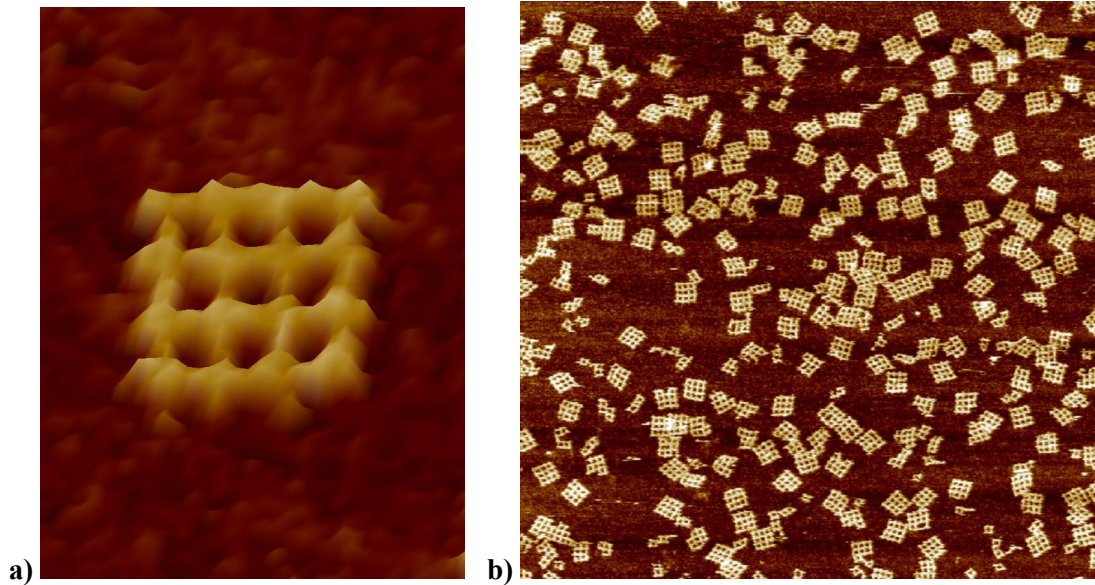


Figure 2-11: AFM image of a) single DNA grid and b) typical deposition of multiple grids on 2x2 μ m micron area. Each grid cavity is \sim 20nm wide.

We observe a large number of correct, fully formed DNA grids that are bound to the atomically flat mica plane. The high apparent yield of this method compared with alternative techniques[59] is an experimental validation that optimizing SEM and TLM sequence metrics and motif hierarchies can have a dramatic impact on the results of the DNA self-assembly process. The complete experimental procedures are detailed in section 2.2.5.

2.1.8 Summary

DNA's precise binding rules at small scale (a few nm) make it a potential candidate for the fabrication of circuit substrates for future nanoscale computing systems. In this section we presented a thermodynamics-based computer aided technique for DNA nanostructure design.

Compared to existing text-based tools, our approach enables the creation of structures of previously unattainable size and produces superior designs for small structures. Furthermore, we experimentally validated this technique through the massively parallel assembly ($>10^{12}$ units/cm³) of 60nm x 60nm DNA grids with 20nm pitch.

In the next section we evaluate options for cost-effective further scaling of the structure size and we experimentally demonstrate the ability of DNA grids to provide a substrate for circuit-type molecular patterns.

2.2 Scalable, Low-cost, Hierarchical Assembly of Programmable DNA Nanostructures

Recent advances in the synthesis of structurally rigid molecular complexes from DNA [33, 52, 76, 78-80] have produced many examples of periodic planar DNA lattice [39, 48, 52, 67, 105, 111]. Aperiodic lattices, where each individual tile is chemically uniquely addressable, are significantly more useful for circuit substrates because they can support arbitrary circuit topologies. However, methods that form aperiodic 2D structures like the 60nm x 60nm DNA grid detailed in Section 2.1 require the number of unique DNA sequences (and therefore cost) to scale with the area of the structure or the development of algorithmic self-assembly [7, 102]. To overcome such limitations we demonstrate a low-cost hierarchical method to fabricate large molecular weight, aperiodic structures by DNA self-assembly.

We build on our prior work with aperiodic DNA self-assembled nanostructures to create a set of four uniquely-edged 4x4 grid structures (see Figure 2-12). Each motif is assembled from five common and four unique oligonucleotides. The unique sequences are selected from the TLM-optimized *AB-Cores* set generated by our thermodynamic analysis software. The cost of our technique scales with the number of unique oligos in the final nanostructure (e.g., 69 oligos in this case). The origami method [71, 72] which generates programmable DNA structures by

folding a single, long DNA strand, suffers from this scaling law as well but in principle could use the methods outlined here to reduce the cost of larger multi-shape structures. Our methods go beyond the origami work to organize programmable structures from multiple long-strand motifs and can be applied to the dense plasmid-based motifs described in [72].

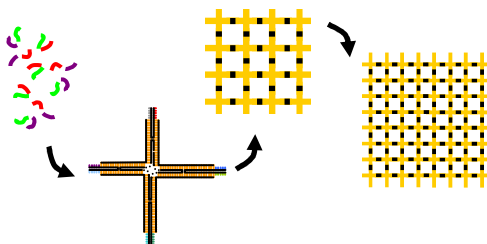


Figure 2-12. The hierarchical approach to build motifs from individual strands and then into 4x4 or 8x8 grids.

Regardless of the method employed to assemble the basic motif we must bypass the requirement of a unique set of sticky-ends required to assemble a structure unambiguously and reuse strands to decouple the cost of a structure from the linear dependence on its area. Thus, such a method is scalable in terms of the size of the nanostructure that can be fabricated from a finite DNA sequence space. In the limit, a single oligonucleotide sequence might be used to form large supramolecular structures [51]. However, to retain maximal programmability we use multi-strand designs with a variable degree of re-use. Strand reuse is exploited to some extent in both methods [59, 71, 72] but has not previously been demonstrated as a viable alternative for assembling large aperiodic structures.

We have explored two methods to achieve scalable DNA self-assembly, one that uses generic linkers and one that uses fully specific linkers to bind motifs. Each method builds larger structures from smaller motifs in a hierarchical manner. Figure 2-12 illustrates the hierarchical approach we have investigated.

2.2.1 Generic linkers

A series of “generic” sticky-ends along the periphery of a DNA grid aid in binding a grid to an adjacent grid. The generic linkers¹ are designed to bind with only one helix (typical arms have two helices) to introduce a relatively unstable interaction. This is to prevent the generic linkers from dominating the specific interactions we will introduce later to programmably organize two distinct grids. The generic linkers are replicated along the grid-edge to liberate the few otherwise specific sequences and thereby enable stable binding between two grids. It is then possible to apply an incremental graph-coloring method, with a constant number of specific binding sites, to sequentially add motifs to the growing structure [21].

The specific binding of the two distinct grids is achieved by using non-generic sticky-ends at selective locations, in this example at the lower right and upper right corners of the two 4x4 grids, respectively (this will become the middle-right edge in the 32-motif structure). Figure 2-13 shows the relationship between generic and specific arms. The gap along the edge between the two 4x4 grids is introduced to disambiguate the identity of each grid in the assembly.

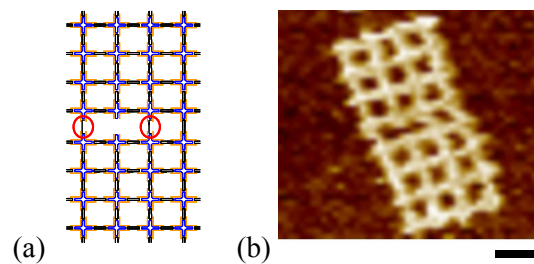


Figure 2-13. (a) Schematic and (b) AFM image of a two-grid (4x8) assembly. Only one linkage at the interface between the two distinct 4x4 grids is specific (right-most) and the remaining two are generic (circled). Scale bar is 40 nm

¹ The left linker in Figure 2-13 is 5'-TAGATGATAGAGTGGTACATCT-3' and the right is 5'-ATCTAACGGATGAGTAGTGGGCTCAGTCGGAT-3'

This demonstrates that multiple weak interactions between oligos along the edge of a grid (generic linkers) can be controlled (or dominated) by a single strong specific interaction. Moreover, this is evidence that the free energies among distal nucleotide interactions constructively add between bound motifs. We infer that the gap introduced for identification purposes may disrupt cumulative non-specific binding induced by the generic oligos. Further, the stability (at room temperature) of such assemblies is compromised because of the weakness of the generic linkages and gap. This may contribute to a reduced apparent yield of the 32-motif structure. However, this demonstration illustrates that the use of generic linkers along the edge of a DNA nanostructure can be dominated by a single specific interaction and enables the development of scalable sequential assembly methods.

2.2.2 Fully specific linkers

Our second method uses fully specific sticky-ends along the periphery of each sub-grid. The re-use of sticky-end sequences from within each grid reduces the number of unique oligos required to assemble larger arrays. This does not induce ambiguous assembly because the sticky-ends are re-used after the constituent pieces of the grids have already formed. For example, we can re-use sticky-ends from the four tetramers in each grid after the grid has assembled. We conclude that this is only possible because strand exchange between the re-used sticky-ends and the intra-grid sticky-ends does not occur.

We have tested the sticky-end re-use by assembling a 2x2 array of grids. Figure 2-14 illustrates a typical AFM scan of the assembled 64-motif product on cleaved mica. The molecular weight of these structures is 8,960 kD and therefore one of the largest synthetic and nanostructures ever synthesized.

The use of AFM to determine the “yield” of assembly is not an accurate method since the mica surface used as a substrate (with the imaging buffer) will preferentially bind large, flat,

charged DNA structures. Further, the simple motifs used here, unlike those in [72], are not easily imaged alone by AFM but must be assembled into larger structures to be reliably observed.

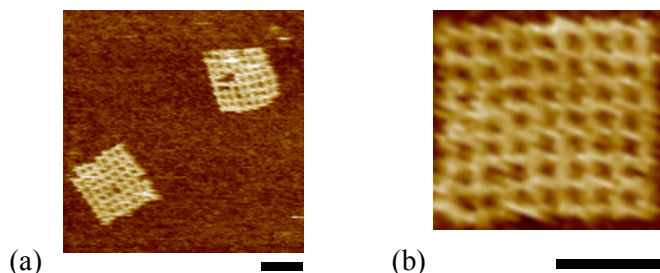


Figure 2-14. (a) An AFM scan of the 2x2 array of grids. (b) the assembled array demonstrates stability even under repeated AFM scans. Scale bars are 100 nm.

Thus, to determine the relative merit of our technique we must evaluate the defect rate of assembled structures since the “raw” motif yield is unknown. Figure 2-15 and Figure 2-16 are histograms of the AFM-observed, surface-bound assembly products. Structures were classified as either *identifiable* (i.e., as a 64-motif grid) or *un-identifiable* (i.e., fragments).

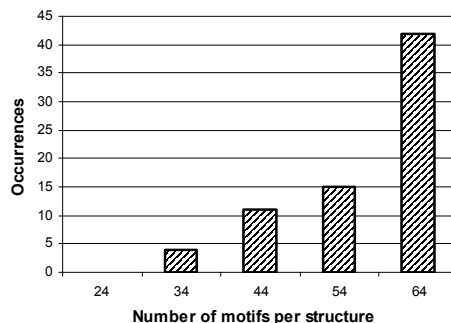


Figure 2-15. Histogram of identifiable structures as observed by AFM (N=73).

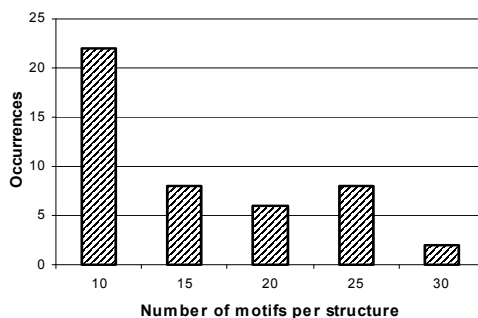


Figure 2-16. Histogram of un-identifiable structures as observed by AFM (N=43).

The binning used in Figure 2-15 and Figure 2-16 is 10- and 5-motifs wide, respectively. For example, incomplete structures with 55 motifs will be binned with fully intact structures with 64 motifs in Figure 2-15. Structures were disregarded if any of the following was observed: (i) clipping by the scan window, (ii) piling into agglomerations, or (iii) manipulation away from the surface during a line scan.

The presence of non-ideal, defective structures is not surprising. We note that the availability of purification methods is a key advantage of DNA self-assembly in the face of defects. The use of solid-support or affinity binding purification may be able to remove defective structures. The *yield-scalability* of our technique will depend on the efficiency with which defective material can be removed. However, the *size-scalability* of our technique depends only on sequence and motif re-use. Recent work in error-resilient nanostructure design may be applicable within this framework [9, 66, 84, 103].

2.2.3 Polymer-mediated connectivity

The use of linkers and hierarchies presents a scalable method to fabricate large DNA structures. An extension of this method is the use of linker motifs that form periodic polymers to bridge grid motifs. The advantage of using polymers is that of potentially increased connectivity between grid nodes. When structures are deposited on a 2D surface the polymer bridges can overlap and connect multiple motifs. Recent nanoscale computing architectures [61],[62] can exploit such random networks to configure systems capable of general computation.

As a proof of concept we use the DNA nanotrack [105] design to connect two 4x4 grids with a 2-tile wide polymer. The track is composed of 4 individual tile motifs that form a repeating pattern. Figure 2-17a shows an AFM scan of an assembled structure, where two 4x4 grids are connected by the 4-tile long track. Because of the repeating, polymer structure the length of the track can vary.

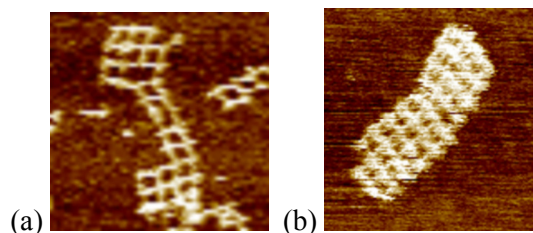


Figure 2-17. AFM image of a) two 4x4 grids connected by a 2-wide polymer track and b) 4-wide polymer track. . Each cavity in (a) and (b) is ~20nm wide.

The number of AFM-observable fully connected structures we observed in large area scans is relatively low. A possible explanation is that such particular constructs are likely to aggregate in solution and thereby become less likely to be visible on surface deposition-based AFM scans. One way to potentially prevent this aggregation would be to start polymer growth only after the grids are deposited on the surface.

Figure 2-17b shows an assembled 4-wide polymer track. Such wider bridging tracks could enable multiple connecting wires and thus provide higher bandwidth between the self-assembled circuit nodes.

2.2.4 Chemically programmable structures

Since each motif is assembled from five common and four unique oligonucleotides in an individual vessel, each grid can be independently modified and can create arbitrary patterns of target molecules as shown in Figure 2-18. To demonstrate programmability the grids are selectively functionalized with streptavidin (SA) by using a biotin-functionalized core-oligo during the annealing of the component motifs and introducing free SA afterwards (SA binds with strong affinity to the small biotin molecule). We use SA because its ~5nm diameter makes each bound molecule easy to distinguish in height-based AFM images.

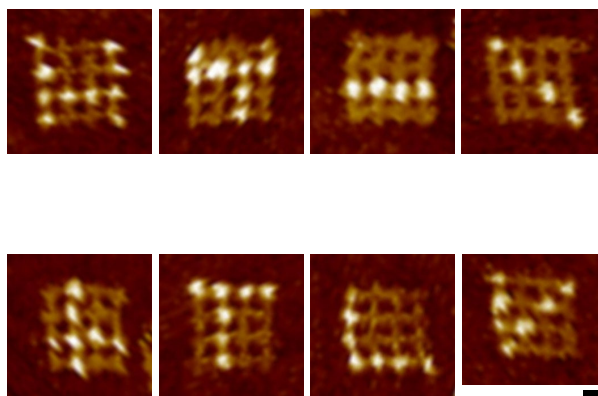


Figure 2-18. AFM images of streptavidin patterned 4x4 DNA grids. Scale bar is 20 nm.

The functionalization points can be placed at various locations on the cruciform tile structure. Figure 2-19 shows two grids programmed with an “N” pattern. In Figure 2-19a we place the binding point at the center of each functionalized tile. In Figure 2-19b we place the binding points off-center on the left side tiles and centered on right side tiles. The different relative positioning of bound SA is apparent. This flexibility in programming the pitch and relative positioning of bound molecules opens the possibility of assembling and interconnecting active molecular computational elements like carbon nanotubes [5, 13], silicon nanowires[43], nanowire transistors[83] and photonic circuit devices (Chapter 3).

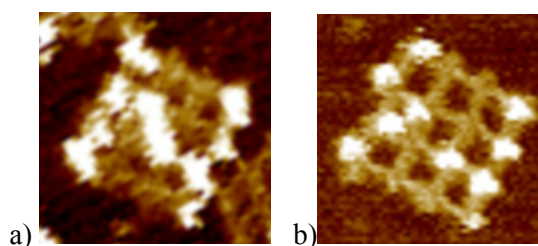


Figure 2-19. AFM scans of 4x4 DNA grids with bound streptavidin. In (a) we use active binding points that are tile-centered. In (b) we use off-center binding points on the left side of the grid and centered points on the right side.

The rate of success in binding the target SA molecules to the functionalized access points is dependent on the concentration of SA added. The patterns shown in Figure 2-18 and Figure 2-19 are assembled with a small excess of 20% SA. Figure 2-20 shows 4x4 grids with a line target pattern in the presence of 20% SA excess (a) and 900% SA excess (b).

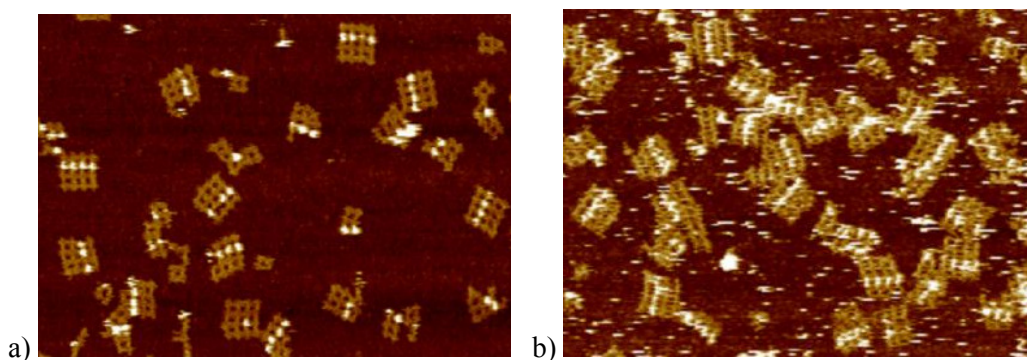


Figure 2-20. AFM images of SA line patterns on 4x4 DNA grid using a) an excess of 20% of SA and b) an excess of 900% of SA

The higher concentration of protein increases the probability of binding SA on all active biotin sites. However, as we can see in Figure 2-20 a large excess of SA is not a requirement when functionalized grid sites are easily accessible for binding, as they appear to be for the linear pattern. Since biotin binds very strongly to SA (the dissociation constant is 10^{-15}M) the binding event is practically irreversible in the given experimental conditions.

2.2.5 Experimental Procedures

The simple DNA motifs we use have nine ssDNA sequences: one core (150-nt), four shells (~40-nt), and four arms (~35-nt). The core and shell sequences were generated with the program SEQUIN [77]. The sticky-end sequences that coordinate the binding of motifs into larger assemblies were generated using our DNA design automation software (Section 2.1.5) to minimize the chance of undesired hybridization. Synthetic oligonucleotides were purchased from

Integrated DNA Technologies (Coralville, IA) and purified by polyacrylamide gel electrophoresis.

The motifs were formed by mixing a stoichiometric quantity of each strand in buffer, 1xTAE/Mg²⁺ (Tris acetate, 40 mM, pH 8.0), (EDTA, 2 mM), and (Magnesium acetate, 12.5 mM). The final motif concentration was 1 μM. The equimolar strand mixture was annealed by heating to 95°C, slowly cooling to 4°C over 24h and then incubating at 4°C for 12h.

The 4x4, 16-motif grid was formed by mixing a stoichiometric quantity of each motif and annealing at a constant 23°C for 4h. The sample was then incubated at 4°C for 12h. The same annealing procedure was used to create the 64-motif 2x2 array by mixing equimolar quantities of the four constituent 16-motif 4x4 grids.

The polymer-linked structures were formed by adding the first 4x4 grid with the 4 polymer tiles, annealing for 30min at 23°C, then adding the second 4x4 grid and annealing for 20min at 23°C and then 12h at 4°C.

Biotinylated core strands and streptavidin (SA; Invitrogen) interaction were used to demonstrate full addressability. SA was added to the aqueous solution of the assembled DNA nanostructures. The mix was incubated for 1 h at 27°C and then 12h at 4°C. The concentration of SA:Core ratio was 1.2:1 (20% excess SA).

AFM was performed under 1xTAE/Mg²⁺ buffer in tapping mode. Each sample to be imaged was deposited (3 μL) onto freshly cleaved mica and left for 2 min, then 25 μL of 1x TAE/Mg²⁺ buffer was added to the mica and another 25 μL was placed on the AFM tip. AFM images were obtained on a Digital Instruments Nanoscope IIIa instrument with a multimode fluid-cell head with NP-S oxide-sharpened silicon nitride tips (Veeco). Tips were plasma cleaned and coated (to reduce protein deposition) with PEG by immersion in a 1mg/mL PEG solution followed by gentle drying with compressed carbon dioxide.

2.3 Conclusion

Our work in designing DNA nano-structures is motivated by their potential to provide an excellent engineering scaffold for the assembly of molecular scale circuits and sensors. This application requires an assembly method that is low cost, can scale to large-size designs and provides full chemical addressability in the resulting structures.

The method we presented in this chapter is a low cost synthetic mechanism because of motif and strand re-use but can also leverage complex motifs assembled by other means, such as with the DNA origami method. Our method uses thermodynamic analysis and design automation techniques to select optimized DNA sequences and can achieve the fabrication of larger programmable structures than have been previously demonstrated by tile- or motif-based methods.

We experimentally demonstrated this method by assembling a 140nm x 140nm DNA grid using strand re-use to decouple the cost of the structure from its area. This approach is applicable to larger structures and is limited by the ability of such structures to diffuse through solution and assemble with the same degree of selectivity as demonstrated by smaller structures. Thus, the yield of such assemblies will challenge the synthesis of larger structures and demand refinement in the process. The diminishing apparent yield of the method is fundamental to all self-assembly methods that organize molecular scale components from motifs and may require purification methods to achieve larger structures. Clearly, there is some size scale at which non-specific interactions begin to dominate the process but promising results in periodic DNA crystal formation suggest that this scale is near-macroscopic [39].

The DNA grid design supports scaffolding of nanoscale components through complete chemical addressability. We experimentally demonstrated this full substrate programmability of DNA grids by assembling arbitrary circuit-type patterns of small molecules (proteins).

In the next chapter we build on the substrate features of DNA structures and propose a new type of molecular circuit devices that enable a complete integrated technology for computing and sensing.

3 Nanoscale Optical Circuits using RET Logic

To date there is no clear winner in the field of nanotechnology for computing. CMOS continues its relentless march toward smaller feature sizes, but the cost of fabrication facilities increases with each new technology generation. Carbon nanotube and ring-gated nanorod FETs are hopeful candidates, but obtaining control over the precise device length and precise placement for arbitrary patterns remain open challenges. Researchers have demonstrated molecular constructs capable of implementing basic Boolean logic gates[6, 18, 31, 91] and a variety of logic functions[8, 54, 55] in a range of chemical environments, including on cellular biological substrates[70, 75, 101]. However, scaling these devices to larger systems is a challenge because they often use chemical inputs and outputs and have multiple representations for binary signals. Optical switches[11, 34, 41], logic elements [4, 68] and waveguides [40, 58] are promising candidates in this context, but inter-connectivity of individual devices remains a challenge [18].

This chapter proposes a new nanoscale technology for computing based on single-molecule optical devices—called chromophores. In isolation, a given chromophore absorbs photons of a specific wavelength and emits photons at a different, lower energy, wavelength. However, when appropriate chromophores are placed a few nanometers apart the energy of an absorbed photon can be transferred to a neighboring chromophore through a process called Resonance Energy Transfer (RET). This process provides the theoretical foundation for the creation of pass gates (both inverting and non-inverting) using four chromophores per gate. These gates form a complete Boolean logic set, which we call RET-logic.

A key requirement for RET-logic is to place unique chromophores within a few nanometers of each other. We use DNA-based self-assembly as the fabrication method to place chromophores within specified distances. The specific DNA nanostructures we are fabricating in our lab are grids where we can place two pass gates and one wire crossover per grid vertex. The

design and assembly of the DNA grids is described in detail in Chapter 2. The grids can be hierarchically assembled to create large arrays of pass gates—the nanoscale equivalent to a sea-of-gates.

DNA-based self-assembly of chromophores provides a scalable, cost-effective technique for molecular-scale computing. However, the overall system must meet certain requirements to provide the appropriate abstractions for computing. The requirements include, but are not limited to: 1) gates: nonlinear modulation of signals, 2) wires: linear signals, 3) insulators, 4) signal restoration: energy supply, 5) circuits with feedback, and 6) input/output.

In this chapter we show how RET-logic on DNA grids can be used to meet the above requirements for a complete technology. Using this technology we design and layout several circuit elements (e.g., multiplexor, decoder) and memory. These circuit elements can be used to design simple computational nodes targeted for specific application domains. The small size of individual nodes could enable bio-compatible computing where an individual node could be used to sense various activities (e.g., presence of certain proteins) within, or in samples taken from, a living organism.

From first principles we construct analytic models for circuit performance and power consumption. These models show that RET-logic can provide switching times on the order of nanoseconds while consuming only nanowatts per gate. In our sea-of-gates node, assuming 100% of gates are consuming power this bounds the power/energy at microwatts per node.

The primary contributions of this work are:

- We propose a novel nanoscale optical device based on Resonance Energy Transfer.
- We show a path to a complete integrated technology.
- We present designs for several important circuit elements and memory using the new technology.

- We construct analytic models from first principles for device performance and power consumption.
- We provide laboratory experimental results demonstrating initial steps toward a prototype system.

The remainder of this chapter is organized as follows. We begin by describing Resonance Energy Transfer (RET), the theoretical basis for our active devices, in Section 3.1. We present an integrated RET technology in Section 3.2. We analyze power and performance in Section 3.3. Section 3.4 discusses potential application domains for our RET logic. Our initial steps toward a prototype are described in Section 3.5 and we conclude in Section 3.7.

3.1 Resonance Energy Transfer Logic

The molecularly-precise fabrication enabled by DNA self-assembly can place and interconnect a limited number of components. At this scale, atoms and molecules must be counted as distinct components and thus the fabrication of “bulk” electronic materials (i.e., >1000 atoms) is more challenging than the fabrication of single molecule assemblies. For this reason, we are developing logic devices built from precisely placed collections of chromophores. The logic device we introduce in this section is built on principles from quantum mechanics and photochemistry but is used here like a *classical* computational element. A useful analogy for our device is electronic current-mode logic where the current (high or low) through a circuit branch represents a Boolean value (1 or 0). However, the physical properties of the molecules in our device exhibit fundamentally different power dissipation and switching rates of the logic blocks with respect to current-mode logic.

This section describes an approach for creating a complete logic technology using chromophores. We begin with background on resonance energy transfer, the theoretical basis for our technology. We conclude this section with a description of our proposed primitive circuit

elements (wires and gates). The following section analyzes and describes a complete integrated RET technology for logic circuits and memory.

3.1.1 Resonance Energy Transfer

Resonance energy transfer (RET) is the underlying mechanism that couples energy from a source (donor) chromophore to its destination (acceptor) chromophore. The transfer resembles the current rectification of a PN diode since the excited-state energy of the donor transfers to the acceptor but not vice versa.

The transition energy diagram for this process is shown in Figure 3-1. The donor (D) is first excited by the absorption of a photon with energy $h\nu_1$ denoted by D^* . The excited-state donor energy, also called an *exciton*, is transferred to the acceptor (A), which becomes excited (A^*) through RET and, by spontaneous decay of the excited-state A^* to A , emits a photon with lower energy $h\nu_2$. The latency of this process was first derived by Förster based on classical charge dipole-dipole coupling and quantum mechanics and is in the 10^{-11} to 10^{-9} sec time scale [93]. Absorbed energy (1) excites the donor from its ground state D_0 to D^* and can decay radiatively (2) or non-radiatively (2a) to produce a photon (2b) by fluorescence RET. The energy of the acceptor excited state A^* is always lower than the energy of the donor excited state D^* . Without additional energy this constrains RET to a single direction, from donor to acceptor.

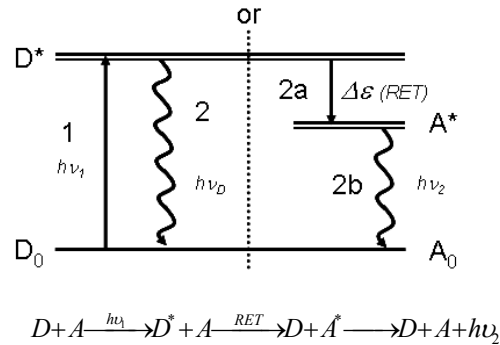


Figure 3-1: Transition energy diagram and expression for RET.

Each chromophore has four (possibly unique) dipoles, two permanent and two transient. The permanent dipoles correspond to the ground state (μ_g) and the excited state (μ_e), while the transient dipoles represent the transitions between these two states: an absorption dipole (μ_{ab}) appears during the transition from the ground state to excited state, and an emission dipole (μ_{em}) appears during the transition from the excited state back to ground state. The transition from a μ_g to μ_e occurs typically in less than 10^{-15} sec due to the purely electronic nature of this process.

The efficiency of RET between donor and acceptor defines the transfer rate, or latency, of an exciton passing through the system. This efficiency also defines important system-level properties such as power consumption, heat dissipation requirements, gain, and the signal-to-noise ratio. Four important parameters relate specific chromophore properties (and relative positions on a nanostructure) to RET efficiency. Table 3-1 identifies these parameters.

Parameter	RET efficiency (Φ_T) scaling law	Description
Chromophore separation (r)	$1/r^6$	Defined by relative placement of chromophores on a nanostructure.
Spectral overlap ($J(\lambda)$)	$J(\lambda)$	Property defined for pairs of chromophores derived from excitation and emission spectra. A measure of how well a donor couples to an acceptor.
Förster radius (R_0)	R_0^6	The separation to achieve 50% efficient RET.
Relative orientation (κ)	κ^2	Trigonometric relationship between chromophore dipoles.

Table 3-1: Parameters that impact RET efficiency

The remainder of this section describes how these four factors can be used to construct basic circuit elements.

3.1.2 Gates

The relative orientation between chromophores (κ^2) is the key parameter that enables switching behavior. By forcing a chromophore's transient dipoles either into or out-of alignment with neighboring chromophores we can induce controlled pass gate or inverting pass gate switching behavior, respectively. To achieve this we propose to exploit the use of electrostatic interactions between chromophores.

The excited state of a nearby chromophore can cause a realignment of a neighboring chromophore's ground state dipole, thus changing the orientation of the chromophore's other dipoles. By careful design/selection of the chromophore, such that permanent and transient dipoles are parallel or perpendicular to the ground state dipole, RET can be controlled. Strong electrostatic interaction (alignment) between the permanent dipoles of chromophores has been demonstrated at close ranges (0.5nm to 2nm) [16, 37].

Figure 3-2 shows our proposed design for an inverting RET pass-gate that contains four chromophores. The input, output, and gate chromophores are rigidly bound to the substrate and the channel chromophore is allowed to rotate in the gate plane. The degree of rotational freedom allowed for each chromophore can be controlled through the specific choice of the molecule used to bind the chromophore to the substrate [81]. In an inverting pass gate the channel's transitional dipoles are parallel to the ground state while a non-inverting pass gate has transitional dipoles that are perpendicular to the ground state [47]. The gate chromophore has perpendicular permanent dipoles (μ_g , μ_e).

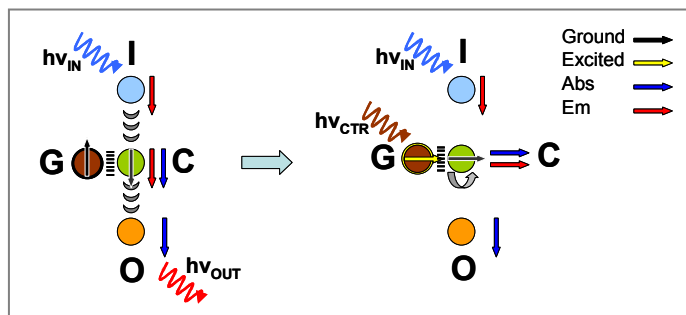


Figure 3-2: Schematic of inverting pass-gate using RET. Gate (G), Input (I) and Output (O) are rigidly bound to the substrate; the Channel (C) can rotate in the pass-gate plane.

When the gate is not excited, the channel's μ_g aligns to the gate's μ_g through electrostatic interaction. The input and output chromophores are chosen to exhibit small μ_g to minimize the electrostatic interaction with the channel. With the channel and gate ground state dipoles aligned, the channel's transitional dipoles (μ_{ab} , μ_{em}) also align with the input and output dipoles, enabling RET (Figure 3-2, left). The pass-gate is in pass mode. When the gate is excited its dipole (μ_e) misaligns the channel to disrupt the RET cascade between the input and output, placing the pass-gate in "high Z" mode (Figure 3-2, right).

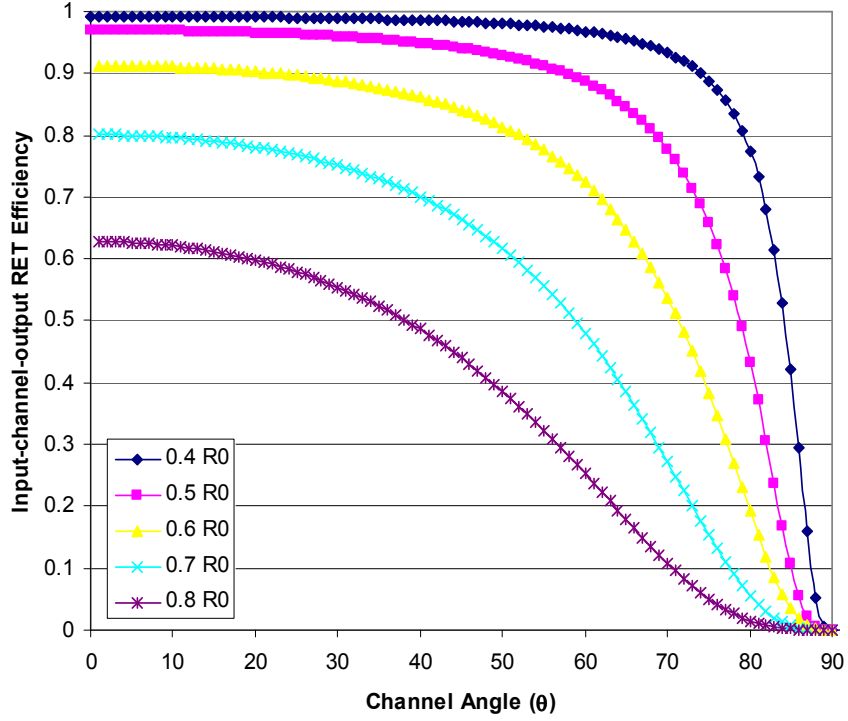


Figure 3-3: Plot of pass gate input-channel-output transfer efficiency vs. channel chromophore angle (θ) for various input-channel-output separations. Channel angle θ is modulated by the gate chromophore.

Figure 3-3 illustrates how control over the relative angle of the channel chromophore influences input-output RET efficiency through the pass gate (Φ_T^2). The gate exhibits switching behavior over a range of chromophore separations and ON/OFF ratios of 10^2 to 10^6 . We expect the switching time of the channel to be ~ 100 ps and the transfer time through the open gate defined by the rate of transfer from input to channel to output (~ 200 ps to 2ns) [47, 93].

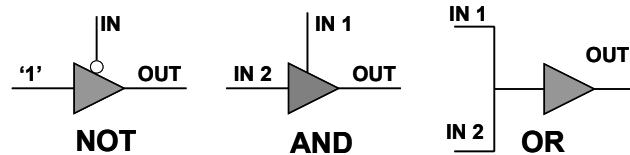


Figure 3-4: Schematic of AND, OR and NOT gates using inverting and non-inverting pass-gates. The OR gate can be implemented as a wired-OR if signal restoration is not required.

The pass gate (both inverting and non-inverting) provides a complete logic family and is the fundamental component on which we build higher-level logic circuits. We are in the process of designing and optimizing the pass gate's configuration on our DNA substrate. We note that other types of gate-channel chromophore interaction, like exciplex formation, could also be employed to enable pass-gate device functionality. Figure 3-4 shows how pass gates, together with wires, can be used to construct digital logic gates like AND, OR and NOT. With RET the equivalent of a wired-OR is possible by selecting two input chromophores that have distinct excitation wavelengths but overlapping emission wavelengths, thus allowing both chromophores to undergo RET with a single output chromophore.

3.1.3 Wires

To be useful for the transfer of information in circuits, RET must permit energy to transfer across long distances (10s of nm). One approach to creating wires is to use multiple different chromophores to form an energy cascade with multiple donor-acceptor steps. One-dimensional multi-chromophore cascades have been demonstrated to carry excited-state energy over distances $\sim 13\text{nm}$ with $> 90\%$ efficiency on linear DNA [58]. Since Φ_T is the per step transfer efficiency, a cascade of n chromophores will have a total efficiency of Φ_T^n , which scales poorly in the length of the cascade. Because of this, although a RET cascade can be used to implement wires, energy migration (EM) is potentially more efficient. Energy migration occurs when the excited-state energy of a donor can diffuse within an ensemble of closely packed homogeneous

donors with the same probability of de-excitation as an individual donor. The implication is that EM along arrays of identical chromophores can extend the distances over which RET may take place well beyond the limits of the Förster radius. The observed timescale for EM is $\sim 10^{-12}$ s / transfer step, which is faster than RET but non-directional.

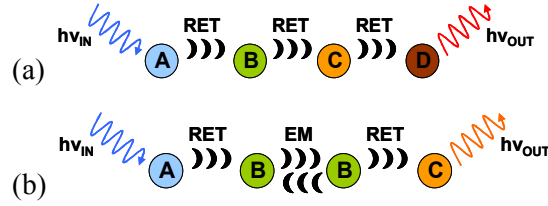


Figure 3-5: Schematic of (a) a 3-step RET cascade and (b) a RET/EM wire on a DNA grid. A photon with energy $h\nu_{in}$ excites A and is transferred through the wire to C (or D) which emits a photon with energy $h\nu_{out}$.

Figure 3-5(a) illustrates a possible 2D energy transfer wire. Chromophore A (the donor) can be excited by a photon from the far-field and, through RET, directionally couple the energy to B, then to C, then D, and ultimately lead to an emitted photon with energy $h\nu_{out}$ (of lower energy due to the Stokes shift effect). Figure 3-5(b) shows an example of a hybrid RET/EM wire. The first chromophore pair A-B is a RET pair that couples energy into a series of EM-coupled chromophores. The output is another RET pair (B-C).

A wire of length L nanometers is expected to have a transfer time of approximately L/r ps (EM) and $10L/r$ ps (RET) for r nm chromophore spacing, where $r \ll R_0$. For wires, the design goal is to minimize r and maximize $J(\lambda)$ and κ^2 within the constraints imposed by the substrate. *The critical substrate requirement is the capability to place chromophores (single molecules) at $r=1\text{nm}-3\text{nm}$ pitch, a constraint easily met with DNA nanostructures.* We also note that spectrally distinct RET or EM wires can cross within very close proximity to facilitate non-planar circuits.

3.2 Integrated RET Technology

Although the pass gates are logically complete, implementing larger logical circuits create challenges with the power supply, energy restoration, feedback, memory, efficient insulation and macroscale I/O. This section describes each of these challenges in detail and proposes solutions that enable the integration of large RET circuits.

3.2.1 Insulators

A critical aspect of any dense computational technology is the prevention of signal interference between independent devices and wires. In conventional CMOS, oxide and minimum physical separation are used to prevent crosstalk, which is unintentional RET in our technology. Our system can employ a similar physical separation by placing molecules at fixed distances from one another. Specifically, since RET degrades as $1/r^6$ the coupling between independent RET wires can be reduced to $\sim 1/X^6$ by a separation of $X \cdot R_0$, or 10^{-7} when $X=10$. Wavelength-multiplexing at the device-level is an alternative to achieve greater device and wire density per wavelength “layer”. Devices in a layer must be separated to prevent crosstalk but can be nearby devices in other layers without penalty.

3.2.2 Signal Restoration: Energy Supply and Feedback

Each step along a RET cascade is energetically downhill. That is, the end of a cascade (long wavelength) can not couple to the beginning of a cascade (short wavelength) without additional energy. However, a complete technology requires feedback from outputs to inputs to implement cross-coupled logic gates or finite state machines. The pass gates presented in Section 3.1.2 can be used to provide signal restoration by inserting NOT gates at the output of each logic module. The constant input to the NOT gate can pass through the buffer and suffers only one loss due to RET.

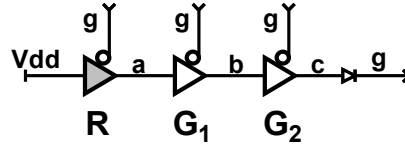


Figure 3-6: Set of RET gates including restoration gate R for feedback and energy supply. Each EM wire is annotated with its exciton frequency band. V_{dd} is the optical pump frequency.

Signal restoration from long wavelengths (low energy) to short wavelengths (high energy) requires additional energy. The proposed pass gates can be used to provide this functionality if the input ‘1’ to the pass gate is generated from an external far-field optical source, called an optical pump, (conceptually analogous to V_{dd}) and the gate is controlled by the signal to either invert or pass. Such gates restore both the frequency as well as the intensity of excitons in a single device. Importantly, since V_{dd} is a far field signal it does not need to be routed.

A set of inverting pass-gates that includes a restoration gate for energy supply and feedback is shown in Figure 3-6. Each EM wire is annotated with its excitation frequency band; V_{dd} is the optical pump frequency and $V_{dd} > a > b > c > g$. In this example the gate inputs of R, G_1 and G_2 use the same frequency g , although this is not required. For each gate, the gating input frequency must be distinct from the source and drain frequencies. Higher frequencies can be converted to lower frequencies “in the wire” using RET cascades that act as down-converting diodes.

An alternative method for signal restoration is to use an external supply that blankets the system with infrared (IR) photons of the necessary energy to amplify the excitation of a given chromophore and thus excite it *energetically backward* to an adjacent chromophore [12]. The specific energy of the IR photons depends on the detailed band structure of the two chromophores but in principle should be in the near- to mid-IR range to achieve an 8x-10x gain.

3.2.3 Memory cells

The ability to restore signals and create circuits with feedback is used to create the D-latch in Figure 3-7 (left). Wires are annotated with excitation frequency (a, b, c, g). To minimize the gate set complexity we assume that all restoring gates (dark gray) have the same output frequency a .

Compared with a standard CMOS design additional pass-gates are necessary to enable 0-to-1 transitions, since the logical zero output of a pass-gate does not have pull-down capability.

Gates are attached to the DNA grid substrate at the interface between tile arms and wires can cross on tile centers. Assuming a half-pitch size L with each tile having length and width $2L$ then the minimum separation is $L\sqrt{2}$.

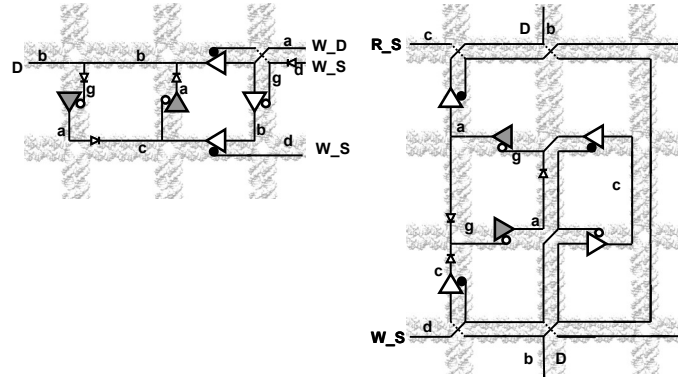


Figure 3-7: Memory latch 20nm x 40nm (left) and memory cell 40nm X 60nm (right)

With our current DNA substrate L is 10nm and the D-latch size is 20nm x 40nm. A more complex 40nm x 60nm SRAM memory cell that can be used for memory arrays is shown in Figure 3-7(right). Signal restoration on directional cell inputs and outputs can be added on the shared connection points between cells.

3.2.4 Decoders, Multiplexers and Adders

Layouts of a 4-way multiplexer and 2/4 decoder with enable input are shown in Figure 3-8a and Figure 3-8b respectively. They measure 40nm x 60nm. A 40nm x 40nm 1-bit full adder cell for arithmetic units is shown in Figure 3-8c.

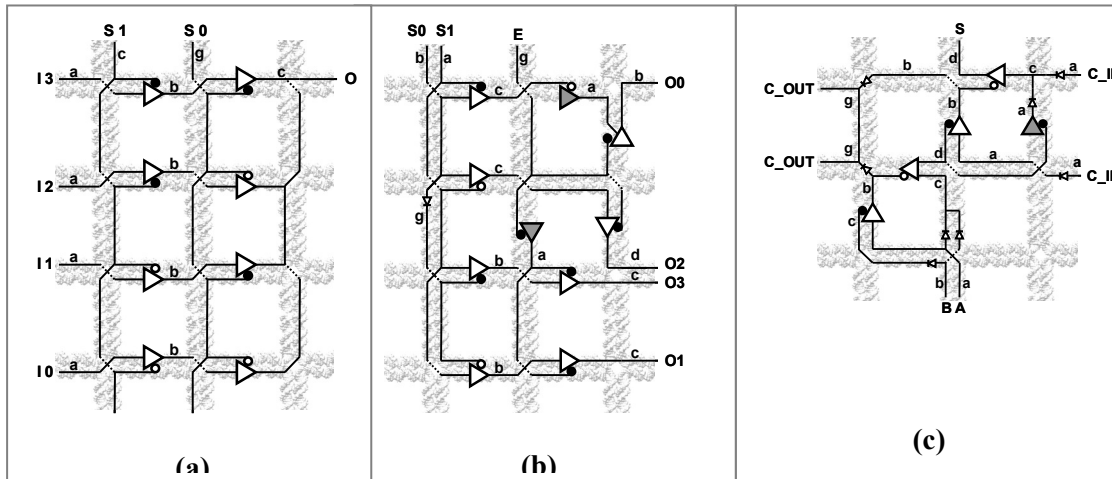


Figure 3-8: (a) MUX4 40nm x 60nm (b) DEC2-to-4 40nm x 60nm (c) 1-bit FA 20nm x 20nm

3.2.5 Macroscale Input /Output

Energy transfer logic does not necessarily require direct addressing of individual components. That is, input signals can be sent into the system and absorbed by any (or all) input chromophores simultaneously. Similarly, output chromophores can be observed by ensemble measurements. This method requires strict wavelength division multiplexing on the inputs, the internal RET wires, and the output chromophores to disambiguate control and output signals. The design challenge is to find instances of chromophores (i.e., real molecular structures) that can satisfy the wavelength and spectral overlap requirements for inputs, wires, gates, and outputs.

3.3 Analysis

To estimate the switching speed and power dissipation of circuits based on RET logic we start from a simple configuration consisting of two pass-gates (A and B) connected by an EM wire (see Figure 3-9). The input to the source of gate A has rate k_{IN} and frequency ν_{IN} . After passing through gate A and through the wire, the rate and frequency at the gate input of B are k_g and ν_g respectively. We consider that with the line asserted (logical “1”) k_g must be at least $1/\tau_{Gex}$ to maintain G in its excited state and gate B in its switched configuration. Given m (3 in this case) RET steps and EM wire of length l , the minimal necessary input rate is $k_{IN\min} \approx (\alpha k_w + k_g)/\Phi_P$ where Φ_P is the overall transfer efficiency of the path. The EM wire can hold up to l excitons; we assume that it must hold at least a fraction α to sustain rate k_g at the output. The circuits in **section 4** show gate-to-gate wire lengths ranging from 10nm to 30nm; for this analysis we assume l to be 20. We use this simple model to derive order-of-magnitude estimations for RET logic switching time and power dissipation.

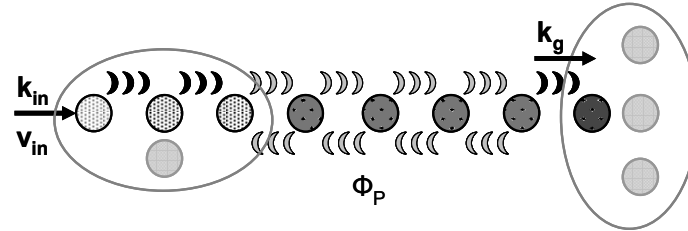


Figure 3-9: Latency and power dissipation analysis: the drain output of one pass-gate connects to the gate input of another through an EM wire.

Table 3-2 below shows the estimated characteristics of a single gate-wire-gate path. Given the calculated $\sim 70\%$ transfer efficiency, the necessary input excitation rate is estimated at 8.4 GHz and the switching time is approx. 2ns. The length of the EM wire has a large impact on dissipated power and must be considered when optimizing circuit layouts. Given a high gating

factor, most power is dissipated when the path is in the asserted state with the input gate in pass mode. The two main sources of thermally dissipated energy are the Stokes shift (down-frequency) inherent in each RET step and non-RET induced de-excitation. A significant fraction of the latter is generally not thermalized but emitted as far-field fluorescence photons.

Table 3-3 shows the estimated power consumption of a node of 150x150 tiles with 22,500 restoring gate-wire-gate paths to be in the μW range. As the next section shows, we think that a node of this size can implement a basic computational device.

Parameter	Description	Nominal values
τ_{rot}	Rotational correlation time of channel	10ps
τ_{Gex} , k_g	Excited lifetime and rate of gate	1ns, 1 GHz
τ_{Wex} , k_w	Excited lifetime and rate of a single EM chromophore	2ns, 0.5 GHz
Φ_{RET} , τ_{RET}	Efficiency and time for RET step	0.9, 100ps
Φ_{EM} , τ_{EM}	Efficiency and time for EM step	0.999, 1ps
m	Number of RET steps	3
l	Number of EM steps	20
α	Fraction of excited EM chromophores in wire necessary to sustain k_g at the output	0.5
$\Phi_P = \Phi_{RET}^m \Phi_{EM}^l$	Input to gate path efficiency	0.71
$k_{IN\min} \approx (\alpha k_w + k_g) / \Phi_P$	Input excitation rate that generates k_g	8.4 GHz
$t_{1prop} \approx \alpha l / k_{IN} \Phi_P + \tau_{rot}$	Transition time for low-to-high	1.8ns
$t_{0prop} \approx \tau_{Wex} + \tau_{rot}$	Transition time for high-to-low	2.1ns

Table 3-2: RET path model

N	Number of restoring gates connected to pump	22,500
f_{th}	Ratio of radiative vs. non-radiative (i.e., thermalized) excitation loss	0.1
$P_{1_Stokes} \approx N[k_g h(\nu_{IN} - \nu_{OUT}) + \alpha k_w h(\nu_{IN} - \nu_{Wire})]$	Energy thermalized on all N gates due to Stokes shift in “1” state (600nm input, 625nm wire, 650nm output)	2.1 μ W
$P_{1_th} \approx Nk_{IN\min} f_{th} h \nu_{IN} + P_{1_Stokes}$	Total energy thermalized in “1”	8.3 μ W
$P_{01_th} \approx N[k_{IN\min} f_{th} (1 - \Phi_p) h \nu_{IN} + k_{IN\min} \Phi_p h(\nu_{IN} - \nu_{Wire})]$	Total energy thermalized in “0-1”	1.8 μ W
$P_{10_th} \approx N\alpha k_w f_{th} h \nu_{Wire}$	Total energy thermalized in “1-0”	3.6 μ W

Table 3-3: Estimate node power consumption

3.4 Application Domains

Given the above circuit elements it is possible to construct a simple computational node on a single large DNA grid. Although large periodic DNA structures have been demonstrated, we assume the size of aperiodic structures is limited to 150x150 cruciform tiles, or a total of 22,500 tiles. Given our mapping of two primitive logic gates per tile, we have 45,000 total gates per node. This is twice as many as previously proposed DNA self-assembled carbon nanotube designs [61, 62] and could contain, for example, an 8-bit accumulator-based CPU core and 128 bytes of memory.

In Chapter 4 we demonstrate the application of RET logic devices for microenvironment sensing applications and in Chapter 5 we explore in detail the ISA design space and trade-offs for bio-compatible integrated computing and sensing nodes.

3.5 Towards a prototype

This section presents our initial results in working toward molecular-scale computing. The purpose of this experiment is to demonstrate two main points: 1) that with the DNA grid we can place chromophores sufficiently close to achieve RET interaction, and 2) to demonstrate simple wired-OR RET behavior.

The 60nm x 60nm DNA grids we use are developed in our laboratory using methods described in Chapter 2. We initially extended the protein patterning method (see Chapter 2.2.4) to use proteins functionalized with chromophores. To test for RET transfer the proteins (with attached chromophores) were assembled in two different configurations: one in which they were attached to neighboring grid centers and another in which they were one tile apart. Figure 3-10 shows AFM images of the resulting grid structures. Each protein was functionalized with a single chromophore type (top protein with Oregon Green 488, bottom protein with Marina Blue).

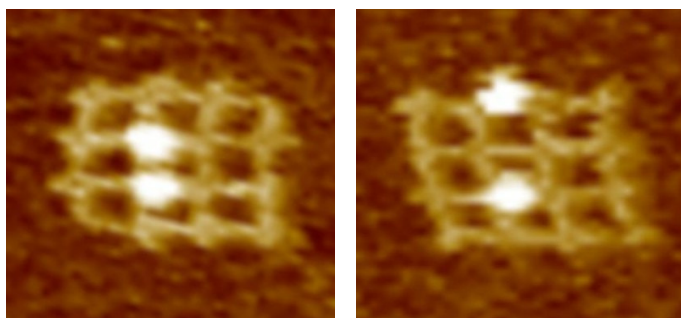


Figure 3-10: AFM images of DNA grids patterned with chromophore-functionalized proteins. The configuration on the left has closer spacing (~15nm) than the one on the right (~35nm). Each grid cavity is ~20nm wide.

We compared the ensemble spectral response from the two configurations to identify any change due to changes in RET efficiency induced by variation in chromophore separation. However, the RET efficiency in either configuration was too low to be detected with our instrumentation. Even when placed on neighboring tiles, the protein-bound chromophores are

~15nm apart, more than twice their Forster radius. Closer spacing was needed in order to achieve efficient RET.

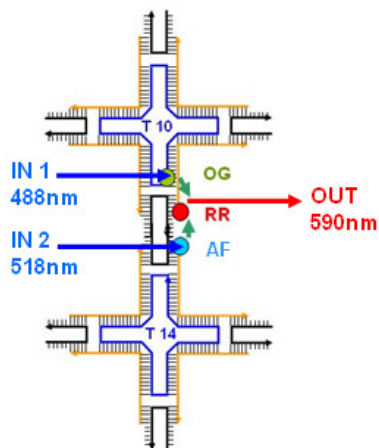


Figure 3-11: Schematic of OR gate.

Using chemistry similar to that used to attach proteins it is possible to attach chromophores directly to specific sites on the DNA grid. We used available sites at the intersection between motifs with a spacing of ~1.3nm. We designed a wired-OR gate using three chromophores, two for the input signals (Oregon Green and Alexa Fluor 535) and one for the output signal (Rhodamine Red) attached to the grid as shown in Figure 3-11. The two inputs are excited by wavelengths of light at 488nm and 518nm for Oregon Green and Alexa Fluor 535 respectively. The input chromophores undergo RET with the Rhodamine Red output chromophore, which has an emission peak at 590nm.

Input 1 (488nm)	Input2 (518nm)	RET Output (590nm)
OFF	OFF	0
ON	OFF	39
OFF	ON	31
ON	ON	70

Table 3-4: Observed RET output (in optical fluorescence counts) from the OR-gate under 488nm (IN 1) and 518nm (IN 2) excitation

We experimentally assembled DNA grids with the attached OR-gates as described above. A fluorometer measures the output of the assembly in the 300-800nm range under various input conditions. Input excitation is generated by a custom dual-beam excitation source. We estimate that the sample contains $\sim 10^{12}$ gates and the output for 488nm (IN 1), 518nm (IN 2) and simultaneous 488nm/518nm (IN 1 + IN 2) excitation is shown in Table 3-4. We isolate the specific contribution of the output (RR) chromophore due to RET from the background fluorescence by subtracting the normalized readout of a baseline grid assembly with the same chromophores placed at distances much greater than their respective Forster radii (thereby preventing RET).

These results demonstrate the capability to place three chromophores sufficiently close to transfer excited-state energy from two distinct inputs to the same output, characteristic of an OR-gate. As part of our future work we are exploring the fabrication of the proposed inverting and non-inverting pass gates.

3.6 Related Work

Researchers have demonstrated molecular constructs capable of implementing basic Boolean logic gates[6, 18, 31, 91] and a variety of logic functions[8, 54, 55] in a range of chemical environments, including on cellular biological substrates[70, 75, 101]. However, scaling

these devices to larger computing systems is still an open challenge because of use of chemical inputs and outputs, multiple representations for binary signals and susceptibility to cellular processes. RET-logic devices present an uniform representation of signals and can selectively interface with biological markers for integrated sensing applications.

Electronic devices like carbon nanotube[5, 109]and nanorod[43] FETs can provide the basis for both computation and sensing, however the lack of control over precise device length and positioning and the difficulty of electronic macro-scale interfacing (pitch matching) make it difficult to assemble complex integrated systems. In contrast, RET-logic elements can be constructed using the precise positioning features of self-assembled DNA grids and use optical signals that do not require macroscale-to-nanoscale I/O wire routing.

Optical switches[11, 34, 41], logic elements [4, 68] and waveguides [40, 58] are promising candidates for molecular computation. Their optical addressing provides an efficient method for macro-scale interfacing, but inter-connectivity of individual devices remains a challenge [18]. We propose inter-connectable RET-logic devices that can exploit the chemical programmability of DNA grids to assemble complex circuits.

DNA computing[2] is a technique that uses DNA hybridization rules directly to perform combinatorial computation. Our approach is different in that we use DNA as a chemically addressable substrate for the active RET-logic computational devices.

3.7 Conclusion

Nanoscale computing may open new areas to apply the power of computation, such as biologically compatible computation. While there is currently no clear winner in the nanoscale arena, this chapter maps out one path toward a molecular-scale computing substrate. We show how DNA-based self-assembly can be used to place optically active single molecules (called chromophores) with nanometer to Angstrom precision. The theoretical foundation of our devices

and circuits is Resonance Energy Transfer (RET) and we propose a new optically switched gate designed using four chromophores. We introduce RET-logic, a complete technology based on chromophores, and show how to design and layout (by hand) several circuit elements. The densities achievable on existing DNA nanostructures results in a D-Latch occupying 20nm X 40nm, a complete SRAM cell occupying 40nm X 60nm, and a full adder occupying 40nm X 40nm, new nanostructures could further improve densities. We present results from analytic evaluation of switching time and power consumption for the proposed devices. We also present our first steps to fabricating a prototype system. This includes the DNA nanostructures and the creation of a chromophore-based wired-OR gate. While this is only a first-step, it demonstrates the ability to precisely control single-molecule placement and to interface with the devices at the macro-scale.

RET logic devices could be used to create biologically compatible computation elements. In the next chapter we demonstrate the integration of RET logic gates with sensing in the context of a sample bio-molecule detection application and in Chapter 5 we analyze the design space of nanoscale sensor processors (nSP) capable of complex integrated computation and sensing.

4 Nanoscale Sensing

The self-assembly of nanoscale logic circuits has great potential as an economical and massively parallel method to create computer systems and will play an increasingly important role in technology as the resolution and manufacturability of current microelectronics processes begin to reach fundamental limits. In this context, DNA self-assembly has the potential to expand the domain of conventional computer systems to reach into environments and application domains that are otherwise impractical such as single-cell sensing or microenvironmental monitoring. In this chapter we demonstrate a method of sensing which uses DNA self-assembly to integrate computation and the ability to detect biomolecules in small volumes at the nanoscale. This application domain is new for computer systems and paves the way for more sophisticated applications of computing in biological systems. We present results which demonstrate that nanoscale RET-logic circuits formed by DNA self-assembly can be operated similar to conventional logic devices and, in an example application, can detect femtomole quantities of biomolecules like proteins and short fragmentary nucleic acids.

In this work we use DNA-guided self-assembly to position chromophores with molecular precision into optical gate configurations (as shown in Section 3.5) and place multiple externally addressable gates on a single DNA scaffold, leading towards integrated optical molecular logic systems. We illustrate a biosensing application in which the gate output is modulated in the presence of target analytes.

The remainder of this chapter is organized as follows. We begin with a theoretical description of RET for systems with multiple chromophores in Section 4.1. We describe the assembly methods in Section 4.2. We present the RET system design and experimental sensing results in Section 4.3. We analyze the underlying mechanism for sensing in Section 4.4. We discuss the scaling to larger circuits in Section 4.5 and we conclude in Section 4.7.

4.1 Resonance energy transfer

To implement our logic devices we take advantage of RET as the underlying mechanism to couple energy from a source (donor) chromophore to its destination (acceptor) chromophore. The transfer resembles electronic current rectification since the excited-state energy of the donor transfers to the acceptor but not vice versa, much like electron and hole currents in a PN diode. To implement logic we use wavelength division multiplexing to selectively excite donors which represent inputs to our system. A donor input is excited by the absorption of a photon and transfers this energy to a nearby acceptor. Upon excitation by RET the acceptor relaxes by spontaneous emission of a photon with lower energy. The rate of this process was first derived by Förster based on classical charge dipole-dipole coupling and quantum mechanics and is

$k_{RET} = k_D \left(\frac{R_0}{r} \right)^6 = k_D \cdot \gamma^6$, where k_D is the emission rate of the donor without RET to any acceptor, r is the distance between the acceptor and donor, and R_0 is the Förster radius, or distance at which RET occurs with 50% efficiency[47, 93], and $\gamma = R_0/r$. The transfer rate between donor (x) and acceptor (y) defines an efficiency for this process of

$$\Phi = \frac{k_{RET}}{k_D + k_{RET}} = \frac{\gamma^6}{1 + \gamma^6}, \text{ which follows a characteristic } r^{-6} \text{ scaling law.}$$

The rate of energy transfer between a donor and acceptor is a function of their relative alignment, separation, and surrounding medium. The Förster radius is defined for a pair of chromophores (x, y) as $R_0^{x,y} = 0.211 \cdot [\kappa_{x,y}^2 \eta^{-4} Q_x J(\lambda)]^{1/6}$, where η is the refractive index of the medium, Q_x is the quantum yield of the donor in the absence of acceptor, $J(\lambda)$ quantifies the spectral overlap between donor emission and acceptor absorption and $\kappa_{x,y}^2$ is a time-averaged factor describing the relative orientation between the two molecules. The sensitivity of the RET

process to the distribution of acceptor-donor distances has led to its use as a ‘spectroscopic ruler’ by which a certain linearity in response to separation is expected[88]. However, at distances very different than R_0 , the rate of transfer is either saturated or negligible, all else being equal. Thus, at short separations the transfer rate is more strongly dependent on changes in κ or η than r .

For low excitation intensity, i.e., in the regime where transfer rates are linear and independent, and when multiple possible donors (or acceptors) exist the fluorescent emission rate of a chromophore is defined as $k_D^x = k_{D_0}^x + \sum k_{RET}^{i,j}$, where $k_{D_0}^x$ is the rate of the donor (x) decay in the absence of acceptors and $k_{RET}^{i,j}$ is the rate for RET between pair (i, j) over all possible pairs in the system. This leads to an overall transfer efficiency of $\Phi_{xy} = k_{RET}^{x,y} / k_D^x$ as before and is identically $\frac{\gamma_{x,y}^6}{1 + \gamma_{x,y}^6}$ for only one pair of chromophores. For multiple pairs we can define the

transfer efficiency for pair (x, y) as $\Phi_{x,y} = \frac{k_{RET}^{x,y}}{k_{D_0}^x + \sum k_{RET}^{i,j}}$. In practice, $\Phi_{x,y}$ deviates from this simple description due to partial pair formation and microenvironment factors. We account for this later by adjusting the transfer efficiency by an experimentally determined fraction of correctly formed donor-acceptor pairs in our system.

Multiple nearby acceptors provide additional pathways for the relaxation of a donor and, for low intensity sources, the rate can be described by a linear combination. The rate of fluorescence for a chromophore among multiple acceptors is

$$F_x = \left(1 - \sum_{i \neq x} \Phi_{x,i}\right) \cdot \left[E_x + \sum_{i \neq x} (\Phi_{i,x} \cdot E_i)\right], \text{ where } n \text{ is the number of chromophores in the}$$

system and E_x is the rate of chromophore excitation due to external sources. The first term in F_x is the radiative decay efficiency of the chromophore and the second term is due to direct and RET

excitation. To define the excitation rate for a chromophore excited by m possible sources we assume single-band, single-photon absorption and a linear combination of rates such that

$$E_x = \sum_{i=0}^m I(\lambda_i) \cdot A_x(\lambda_i) \cdot \varepsilon_x(\lambda_i) \cdot Q_x(\lambda_i), \text{ where } I \text{ is the source intensity, } A \text{ is the}$$

absorbance of the chromophore, ε is the molar extinction coefficient, Q the quantum yield and each quantity is wavelength dependent.

The ensemble response, $\sum F_x$, is observable as steady-state fluorescence spectra and can be used to define an index of RET activity within an experimental system. We use the relative intensity of acceptor fluorescence between two narrow bands to serve as our RET index defined as

$$I_{RET}(\lambda_1, \lambda_2) = \frac{\sum_x F_x \cdot c_x^{\lambda_1}}{\sum_x F_x \cdot c_x^{\lambda_2}}, \text{ where } c_x^{\lambda} \text{ describes the fraction of total fluorescence from a}$$

chromophore that can be observed in a narrow spectral window centered on λ as defined by

$$c_x^{\lambda} = \frac{\int_{\lambda-\mu}^{\lambda+\mu} F_x \cdot d\lambda}{\int_0^{\infty} F_x \cdot d\lambda}, \text{ where } 2\mu \text{ is the width of the spectral window.}$$

Thus, I_{RET} can be calculated from observed ensemble steady-state fluorescence at two wavelengths and can yield detailed information about time-averaged donor-acceptor configurations (e.g., $\kappa_{x,y}^2$ and $r_{x,y}$) by standard non-linear least squares fitting. Later, we show how a change in I_{RET} (i.e., $\Delta I_{RET} = [I_{RET}(\text{final}) - I_{RET}(\text{initial})] / I_{RET}(\text{initial})$) is an output-indicator for our logic gates and how such systems can be multiplexed to detect distinct molecular species in solution.

4.2 DNA self-assembled RET circuits

We use DNA self-assembly to create nanoscale grids on which chromophores can be precisely patterned. Figure 4-1 is an atomic force microscopy image of a 60nm X 60nm DNA grid assembled using 4x4 tile motifs[59, 65, 105]. Briefly, we assemble each of 16 tiles independently and choose the DNA sticky-ends such that each tile will bind at only one position in a 4x4 grid (see Section 2.1). Since we form each tile independently, we can selectively functionalize the DNA strands and after assembly form a grid with a precise chemical pattern. In this work, we use 5'-SH end functionalization to conjugate commercially available chromophores at precise locations on the grid (Appendix 1.1).

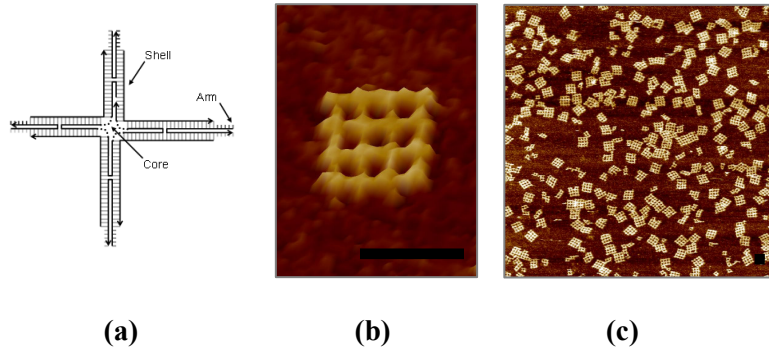


Figure 4-1: Cruciform tiles (a) are assembled from nine DNA strands. AFM images of grid structures composed of 16 tiles are shown in (b) and (c). Reference bar length is 60nm.

Resonance energy transfer can be used to implement logic gates by creating patterns of multiple input donors that share a single output acceptor. The output of the logic gate can be detected by observing a change in I_{RET} due to a change in the input excitation. This arrangement can be tuned by changing donor-acceptor separations such that a specific number of excited donor inputs are needed to generate a given level of acceptor fluorescence. Abstractly this is an n -out-of- k logic gate, a generalization of the Boolean AND-gate, and requires the precise placement of chromophores at distances comparable to R_0 . Since DNA nanostructures can place chromophores at resolutions approaching the helical pitch (3.4 Å) our DNA grid is well suited to this purpose.

4.3 RET logic gates and sensing

To implement a multiplexed sensor we create a digital multiplexer in series with site-specific receptors on the DNA grid that can interact with analytes in solution. In general, a multiplexer takes binary encoded inputs and selects a specific output corresponding to the input. That is, an n -input multiplexer with 2^n outputs energizes the one output specified by the input. Typically, multiplexers steer logic values around more complex circuits but they can also be used to detect abnormal conditions at each output. For example, if all outputs from the multiplexer are observed in parallel (e.g., an implicit OR-gate) an observer can detect if any output is faulty by iterating through the input space and recording the ensemble response. Any low value in the response indicates that the selected output was attenuated. In our system we exploit the site specific binding of biomolecules to disrupt the multiplexer to create optically addressable sensors.

To demonstrate multiplexed sensing we use two RET AND-gates on the DNA grid (Appendix 1.1.2) and, by ensemble observation of I_{RET} , view the system as a simple logic circuit (Figure 4-2). We place analyte receptors (e.g., complementary DNA, locked-nucleic acid (LNA), or biotin) at intersections between tiles (Appendix 1.1.3-1.1.5) to disrupt the output of an AND-gate through competitive binding between the adjacent DNA sticky-ends and the analytes (26-nt DNA, 5-nt RNA, or streptavidin) which represent biomolecules of interest (e.g., miRNAs, metabolic proteins, etc.). Each AND-gate is composed of one unique input chromophore (Gate 1: PacificOrange™, λ_{ex} =400nm; Gate 2: OregonGreen™, λ_{ex} =496nm) and one common input (AlexaFluor™ 530, λ_{ex} =528nm) chromophore to demonstrate (1) that RET can implement logic for multiplexers and (2) a path toward scalable (i.e., high density) multiplexed sensors beyond what is feasible with simple wavelength multiplexing with many unique chromophores.

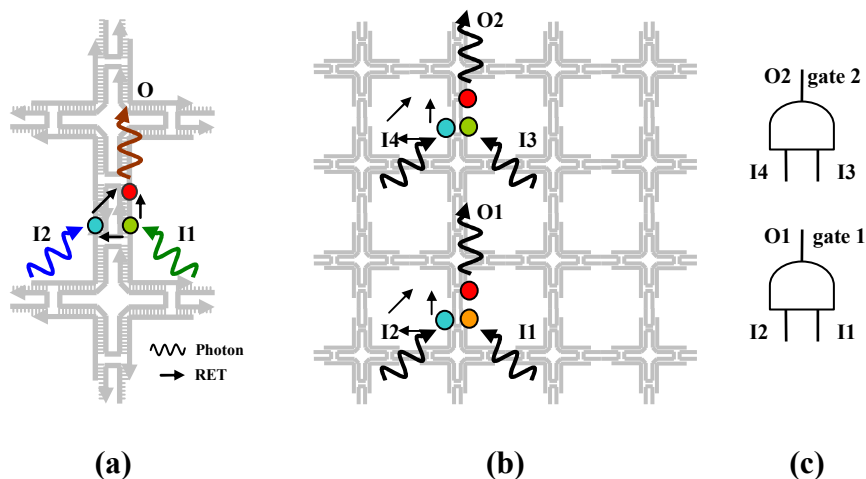


Figure 4-2: Optical gates: Chromophores are attached to 5' and 3' ends of shell strands with input chromophores on one tile and the output on the neighboring tile (a). The inputs and the output are separated by the 5bp inter-tile sticky-end arm. We place two gates (b) on the 16-tile grid structure. The gates share chromophore types on output (O1, O2) and one of the inputs (I2 and I4). Abstractly, the system is a collection of simple logic circuits (c) consisting of two AND-gates.

We have found that we must partially melt the grid to make the target site near the AND-gate output labile to analyte (Appendix 1.2.1). In the presence of an analyte, and upon heating (37 °C) and annealing back to low temperature (18 °C), we observe the change in I_{RET} using two 10nm wide spectral windows centered on $\lambda_1=553\text{nm}$ and $\lambda_2=589\text{nm}$ for each gate's output chromophore to conclude the identity of any analytes present in the solution (Figure 4-3).

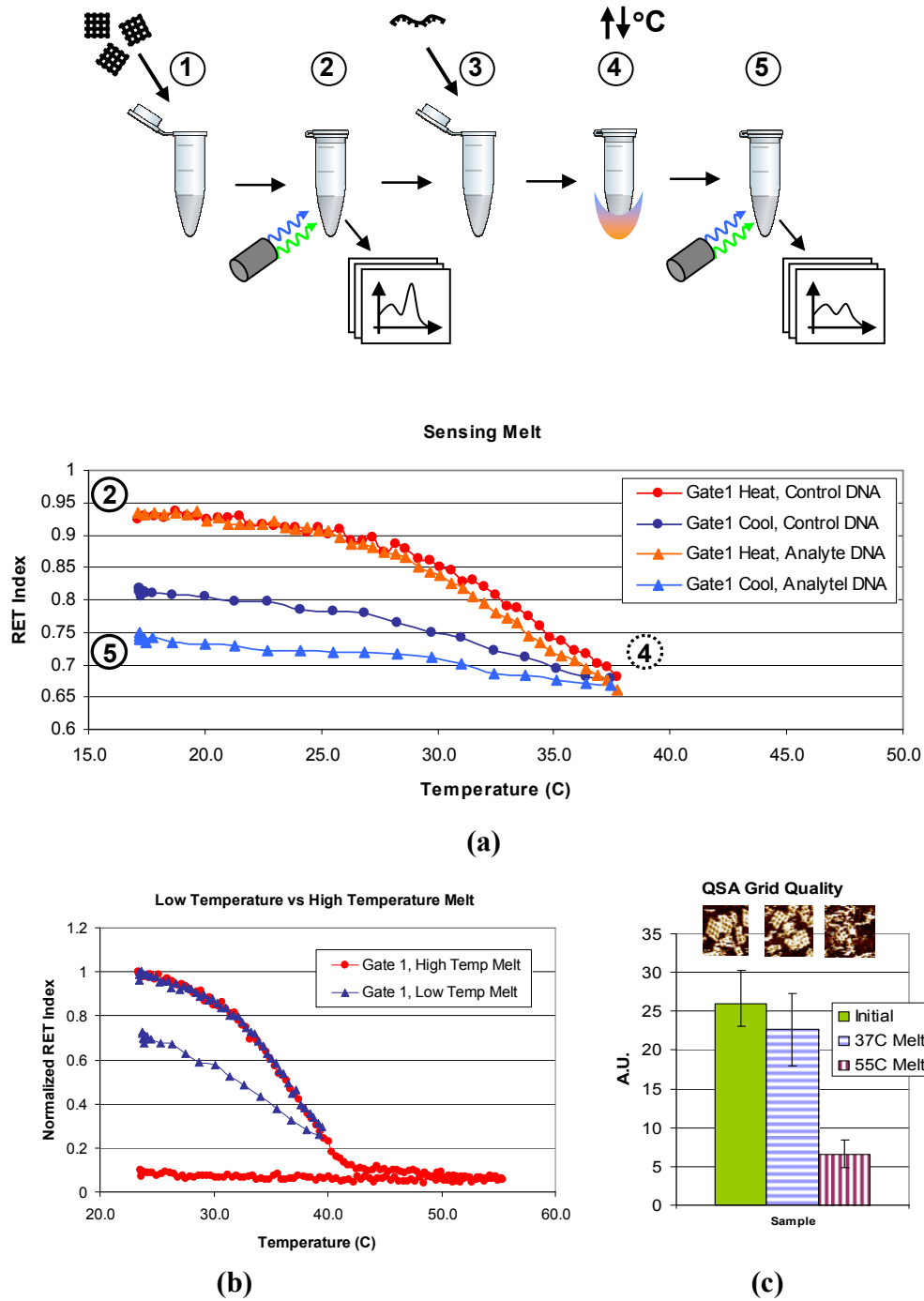


Figure 4-3: Sensing process overview: DNA grids (1) with attached chromophores are added and an initial optical readout of all gates is performed (2). After adding the analytes (3) the sample is heated (4) to 37°C (12min) and subsequently cooled back to 18°C (30min) using two baths and closed-loop temperature feedback to ensure repeatability. A final optical readout is performed (5) and the I_{RET} values are calculated for each acquired spectrum and the relative variation from initial values is recorded (ΔI_{RET}). The RET index

variation of Gate 1 in a grid with the two-gate configuration is shown in (a). We continuously monitor two samples, one including the target analyte (e.g., ssDNA) for Gate 1 and one including a control strand. The I_{RET} drops as temperature increases, (2) to (4). After cooling, the control sample shows higher I_{RET} than the sample with target analyte present. Increasing the melting temperature to 55°C shows an irreversible drop in I_{RET} suggesting structural damage, (b) (data corrected for fluorescence level and temperature dependence – see Appendix 1.2.1). The same conclusion is supported by AFM analysis in (c) where the QSA metric shows a small decrease in grid structure quality after the low-temperature melt and a large degradation after the high-temperature melt.

Since the DNA sticky-ends may displace the analyte upon annealing we choose either a receptor with very high affinity (e.g., biotin for streptavidin), design the sticky-ends to be fully complementary to the analyte (e.g., DNA), or use LNA which can selectively enhance binding with the RNA analyte.

An analyte can be detected by this method if its dissociation rate constant (K_D) is comparable or smaller, due to the partial melting process, than the sticky-end dissociation rate constant at room temperature. We approximate the cooperative dissociation rate constant by

$$K_D = \exp\left(\frac{\Delta H_1 + \Delta H_2}{RT} \left(\frac{1}{T_{m1} + T_{m2}} - \frac{1}{T}\right)\right), \text{ where } \Delta H_1, \Delta H_2, T_{m1}, T_{m2} \text{ are defined by the}$$

nearest-neighbor model[73], for the two 5-nt sticky-ends holding the gate output chromophore near the inputs ($K_D \approx 10^{-1}$). The actual dissociation rate constant must be smaller than this since we observe many intact grid structures at room temperature, however longer range cooperative interactions along the DNA helix are ignored in this approximation[56]. In the case of DNA sensing, the 26-nt analyte strands have two 5-nt regions at each end which are complementary to the sticky-ends of either gate. Since the sticky-ends have the same dissociation rate as the regions of the analyte which bind, non-Watson Crick interactions between the middle of the analyte strand and the surrounding DNA is the likely cause of a reduced dissociation rate after the partial melt. Thus, the analyte strand is detectable and we also show that the binding of the 5-nt end regions to the sticky-ends is sequence specific. In the case of RNA sensing, the 5-nt analyte

strand is complementary to only one (LNA) sticky-end near the gate output. Since RNA-LNA interactions are stronger than identical RNA-DNA interactions[90, 94], the 5-nt RNA analyte can successfully displace the complementary DNA sticky-end and thus be detected. In the case of protein sensing, the streptavidin-biotin dissociation rate ($K_D \approx 10^{-15}$)[14, 99] is substantially smaller than the DNA sticky-end dissociation rate and easily detectable. To facilitate gate output disruption we use three biotins (attached to three shell strands, see Appendix 1.1.5) in the 8-nm³ vicinity of the chromophores. However, our supporting AFM data (see Appendix 1.1.5) shows that only one protein binds to any single gate which is most likely due to steric occlusion by the ~4-nm wide streptavidin.

Control experiments indicate that non-competing (i.e., non-complementary) nucleic acids (DNA or RNA) do not appreciably change I_{RET} , however non-competing proteins like bovine serum albumin (BSA) show a noticeable modulation but do not interfere with the binary discrimination of any analyte identity. A likely explanation is that non-specific interactions between the hydrophobic regions of the chromophores, DNA, and BSA change the helical conformation near the gate and thus modulate I_{RET} . Further, we found that non-specific fragmentary RNA (5-nt) does not appreciably modulate I_{RET} at non-LNA sticky-end sites.

Since partially melting the grid can also lead to disruption of the AND-gates, even without analyte, we first characterize this disruption by monitoring I_{RET} during the melt and determining post-melt structural yield of the grids by AFM. Yield information is derived from AFM images of DNA lattice structures by counting the number of square cavities in a given image relative to the coverage of DNA and normalizing the result to an idealized case of perfectly formed structures. We call this metric the Quality of Self-Assembly (QSA)[53]. We have found that melting to 37 °C does not appreciably disrupt the grid structure yielding a 14% change in I_{RET}

upon re-annealing and a 12% change in QSA, while still making the analyte binding site accessible.

Figure 4-4 presents the response of the two AND-gate system while varying the analyte conditions and input excitations that target each gate. The error bars in Figure 4-4 are derived from the minimum and maximum change in ΔI_{RET} across three or more identical experiments made from the same stock of circuits. Horizontal lines are drawn to indicate the ΔI_{RET} value that serves as the binary decision threshold to determine the presence of an analyte. The noise margin for both gates is greater than about 3X for the DNA sensing experiments and approximately 1.5X for the RNA and protein experiments. This change in signal is sufficiently larger than the noise to make a 100% determination of each analyte.

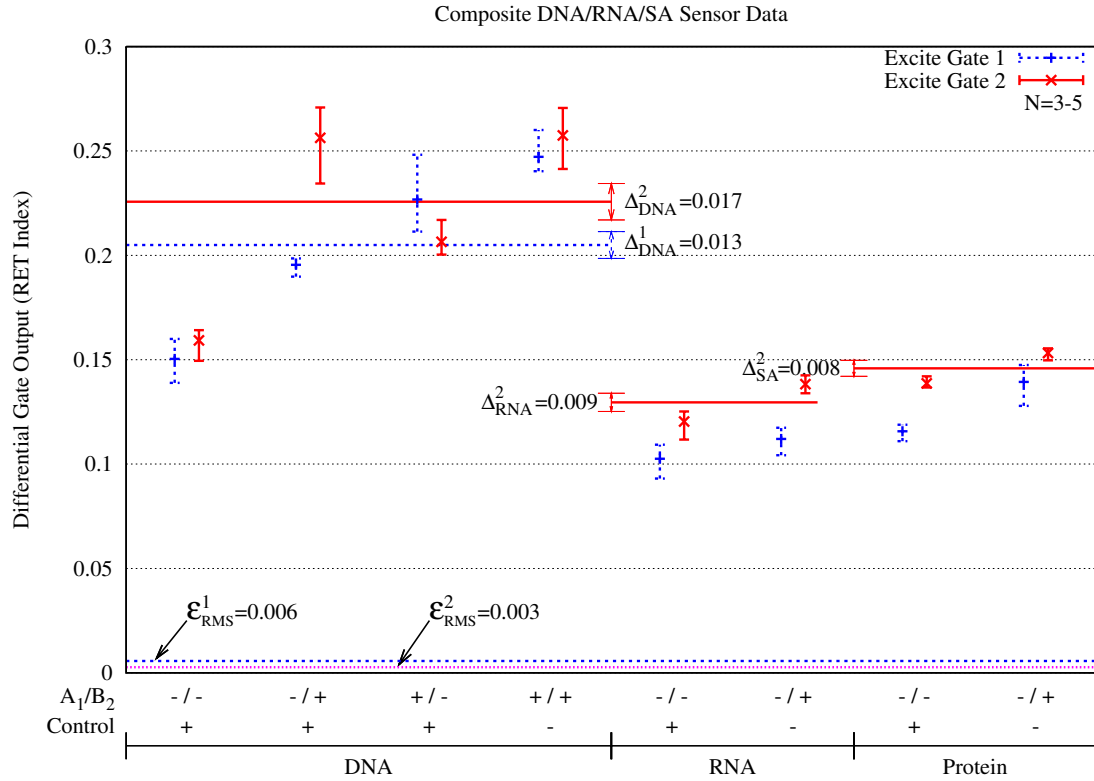


Figure 4-4: Two AND-gate response across DNA, RNA, and protein analytes. Gate 1 is designed to be sensitive to analyte A (A_1) and Gate 2 to analyte B (B_2). For DNA sensing A, B and the control are 26-nt DNA strands (Appendix 1.1.3). For RNA sensing B and the control are 5-nt RNA strands (Appendix 1.1.4) where Gate 2 is modified to include an LNA sticky-end. For protein sensing B is streptavidin and the control is bovine serum albumin where Gate 2 is modified to include a biotin next to each chromophore. The noise margin around each decision threshold (Δ^1 and Δ^2 , respectively) is shown for comparison to the RMS noise for each gate (ϵ^1 and ϵ^2 , respectively). For DNA sensing there are two thresholds corresponding to each gate's sensing decision. For the RNA and protein experiments a single threshold is used since only one gate is selectively targeted (Gate 2). The ΔI_{RET} threshold for all analytes is above the noise floor and is reproducible.

We have also characterized the sensitivity of our system to various analyte concentrations to determine the detection limit and feasibility of using ΔI_{RET} to deduce an activity factor and the concentration of each analyte. Figure 4-5 shows the observed change in I_{RET} for gate 1 and gate 2 as a function of concentration for the DNA analyte (26-nt) that targets gate 2. In practice, we vary the ratio of analyte to a fixed concentration of DNA grid (4 nM) to achieve different analyte concentrations. We determined the limit of detection for our setup by finding the analyte

concentration at which we could no longer distinguish between the two gate outputs. We found that with a commercial CCD spectrometer and short exposures (~ 2 min) the detection limit is approximately 4 nM at an analyte to grid ratio of 1:1. We estimate our observation volume to be 25 μL by geometric arguments (Appendix 1.2.2) and thus can detect a lower limit of 8 femtomoles of DNA analyte. Single-photon detection methods will further reduce this detection limit by enabling few- and single-grid measurements. By using a minimum concentration of grid, as limited by the sensitivity of the optical setup, the concentration of analyte can be in excess and thus maximize the binding activity and observed change in I_{RET} .

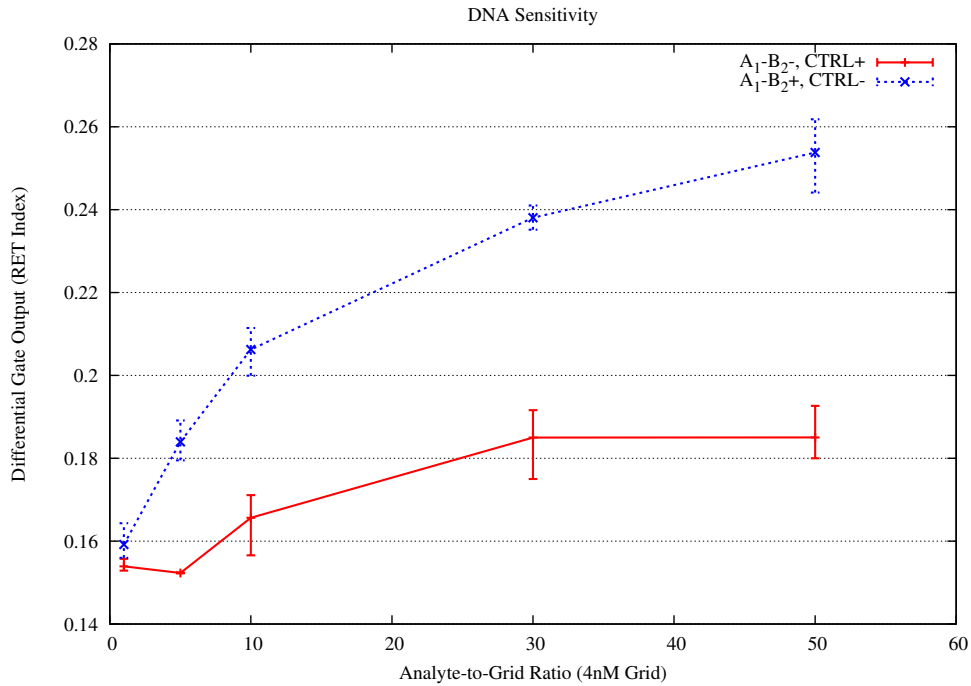


Figure 4-5: Sensitivity to various analyte concentrations. Figure shows the observed change in I_{RET} for gate 1 and gate 2 as a function of concentration for a DNA analyte (26-nt) that targets gate 2. We vary the ratio of analyte to a fixed concentration of DNA grid (4 nM) to achieve varying analyte concentrations (4-200 nM). With an unsophisticated, portable commercial CCD spectrometer and short exposures (~ 2 min) the detection limit is approximately 4 nM at an analyte to grid ratio of 1:1.

Figure 4-5 shows that the change in I_{RET} is monotonic in concentration which indicates, over the range of 4 to 240 nM, the gate output is useful for estimating analyte concentration.

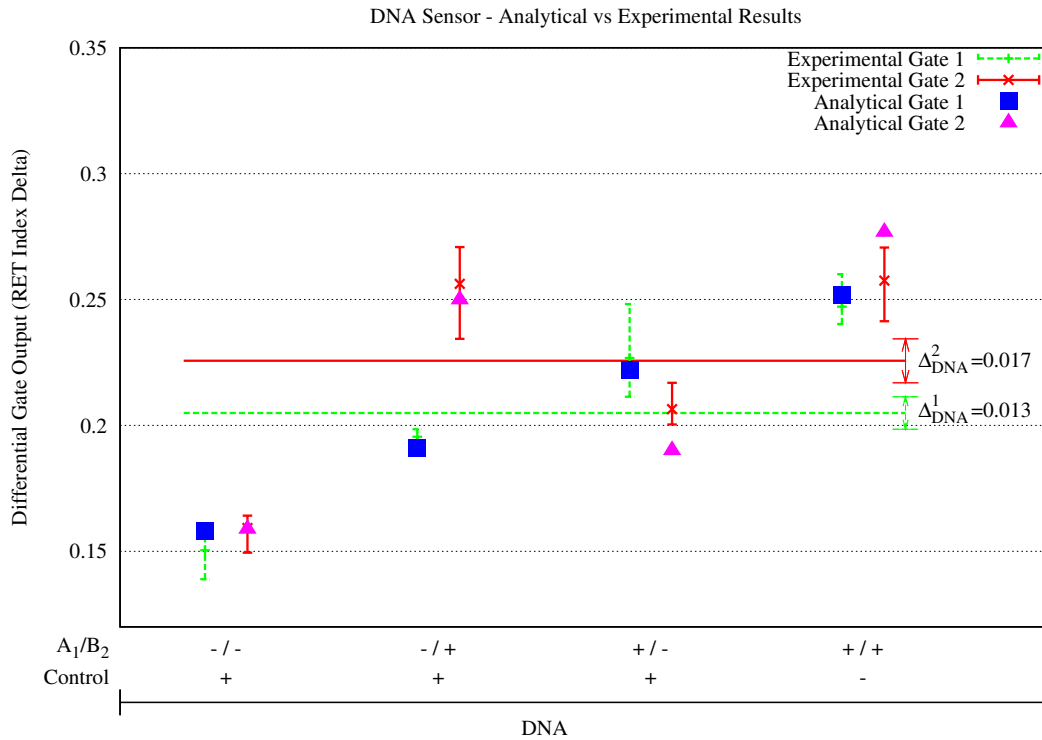
However, this data must be compared against a calibrated sample and thus limits the usefulness of the approach for “blind” concentration measurements without further study.

4.4 Underlying mechanism for sensing

To understand more precisely how each AND-gate output is disrupted by an analyte we use non-linear least squares fitting of the observed change in I_{RET} to determine pre- and post-melt RET parameters such as κ^2 and r . To do this, we model our system as a mixed population of gates and free chromophores. A yield factor, f_y , is the ratio of grid-bound to free chromophores and represents the extent to which we have ideally formed circuits. This leads to an observable fluorescence output rate (F_x') per gate of $F_x' = F_x \cdot f_y + E_x \cdot (1 - f_y)$. To account for analyte-independent disruption of gates during the melting process we use a gate recovery factor, f_r , which quantifies the fraction of undamaged gates which bind analyte, in the fluorescence rate equation $F' = F_x \cdot f_y \cdot f_r + E_x \cdot (1 - f_y \cdot f_r)$. Figure 6 shows the fit between the model and the data for pre- and post-melting of a sensor with two active gates targeting two DNA analytes (SI Section 5). Since we must also estimate functional yield in addition to structural yield we do not use the QSA or other AFM-derived yield metrics because we have found that commensurate binding between planar DNA nanostructures and flat surfaces artificially enriches the apparent yield. To obtain the best fit possible between the model and data we first use data from two idle gates to characterize the fabrication yield of our system. The best fit for the idle gate data estimates that approximately 35% of possible pairs of logic gates have formed correctly. This underscores the discrepancy induced by AFM and accepted methods to estimate yield [72] which conclude that our gate yield, based on structural yield, should be closer to 47%.

To determine parameters like the pre- and post-melt κ^2 and r for the active gate we use the estimated circuit yield and solve for the best fit to F' allowing the gate recovery factor (f_r),

separations ($r_{x,y}$), and orientations ($\kappa_{x,y}^2$) to vary between analyte types (e.g., DNA, RNA, or protein) but each remain fixed across similar runs (e.g., $N > 3$). The fitting results, shown in Figure 4-6, support the hypothesis that analyte binding disrupts gate outputs by modulating κ^2 rather than r since separation plays such a limited role at short distances. Specific details for each fit can be found in the Appendix 1 and Fig. 6 presents the best fit when donor-acceptor pair distances and orientation can vary pre- and post- melt (the summed least squares residual (LSR) is within 0.4% of the maximum data value). We note that to achieve the experimental ΔI_{RET} of ~ 0.25 the inferred separations must be high ($> 5\text{nm}$) and orientation factors similar to rigidly bound chromophores (< 0.01). Since the chromophores we use are hydrophobic and susceptible to binding in the major groove of duplex DNA [27, 74, 87], this suggests that a change in donor-acceptor orientation (or a combination of distance and orientation) is the most likely cause of output modulation since separation alone is unable to match the observed ΔI_{RET} .



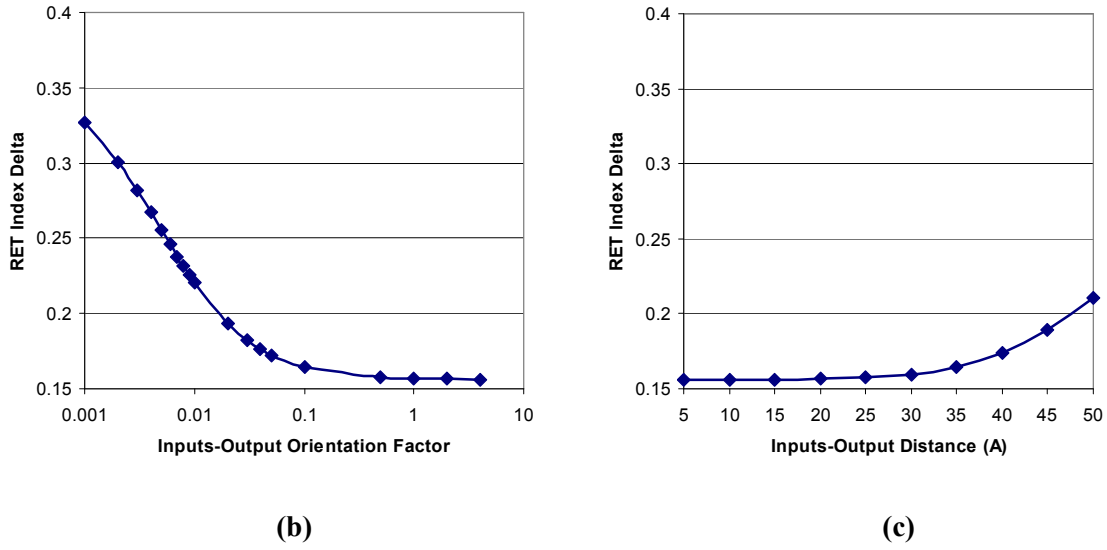


Figure 4-6: Fitting results. We calculate the best fit to F' allowing the gate separations ($r_{x,y}$) and orientations ($\kappa_{x,y}^2$) to vary. The analytical result for DNA sensing is shown against the same experimental results in (a). In (b) we restrict the modulation to input-output orientations only and calculate the $A_1^- B_2^+ \text{Ctrl}^+$ configuration assuming varying orientation factors in the bound-analyte gate (x-axis). The same scenario is shown in (c) allowing only input-output separations to vary.

4.5 Scaling to larger circuits

The methods described here demonstrate the feasibility of sensing biomolecules with RET logic. The method takes advantage of DNA self-assembly to build nanoscale grids with integrated RET circuits designed to operate like digital multiplexers. In this proof-of-concept we show that the response of two logic gates, that differ by only one input bit, can be resolved with sufficient margin to be useful in a sensor system. However, an important aspect of this work is to demonstrate a viable pathway toward building larger RET circuits suitable for high throughput sensing of many analytes, simultaneously. To do this, we use Boolean logic to design a multiplexer by choosing logic terms that each enable a distinct output and thus a distinct sensor. Upon any unique excitation, or address, we observe the output from one and only one kind of sensor. In this way, it is possible to combine many such sensors into a single monolith, smaller than the diffraction limit, as long as each address uniquely identifies a single kind of sensor. The

maximum number of unique addresses is determined by the radix and number of the address symbols, or bits in binary logic given by 2^N , where N is the number of address symbols. By choosing powers of two as weights for each address bit position (i.e., Boolean weights) any unique combination of bits creates a unique value given by $\sum_{i=0}^{N-1} 2^i \cdot B_i$, where B_i is the bit at position i in the address. However, to detect any given address a circuit must determine equivalence between this calculated value and a constant value (i.e., the address), which requires both the positive and complemented form of each address bit.

Since we currently do not have the digital equivalent of an inverter in RET logic, and thus cannot use complemented terms in a logic circuit, we use non-Boolean weights to create unique addresses. By choosing a logprime weight for each symbol in the address the superposition of responses will be unique, as given by $\sum_{i=0}^{N-1} \log(W_i) \cdot B_i$, where W_i is prime. The proof of this is straightforward by analogy to the factorization of integers into primes and the multiplicative relationship between logarithms and sums. Thus, the binary weighted sum of the logarithms of N distinct prime numbers is unique. For example, if each of three binary symbols in an address is given $\log(3)$, $\log(5)$, and $\log(7)$ weight by position, the linear combination of all three yields a unique value over the entire space of binary inputs. The input weight for each chromophore is controlled by placing it at a separation and orientation on the grid that will attenuate RET to the shared output chromophore. Thus, a gate can be created where each input chromophore contributes an exact amount, as determined by the normalized weights, of RET to the output when excited.

The logprime technique trades signal-to-noise for increased address space by requiring a proportional degree of significance in any measured response. Thus, single-photon counting

techniques with the ability to detect single chromophores, dilute gates such that the analyte is in excess, and a library of only six distinct chromophores (i.e., five inputs and one output) enables sensing of over 24 analytes on a single 4x4 DNA grid by employing logprime weights. After accounting for yield (35%) and a diffraction limited spot size (e.g., with 600nm fluorescent output) the overall density of 24 sensors per spot leads to $\sim 10^{14}$ unique analytes per m^2 (e.g., using a routine spot printing technique) which exceeds the density of next-generation sensor arrays (e.g., gene chips with 500nm diameter spots per single probe) by two orders of magnitude. More importantly, the technique we report here has the potential of integrating more complex RET logic onto nanoscale DNA grids which can be seamlessly integrated into biological assays.

4.6 Related Work

Selective, label-free detection of proteins[110], DNA[35], viruses[60], small molecules[97] and antibodies[85] has been demonstrated using functionalized semiconducting nanowires and nanowire field effect transistors. The electrical readout mechanism used in these methods requires routing metal contacts to and from each sensor and thus is relatively costly. The sensors that we present are integrated on water-soluble DNA tiles and do not require a macroscale substrate or any kind of tether for readout. These properties can expand the range of microenvironments that are accessible for sensing.

A closely related class of optical sensors is based on fluorescence resonance energy transfer (FRET), which transduce a molecular recognition event, such as the binding of a target analyte, into a fluorescence signal through a change in the rate of resonance energy transfer (RET). A wide variety of FRET sensors are available, a large fraction of which modulate RET upon binding by altering donor-acceptor pair orientation[104] or distance[19, 25, 57]. Since FRET sensors use the same inter-chromophore energy transfer as RET-logic they can interface directly with RET-logic circuits. In this work we integrate multiple RET devices on the same

substrate and provide the ability to retrieve their sensor status individually. This approach is conceptually similar to the gene or protein arrays used in high-throughput assays[28], but at a molecular scale.

DNA tiles based on single-strand folding[72] have been recently used for RNA sensing[45]. In this design the target RNA strands hybridize with single-strand probes which increase their stiffness and generate a topographical feature that can be resolved by atomic force microscopy (AFM). Our approach differs from this in that it does not require a scanning probe image of the sample. Instead, sensor values are detected by basic ensemble optical measurements with a dual excitation beam spectrofluorometer.

4.7 Conclusion

In this chapter we demonstrated a method that integrates RET molecular logic circuits with sensing and can selectively identify label-free biomolecules in solution by optical multiplexing with binary encoded inputs. The resulting circuits can detect femtomole quantities of proteins, DNA oligomers, and small fragments of RNA (5-nt) in solution. Information I/O to the nanoscale RET circuits is achieved using global optical signals and inexpensive spectrometer read-out equipment. This method, which creates up to twenty-four 8-nm³ logic gates on a 60nm x 60nm DNA grid, is a scalable step toward nanoscale logic capable of interfacing computers with biological processes.

The ability to integrate computation and sensing in a single, biologically compatible molecular device enables a new nanoscale computational domain. In the next chapter we explore the application requirements and the design space of nanoscale sensor processors for this novel domain.

5 Nanoscale Sensor Processors

Understanding molecular scale phenomena is a critical component of many scientific disciplines. The ability to retrieve nanoscale information from within macroscale systems is particularly useful in biological fields where the diversity of molecular components and interaction dynamics within a cell make it difficult to monitor and quantify the underlying processes. Current methods rely on custom designed molecules—called molecular probes—that alter their observable properties to acquire real-time information about nanoscale phenomena.

Molecular probes are important members in the biological scientist's tool box, however they generally function as standalone sensors. Furthermore, their use requires costly equipment, highly specialized training and often the experiments span several days [92]. These limitations prevent the application of molecular probes in monitoring complex biological processes with low cost. For example, at home early disease detection could be achieved with a low-cost device capable of monitoring important markers of bioactivity and cellular health, such as concentrations of specific proteins or small messenger RNA (mRNA) molecules [23]. The challenge is to develop techniques that provide low cost, efficient monitoring of complex molecular scale biological processes.

Computing is often used to monitor complex processes or automate tasks that require expert training. However, biological scale computing represents a new domain for computing with very different constraints from traditional computing systems. For example, this new computing domain requires the ability to diffuse through a volume of small molecules, computing in and sampling the same local environment as a molecular probe (e.g., the homogenized contents of a cell). This size requirement excludes current CMOS solutions since large (several microns) silicon chips do not diffuse freely. Although a CMOS processing core connected to bio-sensors

[95] could read and process chemical information, it would not be able to automate molecular probe applications because of its large aggregate size.

This chapter presents the concept of a nanoscale sensor processor (nSP), which addresses the above challenges through the integration of molecular probe sensors and molecular scale digital logic. An nSP is a nanoscale sized system that can sense, process, store and communicate molecular information. A generic nSP has several components: sensor array for environment monitoring, simple processor core, small memory for state and programs and a communication device for information transfer to the macroscale. Each element of the sensing array is a molecular probe designed to detect the presence of a specific target molecule—called an analyte—through chemical bonding.

The size restriction for molecular probe applications requires a computational substrate that can cost-effectively support meaningfully complex circuits with nanometer feature sizes and provide sensing ability. There are many examples of nanotechnology (e.g., carbon nanotubes[5, 109], silicon nanorods[43], DNA/enzymatic reactions[17]) that provide both a logic system and sensing capability. In this chapter we focus on one specific technology— Resonance Energy Transfer (RET) logic—as the basis for our nSP design. As detailed in the previous chapters, RET logic enables molecular scale digital logic circuits (Chapter 3) and integrated sensing (Chapter 4) using self-assembly fabrication techniques (Chapter 2). However, we note that much of our analysis and architectural design is independent of the specific technology.

The architectural design space of an nSP is strongly influenced by the limited size and by the target application characteristics. Section 3 presents several applications that vary in complexity and discusses the characteristics that influence nSP architecture design. These characteristics include: 1) long time scales, 2) accumulating values, 3) waiting for an event, and 4) processing groups of individual sensor values as an aggregate.

Section 4 presents our nSP architecture, a simple accumulator data path with variable length instructions (either 4 bits or 12 bits). We present two different designs that implement the same base ISA, but differ in operand width and the amount of memory provided. The Standard design provides 256 4-bit memory locations while the Tiny implementation provides only 16 4-bit memory locations. We also introduce the concept of instruction-fused sensing that exploits unified compute/sensing technologies to enable direct environmental modification of instruction bits, and thus reduce overall code size.

We evaluate our nSP designs in Section 5 using simple models and a custom simulator. Our results show that the Standard design occupies approximately $2.5\mu\text{m} \times 2.5\mu\text{m}$ while the Tiny implementation requires approximately $800\text{nm} \times 800\text{nm}$, comparable to the largest known virus. We demonstrate that our target applications can fit within the restricted memory space of the Standard nSP, and that four of our five applications can be implemented in the 8 Bytes of memory on a Tiny nSP. We also explore the design tradeoffs in our nSP instruction set and use simulation to demonstrate the execution of applications in a time varying chemical environment.

Related work is discussed in Section 6 and we conclude in Section 7.

5.1 Enabling Technology

The integration of computation and sensing in a nanoscale package imposes challenging requirements on the underlying technology and manufacturing of nSPs. To date there is no clear winner in the field of nanotechnology for computing or sensing. Carbon nanotube and ring-gated nanorod FETs are hopeful candidates, but obtaining control over the precise device length and precise placement for arbitrary patterns remain open challenges.

We propose using a new nanoscale technology for nSPs based on single-molecule optical devices called chromophores. In isolation, a given chromophore absorbs photons of a specific wavelength and emits photons at a different, lower energy, wavelength. However, when

appropriate chromophores are placed a few nanometers apart the energy of an absorbed photon can be transferred to a neighboring chromophore through a process called Resonance Energy Transfer (RET). This process is frequently used for molecular scale sensing (e.g., molecular beacons or molecular rulers) [47]. RET also provides a theoretical foundation, which we explored in Chapter 3, for the creation of pass gates (both inverting and non-inverting) using four chromophores per gate. These gates form a complete Boolean logic set we call RET-logic.

A key requirement for RET-logic is to place unique chromophores within a few nanometers of each other. Unfortunately, creating such devices using conventional top-down fabrication techniques is costly and increasingly complex. Creating sophisticated circuits by placing individual atoms requires more energy and time than exploiting chemical self-assembly techniques. Furthermore, self-assembly enables fabrication through composition and hierarchies. Different types of molecules can be fabricated independently using the most cost-effective method for each type of molecule. Larger motifs can then be created through the composition of heterogeneous molecules.

RET-logic uses DNA-based self-assembly, detailed in Chapter 2, as the fabrication method to place chromophores within specified distances. The specific DNA nanostructures we use, are grids where we can place two pass gates and one wire crossover per grid vertex. The grids can be hierarchically assembled to create large arrays of pass gates—the nanoscale equivalent to a sea-of-gates.

The next section describes some of the characteristics and tradeoffs of RET-logic computational elements integrated on self-assembled DNA substrates, followed by an overview of current experimental progress towards an nSP prototype.

5.1.1 RET-logic Circuits

The design of RET-logic circuits on DNA grids is explored in detail in Chapter 3. We provide here a brief overview of their characteristics. The layouts in Figure 5-1 show implementations of common RET-logic circuit components (decoder, memory, and 1-bit full adder cells) on a 20nm-pitch DNA substrate. We use inverting and non-inverting pass gates; wires are annotated with the frequency of their specific optical signal ($a > b > c > d > g$).

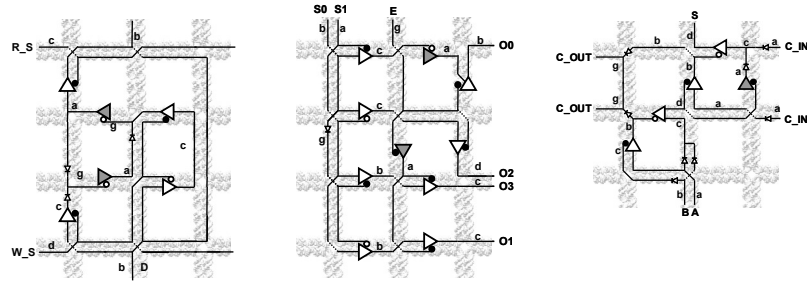


Figure 5-1: RET logic circuit layouts on DNA substrate: SRAM memory cell 60nm x 40nm (left), 2 to 4 decoder 60nm x 40nm (center), 1-bit full adder 40nm x 40nm (right). Grid spacing is 20nm.

Each RET gate has an operational energy cost: the output signal is at a longer wavelength than the input. Signal restoration from long wavelengths (low energy) to short wavelengths (high energy) requires additional energy. The pass gates can provide this functionality if the input to the pass gate is generated from an external far-field optical source, called an optical pump (conceptually analogous to Vdd), and the gate is controlled by the signal to either invert or pass. These restoring gates are shown in a darker shade in Figure 5-1. Since “Vdd” is a far field signal it does not need to be routed. This lack of routing overhead applies to all global inputs (like the clock signal) and is a significant advantage of RET-logic in area-constrained designs. From first-principles analysis we expect the switching time for a FO1 pass-gate to be approximately 2ns with a thermally dissipated power of less than 0.4nW. Communication with external receivers can be implemented using open-ended wires with dedicated emission wavelengths.

The memory cell in Figure 5-1 is a volatile SRAM design. Non-volatile memory could similarly be implemented using a special class of chromophores that have two switchable, stable molecular states [41]. The drawback of using non-volatile photo-switches is that the write time is much slower than that of an SRAM cell (ms vs. ns). We leave exploring non-volatile memory in nSPs as future work.

5.1.2 RET-based Sensing

RET sensors are devices that transduce a molecular recognition event, such as the binding of a target analyte, into a modulation of their optical RET properties. A wide range of biological RET sensors are currently available [47]. The fundamental property that these sensors employ is the dependence of RET on chromophore separation. RET only occurs when chromophores are sufficiently close (a few nm), and decreases as the distance increases. For sufficiently separated chromophores, RET will not occur. Sensors can be designed to enhance RET or prevent RET when a molecular recognition event occurs. Since RET sensors use the same inter-chromophore energy transfer as RET-logic they can interface directly with RET-logic circuits.

5.1.3 Preliminary Experimental Results

In the previous chapters we presented initial results toward fabricating an nSP using RET-logic. We demonstrated four main points: 1) that with the DNA grid we can place chromophores sufficiently close to achieve RET interaction, 2) demonstrated simple wired-OR RET logic, 3) shown that the DNA grid can bind analytes (in this case proteins) using antibodies placed at precise locations on the grid surface, and 4) that RET-logic gates can sense the binding of such analytes.

In Chapter 2 we used the cruciform motif from Figure 5-2a to build DNA grids. Figure 5-2 shows AFM images of (b) a 60x60nm hierarchically assembled grid, (c) the same grid with a protein pattern and (d) a 140x140nm grid each assembled in our laboratory.

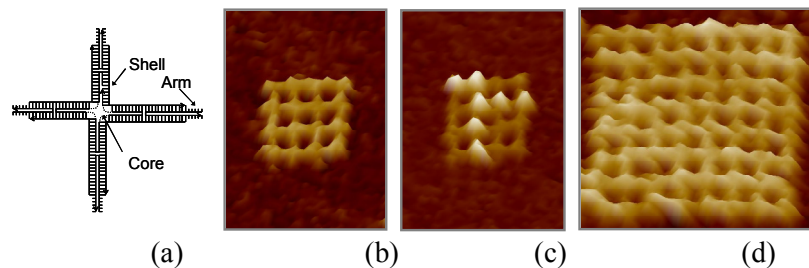


Figure 5-2: (a) Schematic of a Cruciform Motif and Atomic Force Microscopy Images of (b) 60x60nm DNA Grid, (c) Grid with Bound Proteins and (d) 140x140nm Grid.

Using chemistry similar to that used to attach proteins it is possible to attach chromophores to specific sites on the DNA grid. The available sites on each grid occur at the intersection between motifs and at the center of the cruciform motif. The spacing between sites at the motif intersections is $\sim 1.3\text{nm}$ and $\sim 20\text{nm}$ between motif centers. In Chapter 3 we experimentally demonstrated the capability to place three chromophores sufficiently close to transfer excited-state energy from two distinct inputs to the same output, characteristic of an OR-gate.

In Chapter 4 we showed how the output of RET-logic gates can be modulated by the binding of target analytes and demonstrated an application for selective sensing of biomolecules like proteins and small fragments of DNA and RNA.

The technology we presented forms the foundation for biologically compatible computing and sensing, and we believe it will be possible in the future to fabricate nSPs. Understanding the technology is only part of architecting a system. We must also gain an understanding of the application requirements. The next section discusses several potential applications.

5.2 nSP Applications

One of the critical design requirements for an nSP is that it be small enough to diffuse through small volumes. A typical red blood cell width is approximately $6\text{-}8\mu\text{m}$ and we envision

applications that require operation within a cell. The RET-logic nanotechnology described above only provides the potential to create appropriately sized nSPs. To meet the severe size constraints, even RET-logic systems must be carefully architected. To achieve this we need to understand the computational requirements of the biological applications.

To illustrate the diverse application space we selected several target applications that we believe are representative of an nSP's potential. These applications are: 1) early disease detection, 2) custom multi-analyte molecular probes, 3) molecular kinetics analysis, 4) monitoring complex biological scale processes, and 5) imaging below the diffraction limit. We discuss each application in more detail below.

Our goal is to understand the applications' requirements such that we can architect an appropriate nSP system. To achieve this we consider two aspects of each application: 1) the algorithm to perform and 2) timing constraints. The algorithm specifies, at a high level, the computation to perform and is used to determine which primitive operations to support. The timing constraint sets bounds, both upper and lower, on the latency of a primitive operation or an entire computation.

For many biological applications the expected timescales are in the range of seconds to minutes [32]. These times are generally determined by either chemical reaction rates or molecular interaction rates. For example, sensors can be either reversible or irreversible. For irreversible sensors, once the analyte binds to the sensor it is bound forever. In contrast, for reversible sensors the analyte will eventually detach from the sensor. Timescales for irreversible sensors are determined by the binding rate of the analyte. A reversible sensor's time dependent behavior can be characterized by two parameters: 1) a period, and 2) a dwell time. The period is defined as the time between two distinct binding events, and the dwell time is the time an analyte stays bound to

the sensor after the binding event. The period and dwell time of a sensor often represent average values for a probabilistic distribution of times.

We present pseudocode for each of the applications with the goal of demonstrating that an nSP can provide capabilities beyond a single sensor. This pseudocode assumes the ability to read a specified sensor (i.e., `read_sensor(name)`) that targets a particular analyte and returns a Boolean value, True when the analyte is bound to the sensor, False otherwise. We also assume the ability to output an integer value.

Early disease detection. Integrating multiple pathogen sensors on an nSP can address the early detection problem through in vivo or in vitro biological monitoring over extended time windows. A program can count the number and type of binding (or detection) events over this window. At periodic intervals the nSP is queried for their event counts and the information is aggregated and compared against normal thresholds. The algorithm shown in Table 5-1A is an algorithm for counting pathogen binding events. An anti-hemagglutinin based sensor that detects the influenza A typical virus has a dwell time of 1-1.5 seconds and an expected period of minutes [60] at dilute concentration.

Custom Multi-Analyte Molecular Probes. Integrating several molecular probes on an nSP presents the possibility of detecting complex sequences and combinations of environment conditions. Table 5-1B shows an example program that outputs True when a specific combination and order of analytes is detected. The timescale is defined by the rates of monitored reactions and varies from minutes to ns depending on their biological or non-biological nature.

Kinetic Analysis. The quantitative evaluation of specific, reversible molecule binding is universally important in biology. Proteins interact with nucleic acids in gene expression, enzymes with substrates and inhibitors in metabolic processes, antigens with antibodies in the immune system. The binding interaction of two molecules at equilibrium is characterized by binding and

dissociation constants. Classical methods for measuring binding constants with biosensors work at the macroscale and can involve many time consuming repetitive steps [69]. nSPs can derive sensor-analyte binding kinetics information in localized nanoscale environments in real-time by sweeping the nSP clock cycle time. The clock frequency is adjusted until the period and the dwell time of the analyte are captured in a sensor integration window. The algorithm integrates the instant sensor value for a fixed number of iterations and outputs the result (Table 5-1D). The range of available nSP clock frequencies determines the range of binding rate constants that can be analyzed. Classic macroscale methods, e.g., quantitative affinity chromatography, can measure binding constants ranging from 10^2 – 10^9 mol/L.

A) Pathogen Counting	B) Multi-Analyte Probe
<pre>while (true) { sample = read_sensor(P) if (sample != last_sample) { count += sample last_sample = sample } if (send_data = true) { output(count) count=0}}</pre>	<pre>wait until (read_sensor(A) = true) wait until (read_sensor(B) = true and read_sensor(C) = true) wait until (read_sensor(D) = true and read_sensor(A) = false) output(true)</pre>
C) Finite Impulse Filter	D) Kinetic Analysis
<pre>while (true) { sample = 0 for k = 1 to M { sample += read_sensor() } d[last] = sample y = 0 for k = 1 to N { y += c[k]*d[(last+k)%N]} last = (last+1)%N output(y) }</pre>	<pre>while (true) { sample = 0 for k = 1 to M { sample += read_sensor() } output (sample) }</pre>
E) Imaging	
<pre>while (true) { if (send_data = true) for i = 1 to N { output(sensor_read(i))}}</pre>	

Table 5-1: Pseudocode for nSP target applications

Monitoring Complex Processes. The ability of nSP chips to store and process nanoscale data across potentially large reaction time windows could be used, for example, to compute the

average binding rate of a set of proteins or mRNA molecules. The challenge is to perform this averaging at the nanoscale over a large set of possible proteins (e.g., approximately 4×10^5 unique proteins can be found in any individual human cell). A distributed set of nSPs, each designed to detect a subset of the proteins, could employ diffusion to sample and average protein concentrations over a large observation window to track protein expression.

In this type of complex process we expect nSPs to process long series of sensor data using accumulation, weighted averages, histograms or filters. Table 5-1C shows the algorithm for a Finite Impulse Response (FIR) filter. In the case of mRNA and proteins involved in gene activity the kinetics are on a timescale of seconds to minutes [32], although some processes, e.g., conformational changes of signaling proteins, are at the ms scale [96].

Functional Imaging below the Diffraction Limit. The sensor array of an nSP also provides implicit spatial information because of the precise, pre-determined location of each sensor. An interesting potential application of this fact is the imaging of features smaller than the diffraction limit, the fundamental resolution limit of optical microscopes. Multiple nSPs tiled on the surface of interest can serially transmit the 2D “image” of their sensing arrays and optical microscopy equipment can then combine the absolute nSP orientation data in the optical image (a feature that is above the diffraction limit) with the received nSP-relative information to create a composite image of all sensors across all nSPs. The same approach could potentially be used to implement high density nanoscale gene chips. The algorithm is shown in Table 5-1E, each nSP simply outputs the current values for its entire sensor array.

Other applications may be developed if nSPs become available, such as experiment-on-a-chip or nanoscale sensor networks. We leave further exploration of additional applications as future work, and instead focus on designing a single nSP based on our five representative applications.

Through inspection of the above applications we can extract several important characteristics that influence architectural designs, these include: 1) long time scales, 2) accumulating values, 3) waiting for an event, and 4) processing groups of individual sensor values as an aggregate. The following section discusses how these characteristics guide our architectural design.

5.3 *An nSP Architecture*

In this section we present our design for an nSP. We arrive at this design by combining the various application characteristics with the overarching requirement that an nSP must be small enough to diffuse through small volumes. We begin this section by discussing how these requirements qualitatively influence nSP architecture. This is followed by a detailed presentation of our nSP architecture. Our goal is to demonstrate that an nSP can be designed to meet the requirements of this new computing domain. We leave optimizing the architecture as future work.

5.3.1 Qualitative Architectural Implications

The nSP architecture is influenced by each of the application characteristics either individually or when combined with other characteristics. We discuss each of the characteristics and its qualitative influence on architecture. First, the long time scales (seconds to minutes) of biological applications implies that we do not need a high performance processor core (e.g., no superscalar, out-of-order, deep pipeline). Instead the architect can trade area for time using a very simple processor core with complex operations synthesized in software (e.g., multiply and divide).

The second characteristic is that many of the applications accumulate values over time either by counting events, averaging, or integrating values that are monotonically increasing. This has several implications for the architecture. First, the computations can generally be performed using fixed point arithmetic, avoiding the need for floating point hardware. Second, the

accumulated value may require a larger range than the input value, thus leading to datapath components wider than the memory/sensor width. Third, accumulation is common enough that architectural support is justified to help reduce code size.

The next application characteristic, waiting for an event, is similar to accumulating a value in that on conventional architectures it is implemented by reading a sensor value within a loop and either incrementing a counter (accumulating) or checking if the sensor value has changed (wait for event). Like accumulation, waiting for an event is sufficiently common across the applications that the architecture should provide support to reduce code size.

Finally, processing individual sensors as a group implies that it may not be necessary for the architecture to support access to individual sensor values. Instead it may be beneficial to provide support for processing multiple sensor values as a single entity.

5.3.2 nSP Overview

We investigated 8-bit architectures for ultra-small controllers, e.g., the ST Microelectronics ST6 [86] and the Freescale RSO8 [29], designed to be efficient and cost effective with small memory sizes. These architectures, although simple compared to mainstream designs, proved too complex for the extreme area constraints of nSPs. We instead elected to create an architecture streamlined for the expected applications and hardware limitations of nSPs.

Our nSP architecture is a simple accumulator-based processor with a small amount of addressable memory/sensors. Using a single-accumulator reduces the processor core complexity and enables short 4-bit opcodes to support the common recurring operations in nSP applications. Our standard nSP design can address up to 256 4-bit words in a unified instruction/data/sensor memory space. Instructions are variable-length (4bit or 12bit) to decrease the memory footprint of application code. A special variant of our architecture, called Tiny, is designed for the smallest nSPs with a total memory space of only 8 bytes (16x4-bit).

5.3.3 Integrated Sensing

The sensor-centric nature of nSP applications means that the interface between processing and sensing plays an important role in the system design. There are a variety of ways that an nSP can support sensing. For instance, sensors could be memory mapped. In this scenario, predetermined memory addresses are set aside for access to sensed values via load instructions. The method we explore in this paper exploits the biological compatibility of the entire system when using technologies like RET-logic. Since RET is the method used for sensing and for computing, we can directly integrate the sensing mechanisms into the system design.

Although there may be many ways to exploit an integrated design methodology, in this paper we examine methods for sensing to directly modify memory locations. Specifically, certain SRAM cells can be augmented with appropriate sensing mechanisms that force the memory location to the value “1” (or “0” as needed). A technological requirement is that the active area of the sensor must fit within the confines of an SRAM cell. These environmentally modified memory locations could be designed to provide a set of memory-mapped sensors. However, this does not exploit the full potential of a unified sensing and logic technology such as RET. Instead we can interleave sensor-augmented SRAM cells with standard SRAM cells, including those used for instruction opcode bits. For example, a JMP opcode could be modified into a NOP opcode by a sensor binding event. Similarly, instruction operands could be modified by the sensing mechanism to change an arithmetic operand or a branch target. We call this technique instruction-fused sensing (IFS).

IFS provides a unique opportunity for hardware/software co-design to improve code density. With only 8 to 128 bytes of memory available, judicious use of instructions is paramount to providing sufficient computational abilities. The simple task of querying a sensor to determine if a specific protein is present can require several bytes of instruction memory to load a value and

compare it for branching. Instead, a single branch instruction could be used that changes to a NOP (and escape) when the protein binds.

Using IFS can dramatically improve code density where it is applicable. There is, however, a trade-off: the instruction becomes statically bound to the sensor. This can prevent code reuse via procedures or looping. We note that code reuse is valuable when the increase in code-size due to procedure overhead is compensated by the removal of significant inline code. In the limited memory and program space of an nSP this break-even can be difficult to reach. We evaluate this trade-off in more detail in Section 5.

5.3.4 The nSP ISA

Table 5-2 shows our nSP Instruction Set Architecture (ISA) which supports several common memory, arithmetic, and control transfer instructions. Each of the instructions in the ISA is included because it directly supports common operations in one or more applications. Note that the ISA lacks several instructions one often considers standard, e.g., subtract, multiply, and divide. These operations can all be synthesized with the provided instructions if needed. For brevity, when details are necessary we discuss only the Standard nSP ISA.

Several of our nSP instructions are designed to reduce application code size. The INCI instruction, which increments an 8-bit value using implicit addressing (PC relative), is useful for accumulating single-bit sensor values and for control loops, which are recurring operations in the nSP applications. Several instructions also exploit IFS to reduce code size. In particular, JMP, BNZ, INC and INCI all have the option of using IFS. When declared sensitive to an analyte (A), these instructions turn into NOPs when that analyte binds to the appropriate memory location. To facilitate this mechanism we encode a single-bit difference between the opcode of these instructions and the NOP opcode. When a sensor is fused to this bit location the opcode value depends on the value of the sensor, as determined by the presence or absence of an analyte. This

requires careful hardware/software co-design to ensure proper alignment of code and sensors in the memory space.

Instruction	Op.	Standard RTL	Tiny RTL	Description
LD addr	0000	$ACC[0..7] = M_8[addr]; PC += 3$	$ACC[0..3] = M_4[addr]; PC += 2$	Load from memory
ST addr	0001	$M_8[addr] = ACC[0..7]; PC += 3$	$M_8[addr] = ACC[0..4]; PC += 2$	Store to memory
ADD addr	0010	$ACC[0..15] += M_8[addr]; PC += 3$	$ACC[0..7] += M_4[addr]; PC += 2$	Add unsigned from memory
ADDI imm	1100	$ACC[0..15] += M_8[PC+1]; PC += 3$	$ACC[0..7] += M_4[PC+1]; PC += 2$	Add unsigned immediate value
SHL	0100	$ACC[0..15] = ACC[1..15] 0; PC += 1$	$ACC[0..7] = ACC[1..7] 0; PC += 1$	Shift 1 position left
SHR	0101	$ACC[0..15] = 0 ACC[0..14]; PC += 1$	$ACC[0..7] = 0 ACC[0..6]; PC += 1$	Shift 1 position right
NOT	0110	$ACC[0..7] = ! ACC[0..7]; PC += 1$	$ACC[0..4] = ! ACC[0..4]; PC += 1$	Bitwise NOT
AND imm	1010	$ACC[0..7] += M_8[PC+1]; PC += 3$	$ACC[0..4] += M_4[PC+1]; PC += 2$	Bitwise AND
CLR	0011	$ACC[0..15] = 0; PC += 1$	$ACC[0..7] = 0; PC += 1$	Clear ACC
JMP addr (A)	1110	$PC = M_8[PC+1]$	$PC = M_4[PC+1]$	Jump to address
BNZ addr (A)	1101	If $ACC[0..7] \neq 0$ $PC = M_8[PC+1]$ Else $PC += 3$	If $ACC[0..4] \neq 0$ $PC = M_4[PC+1]$ Else $PC += 2$	Jump to addr if ! ACC
INC (A)	1011	$ACC[0..15] += 1; PC += 1$	$ACC[0..7] += 1; PC += 1$	Increment ACC
INCI imm (A)	0111	$ACC[0..7] = M_8[PC+1]; ACC[0..15] += 1;$ $M_8[PC+1] = ACC; PC += 3$	$ACC[0..3] = M_4[PC+1];$ $ACC[0..7] += 1;$ $M_4[PC+1] = ACC; PC += 2$	Increment memory value, store in memory and ACC
NOP	1111	$PC += 3$	$PC += 2$	No operation
OUT addr	1000	$COMM = M_8[PC]; PC += 3$	$COMM = M_4[PC]; PC += 2$	Output ACC
OUTCLR addr	1001	$COMM = M_8[PC]; PC += 3$	$COMM = M_4[PC]; PC += 2$	Output & clear memory

Table 5-2: Our nSP ISA: $M_8 = 8$ bits starting at specified location, $M_4 = 4$ bits. Standard has 16-bit Accumulator, 8-bit PC, and 255 4-bit memory locations. Tiny has 8-bit Accumulator, 4-bit PC, and 16 4-bit memory locations.

We denote the analyte-dependence of an instruction by placing the analyte name in parenthesis after the instruction. Depending on the encoding of the binding event, the instruction can be NOP-ed by either the presence or the absence of the analyte. We use C-style (!) to indicate the instruction is executed when the analyte is not sensed and the analyte identifier alone when the instruction is executed only in the presence of the analyte. For example, INC (!A) means the accumulator is incremented only if the analyte A is not present, else it is a NOP and has no effect.

Instruction operands, either immediate values or addresses, are 8-bit length, the same as the data granularity of loads and stores. This allows for easy address manipulation, but most importantly it increases the numerical range for operations performed on sensor data. One of the common patterns we see in the nSP target applications is that individual sensor data is accumulated in time before being further processed, with the option of longer accumulation times being more desirable. Native support for 8-bit arithmetic increases the accumulation time interval from 16 to 256 cycles while avoiding the severe code size penalty that would result from emulation with 4-bit instructions. The accumulator is 16-bit for extended dynamic range in applications like FIR filters where double word samples are averaged or multiplied through shift-and-add. The high 8 bits of the accumulator can be accessed through explicit shifts into the low 8 bits.

Defining only 8-bit wide memory operations could prove restrictive given the single-bit granularity of sensors. Indeed, accessing an individual sensor value through a wide load can require additional bit masking and shifting. We argue, however, that in cases where single bit sensor values are necessary it is generally more efficient to use the compact instruction-fused sensing mechanism. An analysis of the target application algorithms shows three distinct cases in which sensors are individually queried for their value: 1) branch outcome depends on an individual sensor value, 2) arithmetic result depends on an individual sensor value, 3) output of

sensor values. The first two can be addressed with IFS and the latter can bundle values for output and separate values at a remote receiver.

5.3.5 Discussion

The above nSP architecture is designed to meet the requirements of the new computing domain of biological scale computing. The architecture is generic and can be implemented in several different nanotechnologies that provide both sensing and digital logic. Size is a crucial constraint for an nSP architecture, as any device must be capable of diffusing through small volumes. The architecture presented in this section provides a set of novel mechanisms (e.g., instruction-fused sensing) that enable compact implementations of important biological applications. The following section analyzes the ability of the proposed architecture to satisfy the requirements of the target applications.

5.4 Evaluation

In this section we evaluate our nSP architectures. We begin with an analysis of the nSP size, followed by a discussion of the applications implemented using the nSP ISA and the memory resources required for execution. We then explore the impact of instruction-fused sensing on program size and conclude with simulation of applications monitoring time varying environmental conditions.

5.4.1 Node Size

As previously noted, the size of an nSP is an important factor for biological applications. Here we use the RET-logic layouts and characteristics described in Section 2.1 to estimate the area of nSP implementations. Our preliminary layout indicates that the Standard nSP implementation with 128 bytes of memory requires $2.5 \times 2.5\mu\text{m}$ and a Tiny nSP implementation

with 8 bytes of memory requires 800x800nm. With a surface area comparable to the largest known virus [89], the Tiny nSP could diffuse in the same environments as the virus (e.g., a cell).

5.4.2 Program Size

We implemented the target applications for both the Standard and Tiny nSP architectures. The memory requirement for the Standard implementation (code and data) ranges between 9 and 11.5 Bytes with the exception of the moving average filter which uses 59 Bytes. The Tiny implementations all fit within the limited 8 Byte memory space. For most of the applications, the memory footprint is dependent on the number of monitored sensors; more sensors requires more memory space. For brevity, we present the Standard nSP code for only two applications, pathogen counting and a multi-analyte probe.

```
0 JMP (!send) 6      // if not sending, count
3 OUTCLR 13          // send data and clear counter
6 JMP (!A) 18        // if no analyte is bound go to 18
9 BNZ 0              // analyte is bound, if acc is 0 go to next cycle
12 INCI              // increment count, update acc
15 JMP 0              // jump to next cycle
18 CLR               // clear acc (make last event "not bound")
19 JMP 0              // jump to next cycle
```

Figure 5-3: 8-bit event counter (Pathogen Counting).

The nSP program in Figure 5-3 implements the pathogen counting algorithm, which monitors a single, reversible, pathogen sensor and outputs the number of 1-to-0 transitions observed since the previous report. An 8-bit counter is used to accumulate up to 255 events between output reports. The total memory footprint is 11 Bytes and a saturating counter version (omitted for brevity) uses 14.5 Bytes. This compact code is achieved by using IFS for event detection (i.e., 1) a pathogen is present and 2) the result should be transmitted). The INCI instruction also provides compact accumulation of the counter.

```

0  JMP (!A) 0          // if not A jump to self
3  JMP (!B) 3          // if not B jump to self
6  JMP (!C) 3          // if not C jump to previous
9  JMP (!D) 9          // if not D jump to self
12 JMP (E) 9           // if not E jump to done
15 OUT 1              // output non-zero value

```

Figure 5-4: Multi-analyte probe implementation.

The role of a multi-analyte probe is to detect specific sequences of analytes and their time order, in this example (A) then (B and C) then (D and not E). We use IFS to map the analyte ordering on top of executed control logic (Figure 5-4) and guarantee that the program control path, which is dynamically changed by the analytes, reaches its output phase only when it interacts with the target sequence of analyte events. A single IFS instruction (JMP) is sufficient to sense and process each analyte in the intended evaluation sequence. The total memory footprint for the Standard nSP implementation is 8.5 Bytes.

The remaining applications all require less than the 128 Bytes available on the Standard nSP. Our FIR implementation, that uses a moving average, is the largest, most complex application and it requires just below 60 Bytes. Kinetic analysis and Imaging each require around 10 Bytes.

Counter	Multi-Analyte
0 JMP (!send) 4 2 OUTCLR 9 4 JMP (!A) 12 6 BNZ 0 8 INCI 10 JMP 0 12 CLR 13 JMP 0	0 INCI (!A) 2 INCI (!B) 4 INCI (!C) 6 INCI count 8 BNZ 0 10 OUTCLR 1 12 OUTCLR 3 14 OUTCLR 5
Imaging	Kinetic Analysis
0 INCI count 2 OUT 1 3 JMP 0 5-15 SENSORS	0 JMP (!A) 0 2 JMP (!B) 2 4 JMP (!C) 2 6 JMP (!D) 6 8 JMP (E) 6 10 OUT 2

Table 5-3: Tiny nSP Programs (8 Byte Memory Space)

Table 5-3 shows the Tiny nSP implementations for four applications. FIR is too complex to fit within the 8 Byte limitation. The main cost of using Tiny nSPs is that dynamic range for counting and accumulation is reduced from 8 bits to 4 bits and the total number of sensors that can be monitored is much more limited. The fundamental advantage of the Tiny nSP is their diminutive size: they can diffuse through and sample molecular environments that are inaccessible to the larger Standard nSP.

5.4.3 Impact of Instruction-Fused Sensing

A single IFS instruction can replace several non-IFS operations and significantly reduce the memory requirement for applications. Figure 5-5 shows the IFS and non-IFS implementations of the sample multi-analyte probe application for the Standard nSP. The non-IFS code allocates memory locations for sensors and reads the sensor value with explicit load operations, leading to memory footprint of 21 Bytes versus the 9 Bytes of the IFS version.

0	JMP (!A)	0	0	LD	37
3	JMP (!B)	3		NOT	
6	JMP (!C)	3		BNZ	0
9	JMP (!D)	9		LD	38
12	JMP (E)	9		NOT	
15	OUT	3		BNZ	7
				LD	39
				NOT	
				BNZ	7
				LD	40
				NOT	
				BNZ	21
				LD	41
				BNZ	21
				OUT	3
				sensorA	
				sensorB	
				sensorC	
				sensorD	

Figure 5-5: Code size impact of IFS on the multi-analyte probe. Left: IFS (9 bytes). Right: LD/ST (21 bytes)

Figure 5-6 shows the total memory required by IFS relative to non-IFS (load/store) implementations of our applications for the Standard nSP. IFS reduces the footprint between 58%, in the case of the multi-sensor analyte probe, and 5%, for the single-sensor, processing intensive FIR.

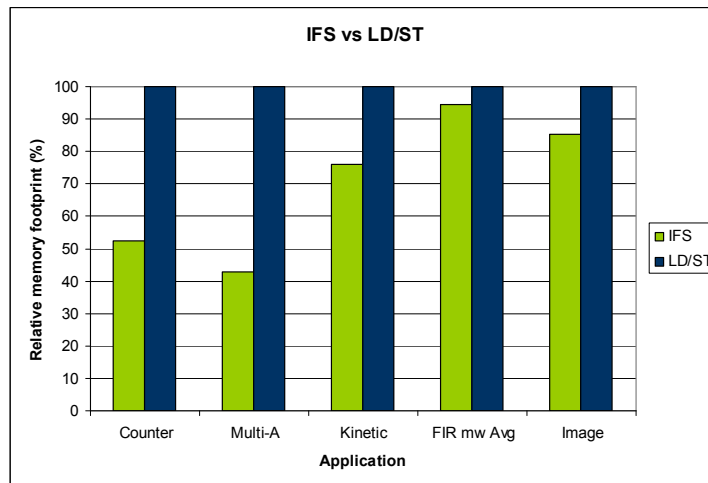


Figure 5-6: Impact of using IFS on the memory requirement of target nSP applications.

A tradeoff in using IFS is that instructions become statically bound to sensors, preventing conventional code size reducing techniques, like procedures or loops. Figure 5-7 explores this

tradeoff. For each application we show on the y axis the number of sensors that can be processed by IFS and LD/ST implementations as we increase the maximum memory available on a Standard nSP. For both implementations we unroll loops when unrolling allows an increase in the number of sensors for the given memory size.

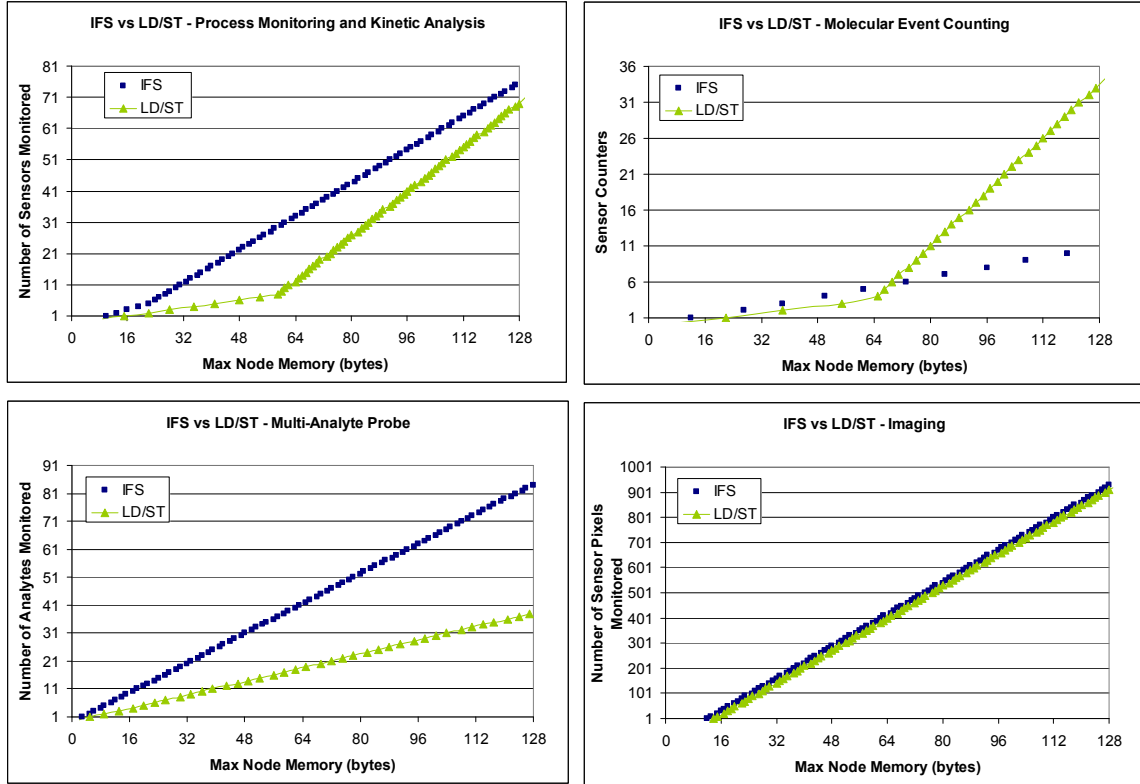


Figure 5-7: Comparison of IFS and LD/ST implementations of applications. The available nSP node memory (X axis) and the number of sensors to be processed (Y axis) influence the relative benefit of using IFS.

Within the range of our Standard nSP addressable memory, 128 Bytes, IFS is generally more efficient than LD/ST, i.e., more sensors can be processed for a given memory size. An exception is the pathogen counter application where the traditional LD/ST implementation is more efficient when available memory is more than 64 Bytes and we wish to count more than 5 pathogens. With more memory, loop overhead can be amortized over more sensors. The same characteristic can be seen for the kinetic analysis application; however, in this case the break-

even point where LD/ST becomes more memory efficient than IFS is beyond the maximum addressable memory range of our nSPs.

5.4.4 Application Simulation Results

We verify the expected output of nSP applications using a simple cycle-level nSP functional simulator augmented with chemical environment and sensor-analyte interaction simulation. Memory access (for a 4-bit word, including sensor read) and arithmetic operations are performed in a single cycle. The total number cycles per instruction varies between 2 and 6 depending on instruction length and number of memory accesses.

The environment simulation models time-varying concentrations of analytes and the corresponding binding and dissociation events for each nSP sensor. The binding event probability is modulated by binding and dissociative rate constants which are explicitly specified for all distinct sensor-analyte pairs.

For each application we initialize the nSP with the appropriate program, simulate a chemical environment characteristic for that application and follow the program output in time. The following details the results.

Pathogen Counting. We simulate an influenza virus environment using published pathogen period and dwell time for anti-hemagglutinin based sensors [60]. Figure 5-8 (bottom graph) shows the output of a Standard nSP running the pathogen counting code from Figure 5-3 in the presence of a time-varying pathogen concentration (top). The nSP clock cycle time is 100Hz, and the output is requested, via an external optical send signal, every 1000 seconds.

When requested, the program outputs the number of observed pathogen binding events since the last transmission. As expected, the value of the output is correlated with the pathogen concentration and shows variations due to stochastic (single-molecule) sensor binding. Observing this trend could be used to diagnose an infection.

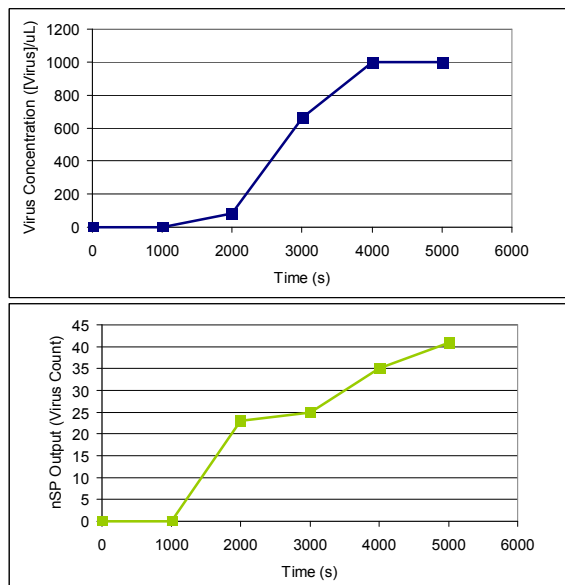


Figure 5-8: Influenza-A virus counting simulation. The nSP node output (bottom) in the presence of the send request signal (middle) follows the virus presence (top).

The minimum nSP clock cycle time is determined by the timescale of the analyte-sensor interaction. If the program samples sensors too slowly, then binding events could be missed. In this experiment the critical sampling threshold is less than 1 second (the average dwell time for this pathogen-sensor combination). Therefore, the nSP clock rate must be fast enough to ensure the program samples the sensors frequently enough. Figure 5-9 shows the output of the virus counting application running at various nSP clock rates (averaged over ten queries taken 1000 seconds apart). The virus concentration and the window of time over which the nSP counts binding events are held constant. Given our multicycle nSP, the clock frequency must be 100 Hz or greater to avoid a misdiagnosis. At lower clock rates pathogen binding events are missed as reflected by the decreasing counter value.

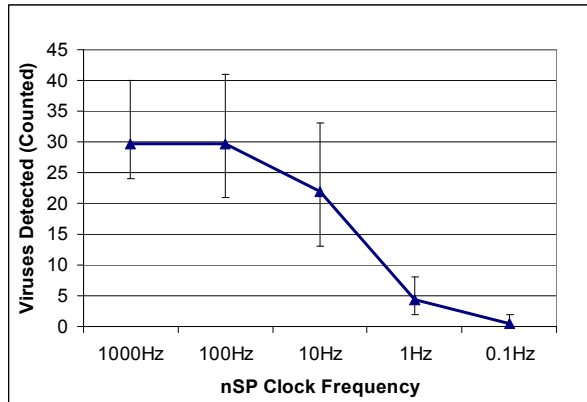


Figure 5-9: The pathogen binding kinetics determine the minimum nSP clockrate before counting becomes inaccurate due to missed events.

Multi-Analyte Probe. We model 5 generic analytes (A-E) and execute the molecular probe application code from Figure 5-4, which detects the (A) then (B and C) then (D and not E) sequence of events. Figure 5-10 shows the input concentration of each analyte and the program output (OUT) over time.

The result emphasizes the local, single-molecule sensing characteristics of the probe. Even though there is still some concentration of analyte E present in the system, the program asserts its detection output (just before the 8s mark). The reason is the stochastic nature of the output decision, based on instantaneous nSP-local values of sensors which will probabilistically encounter time intervals with no bound analyte, even if globally the analyte is still present. This could be eliminated by observing analytes over a longer window of time to determine their presence or absence.

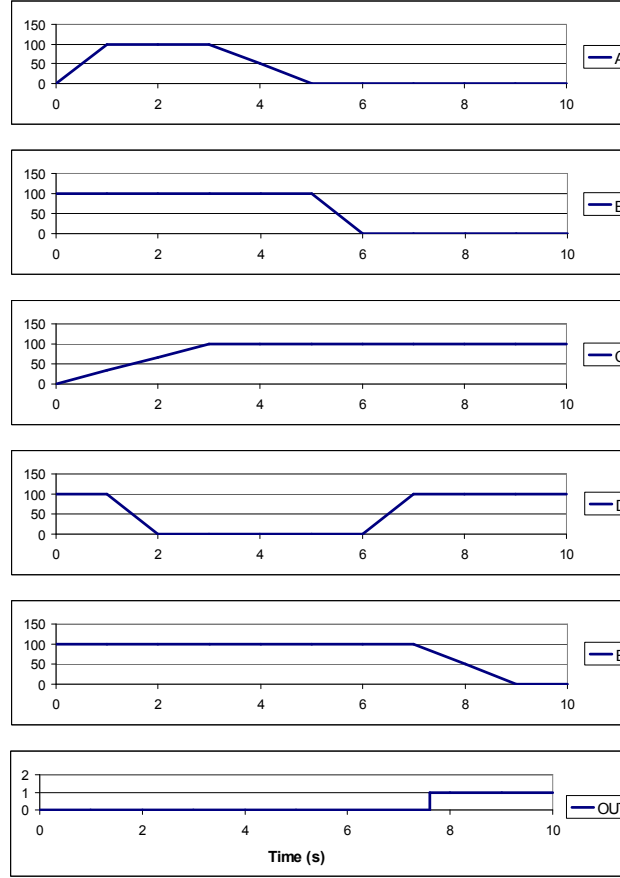


Figure 5-10: Multi-analyte probe simulation: the node output (OUT) depends on the sequence of analytes (A,B,C,D,E).

5.5 Related Work

The most closely related work to ours falls within the general realm of amorphous computing [1], which is predicated on the existence of large numbers of inexpensive devices with limited computational ability, limited memory capacity, and limited communication range. The set of potential applications for amorphous computing is vast, ranging from smart paint to in vivo computation for biological applications.

Our work also has similarities to early microprocessor designs [24] and the broad area of sensor networks [42, 44] and ultra-low power sensor processors [108]; however, our small scale creates significantly different resource constraints.

Other work explores novel molecular logic, but currently only presents individual gate functionality [17]. Computational devices that function on cellular biological substrates[70, 75, 101] have the potential to interface directly with gene expression and cellular function, however their application space is specific and scaling to complex computing systems is a challenge. In contrast with DNA computing[2] we use DNA as a substrate for molecular logic instead of combinatorial computation.

In synthetic biology[10] the biological cell is the computer. Through engineering of biological processes, researches have demonstrated switches[30] and logic gates[3, 30, 107] that can form the basis for more complex synthetic digital logic circuits. The close integration of such circuits with cellular molecular components is a strong advantage for biological applications. However, current synthetic biology circuits are slow (gate response times in the order of several hours), are limited to the cellular context and are prone to interference from other cellular processes. In contrast, nSPs are using optical circuits with nanosecond switching time and can function in multiple environments, both biological and non-biological.

Other closely related work includes the Decoupled Array Multiprocessor (DAMP) [20], the Nano-scale Active Network Architecture (NANA) [61] and the Self-Organizing SIMD Architecture (SOSA) [62] which all use DNA-based self-assembly of nano-electronic devices. Our work also uses DNA self-assembly but focuses on novel single molecule optical devices, thus achieves higher density and provides an efficient method for macro-scale interfacing (pitch matching in electronics).

5.6 Conclusion

Two driving forces on computer architecture are application requirements and technology change. The combination of important problems in the life sciences and advances in material science are exposing a new computational domain: biological scale integrated sensing and

processing. The ability to utilize programmable devices at biological scales may enable life scientists to perform hypothesis testing previously thought impossible. This domain presents new challenges to computer architects due to the extreme size constraints: a device must be capable of diffusing through small volumes while still meeting application requirements.

This chapter introduces an architecture for nanoscale sensing and processing. We analyze the application characteristics (e.g., long time scales and common operations) to design a multicycle accumulator-based architecture. A novel aspect of this architecture is the use of instruction-fused sensing that exploits the unified use of nanoscale devices for both sensing and logic design to allow sensors to directly modify logic values (i.e., instruction opcode bits). We implement several representative applications that execute on our proposed architecture and demonstrate capabilities (e.g., sensing based on complex logic) beyond those achievable with current simple biological sensors. This work shows our first steps toward developing biological scale computing.

6 Conclusion

6.1 *Thesis Summary*

In this thesis we mapped a potential path toward achieving molecular-scale computing. We make contributions in the areas of nanoscale fabrication techniques, molecular digital logic devices, integrated sensing elements, and architectural design of nanoscale sensor processors and show how these advances vertically integrate to enable new applications domains for computer systems.

In Chapter 2 we develop and experimentally demonstrate a scalable, cost-effective DNA self-assembly-based fabrication technique for molecular circuits. Our method uses thermodynamic analysis and design automation techniques to select optimized DNA sequences and can achieve the fabrication of larger programmable structures than have been previously demonstrated by tile- or motif-based methods. We validate this method by assembling a 140nm \times 140nm DNA grid, one of the largest aperiodic synthetic nanostructures ever synthesized. The grid design supports scaffolding of nanoscale components through complete chemical addressability, which we experimentally demonstrate by assembling arbitrary circuit-type patterns of small molecules.

In Chapter 3 we propose and evaluate RET-logic circuits, a novel nanoscale technology for computing based on single-molecule optical devices. The theoretical foundation of our devices and circuits is Resonance Energy Transfer (RET) and we propose a new optically switched gate designed using four chromophores. We show that RET-logic is a complete technology and present the design and layout of several circuit elements. The densities achievable on existing DNA nanostructures results in a D-Latch occupying 20nm \times 40nm, a complete SRAM cell occupying 40nm \times 60nm, and a full adder occupying 40nm \times 40nm. We also present results from the experimental assembly of RET-logic OR gates on DNA structures.

In Chapter 4 we integrate RET molecular logic circuits with sensing and demonstrate the selective identification of label-free biomolecules in solution by optical multiplexing with binary encoded inputs. The resulting circuits can detect femtomole quantities of proteins, DNA oligomers, and small fragments of RNA (5-nt) in solution. This method, which creates up to twenty-four 8-nm³ logic gates on a 60nm x 60nm DNA grid, is a scalable step toward nanoscale logic capable of interfacing computers with biological processes.

Finally, in Chapter 5 we explore the architectural implications of integrating computation and molecular sensors to form nanoscale sensor processors (nSP), nanoscale-sized systems that can sense, process, store and communicate molecular information. We show that nSPs may enable new computing domains and automate tasks that currently require expert scientific training and costly equipment. This new application domain severely constrains nSP size, which significantly impacts the architectural design space. In this context, we explore nSP architectures and present an nSP design that includes a simple accumulator-based ISA, sensors, limited memory and communication transceivers. To reduce the application memory footprint, we introduce the concept of instruction-fused sensing. We use simulation and analytical models to evaluate nSP designs executing a representative set of target applications. Furthermore, we evaluate an nSP implementation using optical Resonance Energy Transfer (RET) logic on DNA grid substrate that enables the small size required by the application domain; our smallest design is about the size of the largest known virus.

6.2 *What's Next?*

Looking forward, we think that material science advances will continue to push the boundary of where and how we can apply computation and will expose new opportunities through which computer architects can address the challenges of new and evolving applications domains.

One trade-off in using self-assembly manufacturing techniques is the increased number of defects in the resulting structures. How to achieve reliable computation with unreliable components in resource-constrained computational elements is a vital and challenging research question. Particularly promising to investigate in this space are techniques that integrate architectural mechanisms for fault tolerance with technological advances, like self-healing and sequential assembly, to ensure reliability at the application level.

Processing elements that can access and compute in biological-scale environments enable a wide range of life-sciences applications. Their nanoscale size also means that we can place massive numbers ($>10^{12}$) of these processors in small volumes. To exploit such multi-node systems current approaches propose to create networks of nodes using hybrid CMOS designs or random self-assembled structures. However, adding these networks results in significant manufacturing challenges and can also severely limit the target application space. Can we remove the physical network requirement and still provide system-wide processing? What type of computation and applications could such a system support?

For example, in RET-logic nSP systems the mechanisms for external communication (input through excitation at specific wavelengths and output by emission at specific wavelengths) can be exploited to provide communication between nSP nodes suspended in an aqueous solution. At sufficiently high concentrations, nodes would come into physical contact with one another periodically and exchange information. The period of time between node interactions (i.e., diffusion time) is proportional to $\langle X \rangle^2 \cdot D^{-1}$, where $\langle X \rangle$ is the average node-node separation and D is the diffusion constant of a node. We call this diffusion limited computation. For the nodes to successfully collaborate on larger problems it is important to balance the size of the node (i.e., D), the concentration of nodes (i.e., $\langle X \rangle$), and the available resources for computation between interactions.

Diffusion limited computation could be used in biological applications, for example to compute the average binding rate across large set of proteins. More generally, we can apply diffusion limited computation to design computing systems in which nanoscale information from across large macroscale domains can be integrated and queried, similar to traditional databases. Nanoscale processing elements could provide both the data, from the vast aggregate set of sensors, and the distributed query execution engine. It is interesting to note that the architectural challenges of designing massively parallel systems with distributed nodes that have limited resources and unreliable communication apply not just to some of the largest computing systems that we design today, but also to some of the smallest.

Appendix A

A.1 Optical Gates

A.1.1 Chromophore functionalization

For chromophore-DNA functionalization we used standard maleimide-thiol conjugation. Maleimide-conjugate Rhodamine-Red (RR), Oregon Green 488 (OG), Alexa-Fluor 532 (AF) and Pacific Orange (PO) chromophores from Molecular Probes / Invitrogen were suspended in DMSO at 2.5mM concentration. 5' and 3' thiol-terminated ssDNA shell strands from IDT-DNA were suspended in 1 × TAE buffer at 30μM concentration. A solution of thiolated ssDNA with 60x excess of freshly prepared TCEP reducing agent was incubated for 30min at 80°C, followed by the addition of 60x maleimide-chromophore excess and a further 3h at 80°C and 12h at 4°C incubation. All materials and buffers were degassed prior to use.

Excess free dye was filtered with Millipore Microcon YM-3 membrane centrifugal filters in 9-10 filtering steps. At each step the retentate was restored to 1mL through the addition of 1 × TAE/Mg²⁺ buffer and spun for ~20 min at 14000g to reduce the sample volume to ~100μL. The chromophore concentration in the filtrate was monitored at each step using absorbance measurements until only trace amounts were detectable.

DNA recovery varied between 30% and 70%. The strands with attached chromophores were used during tile anneals to assemble functionalized tiles and grids.

Chromophore	Abs (nm)	Em (nm)
Pacific Orange	400nm	551 nm
Oregon Green	496 nm	524 nm
Alexa Fluor 532	528 nm	553 nm
Rhodamine Red	572 nm	590 nm

Table S 1: Absorption and emission peaks for DNA-bound chromophores in 1xTAE/Mg²⁺ buffer

A.1.2 Gate configuration on 4x4 grid

We place two gates on the grid, each with three chromophores. For Gate 1 Rhodamine Red is attached to the 5' end of a shell strand on tile 10 (T10) and Pacific Orange and Alexa Fluor 532 are attached to 5' end and 3' end respectively of shells on T14 (Figure S 1). For Gate 2 Rhodamine Red is attached to the 5' end of a shell strand on tile 2 (T2) and Oregon Green 488 and Alexa Fluor 532 are attached to 5' end and 3' end respectively of shells on T16.

The input and output chromophores of each gate are separated by two 5bp double-helical domains of hybridized sticky-ends. The estimated inter-chromophore distances are AF-RR 2.6nm, OG-RR and PO-RR 1.7nm, AF-OG and AF-PO 2.0nm. Figure S 2 shows an AFM image of 4x4 grids that were functionalized with the two optical gates.

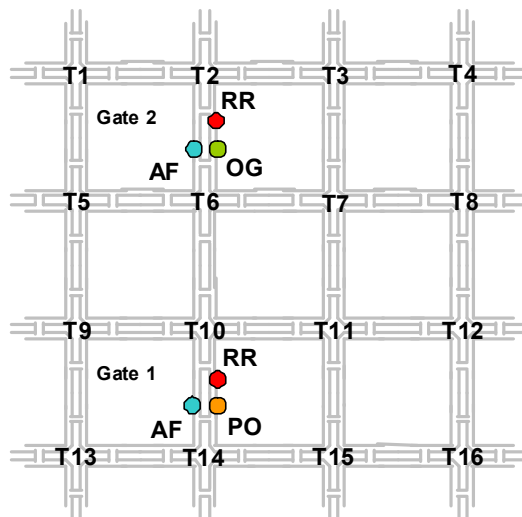


Figure S 1: Chromophores are attached to tile shell-strand ends to form gates on assembled 4x4 grids.

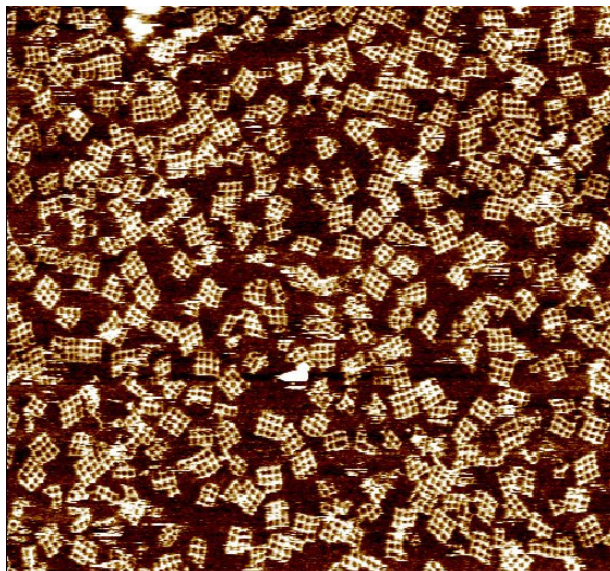


Figure S 2: AFM image of 16-tile DNA grids with two optical gates. The gate chromophores are too small to be visible in this AFM scan.

A.1.3 DNA sensing gates and target analytes

For DNA sensing we assemble the configuration from Figure S 1 and use the base-sequence of the intra-gate sticky-ends to achieve analyte specificity. Each gate has two sticky-end regions:

Gate 1:

S-End sequence 1: 5'- CACAG -3' (+ complement)

S-End sequence 2: 5'- GTGCA -3' (+ complement)

Gate 2:

S-End sequence 1: 5'- GCTTG -3' (+ complement)

S-End sequence 2: 5'- GTCGT -3' (+ complement)

For the DNA sensing experiment we use the following target analytes:

Analyte	Target Gate	Base Sequence
A ₁	Gate 1	5'- CTGTGCGGCGTGTGGTTGCATTGCAC -3'
B ₂	Gate 2	5'- CAAGCCGGCGTGTGGTTGCATACGAC -3'

Ctrl	-	5'- TAAGAGATAGAGTGGTACATCTAAGT -3'
------	---	------------------------------------

Table S 2: DNA sensing analytes

A.1.4 RNA sensing gate and target analytes

For RNA sensing experiment we assemble the configuration from Figure S 1 and use the base-sequence of the intra-gate sticky-ends to achieve analyte specificity. We use the same sticky-end sequences as shown for DNA sensing. We observed experimentally that DNA-RNA interaction at room temperature for short 5-nt RNA strands is too weak to compete with the existing DNA-DNA sticky-end interaction (the IRET differential of analyte and control sensing runs with 8nM grid, 400nM RNA was below the acquisition noise level). To increase the melting temperature of the analyte-gate interaction we replace one of the sticky-ends of Gate 2 with the LNA equivalent.

Gate 2:

S-End sequence 2: LNA 5'- ACGAC -3' (+ DNA complement)

For RNA sensing analytes we use the LNA-complementary 5-nt RNA strand and a 5-nt “randomer” for control:

Analyte	Target Gate	Base Sequence
B ₂	Gate 2	RNA 5'-GUCGU-3'
Ctrl	-	RNA 5'-UCUAG-3'

Table S 3: RNA sensing analytes

A.1.5 Protein sensing gate and target analytes

For protein sensing experiment we assemble the configuration from Figure S 1. Additionally, we use biotin pre-functionalized arm strands on gate tiles such that in the assembled configuration a biotin is present next to each gate chromophore. We add biotins to Gate 2 only.

Protein sensing analytes:

Analyte	Target Gate	Protein
B ₂	Gate 2	Streptavidin
Ctrl	-	Bovine Serum Albumin

Table S 4: Protein sensing analytes

Figure S 3 shows an AFM image of 4x4 grids after being exposed to streptavidin on a sensing run. Bound proteins are visible at the expected gate locations.

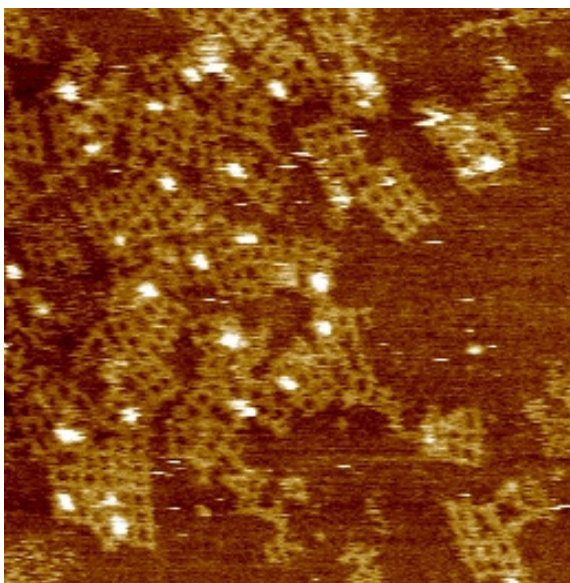


Figure S 3: 1 μ m \times 1 μ m AFM image of dual-gate 4x4 DNA grids with bound streptavidin (16nM grid, 32nM SA, 1 \times TAE/Mg²⁺).

A.2 Sensing

For optical readout we use a custom-built dual-beam spectrometer with a 500W Hamamatsu Mercury-Xenon lamp light source and OceanOptics S2000 Fiber Optic spectrometer (CCD sensor). The SpectraSuite operating software from OceanOptics is used for data

acquisition. Cuvette holders are temperature-controlled by circulating water from programmable water baths.

A.2.1 Melting: increasing binding site accessibility

We found that the binding site accessibility at room temperature is too low to influence I_{RET} . An increase in temperature (melt) significantly increases accessibility. Table S 5 shows the I_{RET} modulation for DNA sensing with 2nM grid/16nM analyte. For the “Melt” run we used the procedure in SOM 0, heating and cooling the sample over 30min. For the “No Melt” run we maintain the sample temperature constant over the same 30min. No significant I_{RET} modulation is detected in this case.

Analyte	Gate 2, Melt	Gate 2, No Melt
B ₂	0.173	0.002
Ctrl	0.150	0.004

Table S 5: I_{RET} delta for DNA sensing (2nM grid, 16nM analyte) with and without melting to 37°C. Melting is necessary to make the binding site accessible.

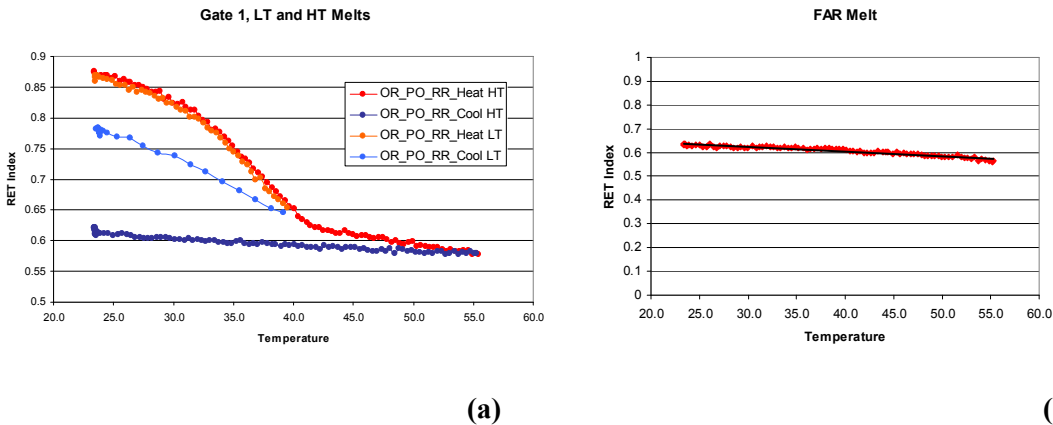


Figure S 4 (a) I_{RET} monitoring with Gate 1 excitation of dual-gate grid during low-temperature, recoverable melting and high-temperature, disruptive melting (no analytes are present). (b) I_{RET} monitoring of grids with same chromophores as the dual-gate but placed at large distances of each-other (FAR configuration - see SOM Section 0)

Figure S 4(a) shows I_{RET} values with Gate 1 excitation of dual-gate grid during low-temperature, recoverable melting and high-temperature, disruptive melting (no analytes are present). AFM images of dual-gate grids before and after melts are displayed in Figure S 5. Figure S 4 (b) shows I_{RET} monitoring of grids with same chromophores as the dual-gate but placed at distances much larger than their relative Forster radii in order to prevent RET (FAR configuration - see SOM Section 4.3). The data tracks the temperature dependence of the base I_{RET} value for a system chemically equivalent to the dual-gate but with no significant RET.

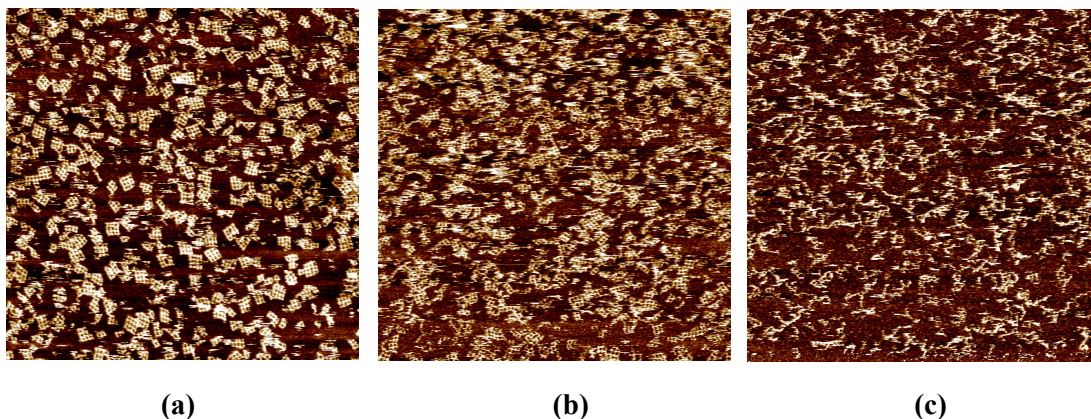


Figure S 5: AFM images of dual-gate grids (a) after low-temperature melt (b) and after high-temperature melt (c)

A.2.2 Sensing procedure

We add and mix 70 μ L 1xTAE/Mg²⁺ buffer and 5 μ L dual-gate DNA grid inside the cuvette. After allowing 10 minutes for the sample to achieve thermal equilibrium at 18°C we take an initial set of dual-beam fluorescence measurements. For the 4nM grid and 8nM grid runs we use 10 sec exposures and an averaging factor of 20 for a total of 200 seconds per spectrum acquisition. In the next step we add 2 μ L of analyte, mix and heat the sample to 37°C over 12 minutes followed by cooling back to 18°C over 30 minutes. The temperature profile is shown in

Figure S 6. After the cooling period the final set of dual-beam fluorescence measurements are taken with the same acquisition settings. I_{RET} and ΔI_{RET} are calculated based on acquired spectra.

The total sample volume is 80 μ L. The geometrical volume exposed to input excitation light is approximately 25 μ L. The excitation intensity at each input wavelength is adjusted such that the generated output chromophore counts in the dual-gate system are approximately the same for each input.

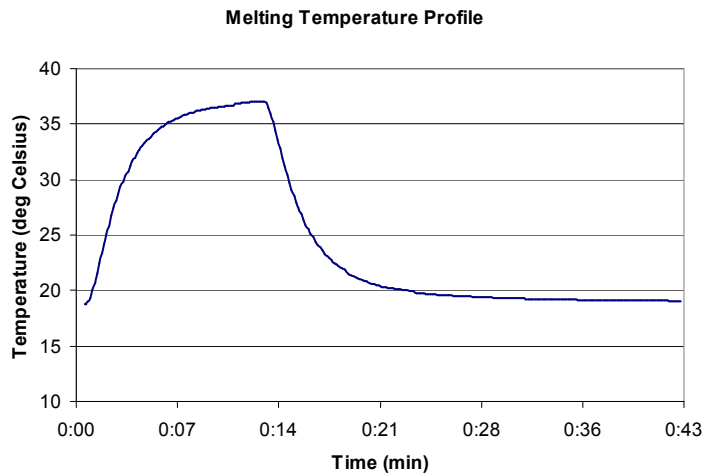


Figure S 6: Sensing temperature profile: heating (12 min) and cooling (30min).

A.2.3 Impact of structural configuration on sensing

To evaluate the impact of the specific gate configuration on sensing we use the 4x4 grid to assemble a system with the same number and type of chromophores but attached at distances much greater than their respective Forster distances. The output chromophores remain in the same position as in the dual-gate to avoid changes in their micro-environment. A diagram of this configuration, which we call FAR, is shown in (Figure S 7).

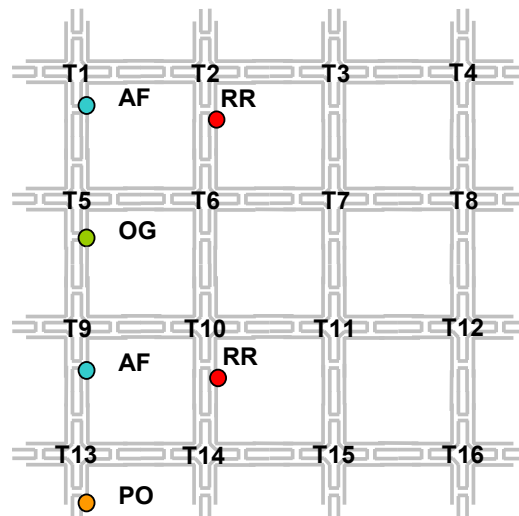


Figure S 7: FAR configuration: same chromophores as used in the dual-gate are attached at distances $>3\times$ their respective Forster distances to prevent RET.

Table S 6 and Table S 7 show the ΔI_{RET} for DNA sensing with dual-gate grids and FAR grids respectively. We note the absence of I_{RET} modulation for FAR grids, which shows that RET is vital for sensing and the optical modulation in sensing runs is not due to direct interaction of the analytes with the acceptor (output) chromophores.

A ₁	B ₂	Ctrl	Gate 1 Ex	Gate 2 Ex
-	-	++	0.160	0.164
+	-	+	0.221	0.202
-	+	+	0.198	0.264
+	+	-	0.241	0.260

Table S 6: ΔI_{RET} for DNA sensing with dual-gate grids (8nM grid, 400nM DNA analyte)

A ₁	B ₂	Ctrl	FAR Gate 1 Ex	FAR Gate 2 Ex
-	-	++	0.008	0.004
+	-	+	0.001	-0.002
-	+	+	0.000	-0.001
+	+	-	0.008	0.002

Table S 7: ΔI_{RET} for DNA sensing with FAR grids ((8nM grid, 400nM DNA analyte)

A.2.4 Grid concentration

We mapped the gate sensitivity for 4nM grid and 1x-50x DNA analyte concentration (Paper Figure 5). We made several DNA sensing experimental runs with various grid concentrations and observed that data points were consistent with the 4nM I_{RET} sensitivity curve profile. The concentrations we tested were 8nM grid/50x analyte (Figure 4) and 2nM grid/16nM analyte (

Table S 5). The lowest grid/analyte concentration we used was 400pM grid/800pM analyte. Given the lower fluorescence counts and increased noise to signal we used in this case an extended acquisition time of 15 minutes (15sec exposure, 60 averages) and recorded an average control/analyte I_{RET} separation of 0.023 for DNA sensing on Gate 2.

A.3 Data Fit

We use a Generalized Reduced Gradient nonlinear solver to optimize the least-square sum of residuals between the averaged experimental and analytical dual-gate output values under each excitation pattern.

Table S 8 shows the results for the most constrained system (DNA sensing with two target analytes and one control) from Figure 6. The distance-only solver assumes that all chromophores are free rotators and attempts to fit using only inter-chromophore distance modulation upon analyte binding. We note that the solution is geometrically inconsistent due to several large distances (which by themselves are unlikely in the designed DNA grid configuration). By modulating both distances and angular orientations we obtain a more plausible solution with

relatively small distances. The minimum distance is 0.5nm and minimum κ^2 is 0.005 since our bound chromophores are not perfectly rigid.

Fit to:	Distance	Distance and Angle
Cumulative residual (LSR)	0.00110574	0.00110561
Functional Yield	0.3518027	0.3518027
Recovery (f_r)	0.7545284	0.7545284
Activity or binding fraction	1	1
Initial State		
Dist (Å)		
$r_{1,o}$	5	17
$r_{2,o}$	5	11
$r_{1,2}$	950	21
$r_{3,o}$	5	13
$r_{4,o}$	5	10
$r_{3,4}$	343	21
Orientation		
$k_{1,o}$	0.667	1.178
$k_{2,o}$	0.667	4.000
$k_{1,2}$	0.667	3.386
$k_{3,o}$	0.667	4.000
$k_{4,o}$	0.667	4.000
$k_{3,4}$	0.667	1.596
Bound State (final)		
Dist (Å)		

$r_{1,o}$	54	36
$r_{2,o}$	49	26
$r_{1,2}$	100	20
$r_{3,o}$	67	52
$r_{4,o}$	44	26
$r_{3,4}$	110	27
Orientation		
$k_{1,o}$	0.667	0.005
$k_{2,o}$	0.667	0.014
$k_{1,2}$	0.667	0.011
$k_{3,o}$	0.667	0.005
$k_{4,o}$	0.667	0.031
$k_{3,4}$	0.667	0.005

Table S 8: Analytical fit for the dual-gate system for DNA sensing.

References

- [1] H. Abelson, D. Allen, D. Coore, C. Hanson, G. Homsy, T. F. Knight, R. Nagpal, E. Rauch, G. J. Sussman, and R. Weiss, "Amorphous Computing," *Communications of the ACM*, vol. 43 (5), pp. 74-82, 2000.
- [2] L. Adleman, "Molecular Computation of Solutions to Combinatorial Problems," *Science*, vol. 266, pp. 1021-1024, 1994.
- [3] J. C. Anderson, C. A. Voigt, and A. P. Arkin, "Environmental Signal Integration by a Modular AND Gate," *Mol Syst Biol*, vol. 3, pp. -, 2007.
- [4] J. Andreasson, S. D. Straight, T. A. Moore, A. L. Moore, and D. Gust, "Molecular All-photonic Encoder-decoder," *Journal of the American Chemical Society*, vol. 130 (33), pp. 11122-11128, 2008.
- [5] A. Bachtold, P. Hadley, T. Nakanishi, and C. Dekker, "Logic Circuits with Carbon Nanotube Transistors," *Science*, vol. 294, pp. 1317-1320, 2001.
- [6] V. Balzani, A. Credi, and M. Venturi, "Molecular Logic Circuits," *ChemPhysChem*, vol. 4 (1), pp. 49-59, 2003.
- [7] R. D. Barish, P. W. K. Rothmund, and E. Winfree, "Two computational primitives for algorithmic self-assembly: Copying and counting," *Nano Letters*, vol. 5 (12), pp. 2586-2592, 2005.
- [8] R. Baron, O. Lioubashevski, E. Katz, T. Niazov, and I. Willner, "Elementary Arithmetic Operations by Enzymes: A Model for Metabolic Pathway Based Computing," *Angewandte Chemie International Edition*, vol. 45 (10), pp. 1572-1576, 2006.
- [9] Y. Baryshnikov, E. Coffman, N. Seeman, and T. Yimwadsana, "Self-correcting Self-assembly: Growth Models and the Hammersley Process," *DNA Computing Lecture Notes in Computer Science*, vol. 3892, pp. 1-11, 2006.
- [10] S. Benner and A. M. Sismour, "Synthetic biology," *Nature Reviews Genetics*, vol. 6 (7), pp. 533-543, 2005.
- [11] D. S. Bradshaw and D. L. Andrews, "Optically Controlled Resonance Energy Transfer: Mechanism and Configuration for All-optical Switching," *Journal of Chemical Physics*, vol. 128 (14 144506), pp. -, 2008.
- [12] D. W. Brousmiche, J. M. Serin, J. M. J. Frechet, G. S. He, T.-C. Lin, S. J. Chung, and P. N. Prasad, "Fluorescence Resonance Energy Transfer in a Novel Two-Photon Absorbing System," *Journal of the American Chemical Society*, vol. 125, pp. 1448-1449, 2003.
- [13] P. J. Burke, "Carbon Nanotube Devices for GHz to THz Applications," *Spie*, vol. 5593, pp. 52-61, 2004.

- [14] L. Chalet and F. J. Wolf, "Properties of Streptavidin Biotin-binding Protein Produced by Streptomyces," *Archives of Biochemistry and Biophysics*, vol. 106 (1-3), pp. 1-8, 1964.
- [15] A. Chworos, I. Severcan, A. Y. Koyfman, P. Weinkam, E. Oroudjev, H. G. Hansma, and L. Jaeger, "Building programmable jigsaw puzzles with RNA," *Science*, vol. 306 (5704), 2004.
- [16] L. R. Dalton, A. W. Harper, and B. H. Robinson, "The role of London forces in defining noncentrosymmetric order of high dipole moment*high hyperpolarizability chromophores in electrically poled polymeric thin films," *Proceedings of the National Academy of Sciences*, vol. 94, pp. 4842-4847, 1997.
- [17] A. P. de Silva and N. D. McClenaghan, "Molecular-Scale Logic Gates," *Chemistry - A European Journal*, vol. 10 (3), pp. 574-586, 2004.
- [18] A. P. de Silva and S. Uchiyama, "Molecular Logic and Computing," *Nature Nanotechnology*, vol. 2 (7), pp. 399-410, 2007.
- [19] V. V. Didenko, "DNA Probes Using Fluorescence Resonance Energy Transfer (FRET): Designs and Applications," *BioTechniques*, vol. 31 (5), 2001.
- [20] C. Dwyer, J. Poulton, R. M. Taylor, and L. Vicci, "DNA Self-assembled Parallel Computer Architectures," *Nanotechnology*, vol. 15, pp. 1688-1694, 2004.
- [21] C. Dwyer, L. Vicci, J. Poulton, D. Erie, R. Superfine, S. Washburn, and R. M. Taylor, "The Design of DNA Self-Assembled Computing Circuitry," *IEEE Transactions on VLSI*, vol. 12, pp. 1214-1220, 2004.
- [22] C. Dwyer, S. H. Park, T. H. LaBean, and A. R. Lebeck, "The Design and Fabrication of a Fully Addressable 8-tile DNA Lattice," in *Proceedings of the Foundations of Nanoscience*, pp. 187-191, 2005.
- [23] D. Endy, "Foundations for Engineering Biology," *Nature*, vol. 438 (7067), pp. 449-453, 2005.
- [24] F. Faggin and M. E. Hoff, "Standard parts and custom design merge in four-chip processor kit," *Electronics*, pp. 112-116, 1972.
- [25] C. Fan, K. W. Plaxco, and A. J. Heeger, "Biosensors based on binding-modulated donor-acceptor distances," *Trends in Biotechnology*, vol. 23 (4), pp. 186-192, 2005.
- [26] U. Feldkamp, S. Saghaei, W. Banzhaf, and H. Rauhe, "DNASequenceGenerator: A Program for the Construction of DNA Sequences," in *Proceedings of the Seventh International Workshop on DNA Based Computers (DNA7)*, pp. 23-32, 2001.
- [27] L. A. Fendt, I. Bouamaied, S. Thoni, N. Amiot, and E. Stulz, "DNA As Supramolecular Scaffold for Porphyrin Arrays on the Nanometer Scale," *Journal of the American Chemical Society*, vol. 129 (49), pp. 15319-15329, 2007.

- [28] S. P. A. Fodor, "DNA Sequencing: Massively Parallel Genomics," *Science*, vol. 277 (5324), pp. 393-395, 1997.
- [29] S. Freescale, "MC9RS08KA2, MC9RS08KA2 Datasheet," 2007.
- [30] T. S. Gardner and C. R. Cantor, "Construction of a genetic toggle switch in *Escherichia coli*," *Nature*, vol. 403 (6767), pp. 339, 2000.
- [31] L. Gobbi, P. Seiler, and F. o. Diederich, "A Novel Three-Way Chromophoric Molecular Switch: pH and Light Controllable Switching Cycles," *Angewandte Chemie International Edition*, vol. 38 (5), pp. 674-678, 1999.
- [32] I. Golding, J. Paulsson, S. M. Zawilski, and E. C. Cox, "Real-Time Kinetics of Gene Activity in Individual Bacteria," *Cell*, vol. 123 (6), pp. 1025-1036, 2005.
- [33] R. P. Goodman, I. A. T. Schaap, C. F. Tardin, C. M. Erben, R. M. Berry, C. F. Schmidt, and A. J. Turberfield, "Rapid Chiral Assembly of Rigid DNA Building Blocks for Molecular Nanofabrication," *Science*, vol. 310 (5754), pp. 1661-1665, 2005.
- [34] S. Habuchi, R. Ando, P. Dedecker, W. Verheijen, H. Mizuno, A. Miyawaki, and J. Hofkens, "Reversible Single-molecule Photoswitching in the Gfp-like Fluorescent Protein Dronpa," *Proceedings of the National Academy of Sciences*, vol. 102 (27), pp. 9511--9516, 2005.
- [35] J. Hahn and C. M. Lieber, "Direct Ultrasensitive Electrical Detection of DNA and DNA Sequence variations using nanowire nanosensors," *Nano Letters*, vol. 4 (1), pp. 51-54, 2004.
- [36] C. V. Hanson, C.-k. J. Shen, and J. E. Hearst, "Cross-Linking of DNA in situ as a Probe for Chromatin Structure," *Science*, vol. 193 (4247), pp. 62-64, 1976.
- [37] A. W. Harper, S. Sun, L. R. Dalton, S. M. Garner, A. Chen, S. Kalluri, W. H. Steier, and B. H. Robinson, "Translating Microscopic Optical Nonlinearity into Macroscopic Optical Nonlinearity: the Role of Chromophore-chromophore Electrostatic Interactions," *Journal of the Optical Society of America B-optical Physics*, vol. 15 (1), pp. 329-337, 1998.
- [38] A. J. Hartemink, D. K. Gifford, and J. Khodor, "Automated Constraint-Based Nucleotide Sequence Selection for DNA Computation," 1998, pp. 227-235.
- [39] Y. He, Y. Chen, H. P. Liu, A. E. Ribbe, and C. D. Mao, "Self-assembly of Hexagonal DNA Two-dimensional (2D) Arrays," *Journal of the American Chemical Society*, vol. 127 (35), pp. 12202-12203, 2005.
- [40] M. Heilemann, P. Tinnefeld, G. S. Mosteiro, M. G. Parajo, N. F. V. Hulst, and M. Sauer, "Multistep Energy Transfer in Single Molecular Photonic Wires," *Journal of the American Chemical Society*, vol. 126, pp. 6514-6515, 2004.
- [41] M. Heilemann, E. Margeat, R. Kasper, M. Sauer, and P. Tinnefeld, "Carbocyanine Dyes As Efficient Reversible Single-molecule Optical Switch," *Journal of the American Chemical Society*, vol. 127 (11), pp. 3801--3806, 2005.

- [42] J. Hill, R. Szewczyk, A. Woo, S. Hollar, D. Culler, and K. Pister, "System Architecture Directions for Networked Sensors," in *Proceedings of the Asplos-ix: Proceedings of the Ninth International Conference on Architectural Support for Programming Languages and Operating Systems*, pp. 93--104, 2000.
- [43] Y. Huang, X. Duan, Y. Cui, L. J. Lauhon, K.-H. Kim, and C. M. Lieber, "Logic Gates and Computation from Assembled Nanowire Building Blocks," *Science*, vol. 294, pp. 1313-1317, 2001.
- [44] P. Juang, H. Oki, Y. Wang, M. Martonosi, L. S. Peh, and D. Rubenstein, "Energy-efficient Computing for Wildlife Tracking: Design Tradeoffs and Early Experiences with Zebnet," in *Proceedings of the Asplos-x: Proceedings of the 10th International Conference on Architectural Support for Programming Languages and Operating Systems*, pp. 96--107, 2002.
- [45] Y. G. Ke, S. Lindsay, Y. Chang, Y. Liu, and H. Yan, "Self-assembled Water-soluble Nucleic Acid Probe Tiles for Label-free RNA Hybridization Assays," *Science*, vol. 319 (5860), pp. 180-183, 2008.
- [46] A. Y. Koyfman, G. Braun, S. Magonov, A. Chworos, N. O. Reich, and L. Jaeger, "Controlled Spacing of Cationic Gold Nanoparticles by Nanocrown RNA," *Journal of the American Chemical Society*, vol. 127 (34), pp. 11886-11887, 2005.
- [47] J. R. Lakowicz, *Principles of Fluorescence Spectroscopy*. New York: Kluwer Academic / Plenum Publishers, 1999.
- [48] J. D. Le, Y. Pinto, N. C. Seeman, K. Musier-Forsyth, T. A. Taton, and R. A. Kiehl, "DNA-templated Self-assembly of Metallic Nanocomponent Arrays on a surface," *Nano Letters*, vol. 4 (12), pp. 2343-2347, 2004.
- [49] N. Le Novère, "MELTING, computing the melting temperature of nucleic acid duplex," *Bioinformatics*, vol. 17, pp. 1226-1227, 2001.
- [50] D. Liu, S. H. Park, J. H. Reif, and T. H. LaBean, "DNA Nanotubes Self-assembled from TX Tiles as Templates for Conductive Nanowires," *Proceedings of the National Academy of Science*, vol. 101, pp. 717-722, 2004.
- [51] H. P. Liu, Y. Chen, Y. He, A. E. Ribbe, and C. D. Mao, "Approaching the Limit: Can One DNA Oligonucleotide Assemble into Large Nanostructures?," *Angewandte Chemie-international Edition*, vol. 45 (12), pp. 1942-1945, 2006.
- [52] C. Mao, W. Sun, and N. C. Seeman, "Designed Two-Dimensional DNA Holliday Junction Arrays Visualized by Atomic Force Microscopy," *Journal of the American Chemical Society*, vol. 121, pp. 5437-5443, 1999.
- [53] V. Mao, "Self-Assembled DNA Scaffolds for Nanodevices," Duke University, 2007.

- [54] D. Margulies, G. Melman, and A. Shanzer, "A Molecular Full-adder and Full-subtractor, an Additional Step Toward a Molecular Computer," *Journal of the American Chemical Society*, vol. 128 (14), pp. 4865-4871, 2006.
- [55] D. Margulies, C. E. Felder, G. Melman, and A. Shanzer, "A Molecular Keypad Lock: a Photochemical Device Capable of Authorizing Password Entries," *Journal of the American Chemical Society*, vol. 129 (2), pp. 347-354, 2007.
- [56] R. S. Mathew-Fenn, R. Das, and P. A. B. Harbury, "Remeasuring the double helix," *Science*, vol. 322 (5900), pp. 446-449, 2008.
- [57] I. L. Medintz, A. R. Clapp, H. Mattoussi, E. R. Goldman, B. Fisher, and J. M. Mauro, "Self-assembled Nanoscale Biosensors Based on Quantum Dot FRET Donors," *Nature Materials*, vol. 2 (9), pp. 630-638, 2003.
- [58] Y. Ohya, K. Yabuki, M. Hashimoto, A. Nakajima, and T. Ouchi, "Multistep Fluorescence Resonance Energy Transfer in Sequential Chromophore Array Constructed on Oligo-DNA Assemblies," *Bioconjugate Chemistry*, vol. 14, pp. 1057-1066, 2003.
- [59] S. H. Park, C. Pistol, S. J. Ahn, J. H. Reif, A. R. Lebeck, C. Dwyer, and T. H. LaBean, "Finite-size, Fully-Addressable DNA Tile Lattices Formed by Hierarchical Assembly Procedures," *Angewandte Chemie*, vol. 45, pp. 735-739, 2006.
- [60] F. Patolsky, G. Zheng, O. Hayden, M. Lakadamyali, X. Zhuang, and C. M. Lieber, "Electrical Detection of Single Viruses," *Proceedings of the National Academy of Sciences*, vol. 101 (39), pp. 14017-14022, 2004.
- [61] J. P. Patwardhan, C. Dwyer, A. R. Lebeck, and D. J. Sorin, "NANA: a Nano-scale Active Network Architecture," *J. Emerg. Technol. Comput. Syst.*, vol. 2 (1), pp. 1-30, 2006.
- [62] J. P. Patwardhan, V. Johri, C. Dwyer, and A. R. Lebeck, "A Defect Tolerant Self-organizing Nanoscale SIMD Architecture," in *Proceedings of the 12th International Conference on Architectural Support for Programming Languages and Operating Systems*, pp. 241-251, 2006.
- [63] N. Peyret, P. A. Seneviratne, H. T. Allawi, and J. SantaLucia, "Nearest-Neighbor Thermodynamics and NMR of DNA Sequences with Internal A-A, C-C, G-G, and T-T Mismatches," *Biochemistry*, vol. 38 (12), pp. 3468-3477, 1999.
- [64] C. Pistol, A. R. Lebeck, and C. Dwyer, "Design Automation for DNA Self-Assembled Nanostructures," in *Proceedings of the 43rd Design Automation Conference (DAC)*, pp. 919 - 924, 2006.
- [65] C. Pistol and C. Dwyer, "Scalable, low-cost, hierarchical assembly of programmable DNA nanostructures," *Nanotechnology*, vol. 18, pp. 125305-9, 2007.

- [66] J. H. Reif, S. Sahu, and P. Yin, "Compact Error-resilient Computational DNA Tiling Assemblies," in *DNA Computing Selecture Notes in Computer Science*, vol. 3384, 2005, pp. 293-307.
- [67] D. Reishus, B. Shaw, Y. Brun, N. Chelyapov, and L. Adleman, "Self-assembly of DNA Double-double Crossover Complexes into Hiigh-density, Doubly Connected, Planar Structures," *Journal of the American Chemical Society*, vol. 127 (50), pp. 17590-17591, 2005.
- [68] F. Remacle, R. Weinkauff, and R. D. Levine, "Molecule-based Photonically Switched Half and Full Adder," *Journal of Physical Chemistry a*, vol. 110 (1), pp. 177-184, 2006.
- [69] R. L. Rich and D. G. Myszka, "Survey of the year 2001 commercial optical biosensor literature," *Journal of Molecular Recognition*, vol. 15 (6), pp. 352-376, 2002.
- [70] K. Rinaudo, L. Bleris, R. Maddamsetti, S. Subramanian, R. Weiss, and Y. Benenson, "A Universal Rnai-based Logic Evaluator That Operates in Mammalian Cells," *Nat Biotech*, vol. 25 (7), pp. 795-801, 2007.
- [71] P. W. K. Rothmund, "Design of DNA Origami," in *Proceedings of the IEEE/ACM International Conference on Computer Aided Design (ICCAD)*, pp. 471- 478, 2005.
- [72] P. W. K. Rothmund, "Folding DNA to create nanoscale shapes and patterns," *Nature*, vol. 440 (7082), pp. 297-302, 2006.
- [73] J. SantaLucia and D. Hicks, "The Thermodynamics of DNA Structural Motifs," *Annual Review of Biophysics and Biomolecular Structure*, vol. 33, pp. 415--440, 2004.
- [74] K. A. Schallhorn, K. O. Freedman, J. M. Moore, J. Lin, and P. C. Ke, "Single-molecule DNA Flexibility in the Presence of Base-pair Mismatch," *Applied Physics Letters*, vol. 87, pp. 033901, 2005.
- [75] G. Seelig, D. Soloveichik, D. Y. Zhang, and E. Winfree, "Enzyme-free Nucleic Acid Logic Circuits," *Science*, vol. 314 (5805), pp. 1585-1588, 2006.
- [76] N. C. Seeman, "Nucleic Acid Junctions and Lattices," *Journal of Theoretical Biology*, vol. 99, pp. 237-247, 1982.
- [77] N. C. Seeman, "De Novo Design of Sequences for Nucleic Acid Structural Engineering," *Biomolecular Structure & Dynamics*, vol. 8 (3), pp. 573-581, 1990.
- [78] N. C. Seeman, H. Wang, B. Liu, J. Qi, X. Li, X. Yang, F. Liu, W. Sun, Z. Shen, R. Sha, C. Mao, Y. Wang, S. Zhang, T. J. Fu, S. Du, J. E. Mueller, Y. Zhang, and J. Chen, "The Perils of Polynucleotides: The Experimental gap Between the Design and Assembly of Unusual DNA Structures," in *Proceedings of the Second International Meeting on DNA Based Computers (DNA2)*, pp. 191-205, 1996.
- [79] N. C. Seeman, "DNA Engineering and its Application to Nanotechnology," *Trends in Biotechnology*, vol. 17, pp. 437-443, 1999.

- [80] J. Sharma, R. Chhabra, Y. Liu, Y. G. Ke, and H. Yan, "DNA-templated Self-assembly of Two-dimensional and Periodical Gold," *Angewandte Chemie-international Edition*, vol. 45 (5), pp. 730-735, 2006.
- [81] J. Shi and D. E. Bergstrom, "Assembly of Novel DNA Cycles with Rigid Tetrahedral Linkers," *Angewandte Chemie International Edition*, vol. 36 (1-2), pp. 111-113, 1997.
- [82] M. R. Shortreed, S. B. Chang, D. Hong, M. Phillips, B. Campion, D. C. Tulpan, A. Condon, H. H. Hoos, and L. M. Smith, "A thermodynamic approach to designing structure-free combinatorial DNA word sets," *Nucleic Acids Research*, vol. 22 (15), pp. 4965-4977, 2005.
- [83] K. Skinner, R. L. Carrol, C. Dwyer, and S. Washburn, "Nanowire Transistors, Gate Electrodes, and Their Directed Self-Assembly," in *Proceedings of the 72nd Southeastern Section of the American Physical Society (SESAPS)*, pp. H2+, 2005.
- [84] D. Soloveichik and E. Winfree, "Complexity of Compact Proofreading for Self-assembled Patterns," in *DNA Computing Selecture Notes in Computer Science*, vol. 3892, 2006, pp. 305-324.
- [85] E. Stern, J. F. Klemic, D. A. Routenberg, P. N. Wyrembak, D. B. Turner-Evans, A. D. Hamilton, D. A. LaVan, T. M. Fahmy, and M. A. Reed, "Label-free immunodetection with CMOS-compatible semiconducting nanowires," *Nature*, vol. 445 (7127), pp. 519-552, 2007.
- [86] Stmicroelectronics, "ST6200C/ST6201C/ST6203C Datasheet," 2007.
- [87] L. Strekowski and B. Wilson, "Noncovalent interactions with DNA: An overview," *Mutation Research/Fundamental and Molecular Mechanisms of Mutagenesis*, vol. 623 (1-2), pp. 3-13, 2007.
- [88] L. Stryer and R. P. Haugland, "Energy Transfer: A Spectroscopic Ruler," *Proceedings of the National Academy of Sciences*, vol. 58, pp. 719-726, 1967.
- [89] M. Suzan-Monti, B. La Scola, and D. Raoult, "Genomic and evolutionary aspects of Mimivirus," *Virus Research*, vol. 1 (117), pp. 145-155, 2006.
- [90] R. Thomsen, P. S. Nielsen, and T. H. Jensen, "Dramatically Improved RNA in Situ Hybridization Signals Using Lna-modified Probes," *Rna-a Publication of the RNA Society*, vol. 11 (11), pp. 1745-1748, 2005.
- [91] H. Tian and Q.-C. Wang, "Recent progress on switchable rotaxanes," *Chem. Soc. Rev.* (35), pp. 361 - 374, 2006.
- [92] C. M. Tsai and C. E. Frasch, "A sensitive silver stain for detecting lipopolysaccharides in polyacrylamide gels," *Anal Biochem*, vol. 119 (1), pp. 115-119, 1982.
- [93] B. Valeur, *Molecular Fluorescence: Principles and Applications*. Weinheim: Wiley-VCH, 2002.

- [94] A. Valoczi, C. Hornyik, N. Varga, J. Burgyan, S. Kauppinen, and Z. Havelda, "Sensitive and Specific Detection of Micrnas by Northern Blot Analysis Using Lna-modified Oligonucleotide Probes," *Nucleic Acids Research*, vol. 32 (22 e175), pp. -, 2004.
- [95] T. Vo-Dinh, J. P. Alarie, N. Isola, D. Landis, A. L. Wintenberg, and M. N. Ericson, "DNA Biochip Using a Phototransistor Integrated Circuit," *Analytical Chemistry*, vol. 71 (2), pp. 358--363, 1999.
- [96] A. J. Wand, "Dynamic activation of protein function: A view emerging from NMR spectroscopy," *Nature Structural Biology*, vol. 8 (11), pp. 926-931, 2001.
- [97] W. U. Wang, C. Chen, K.-h. Lin, Y. Fang, and C. M. Lieber, "Label-free detection of small-molecule-protein interactions by using nanowire nanosensors," *Proceedings of the National Academy of Sciences*, vol. 102 (9), pp. 3208-3212, 2005.
- [98] X. Wang and W. M. Nau, "Kinetics of end-to-end collision in short single-stranded nucleic acids," *Journal of the American Chemical Society*, vol. 126, pp. 808-813, 2004.
- [99] P. C. Weber, D. H. Ohlendorf, J. J. Wendoloski, and F. R. Salemme, "Structural Origins of High-affinity Biotin Binding to Streptavidin," *Science*, vol. 243 (4887), pp. 85-88, 1989.
- [100] G. M. Whitesides and B. A. Grzybowski, "Self-Assembly at All Scales," *Science*, vol. 295, pp. 2418-2421, 2002.
- [101] M. N. Win and C. D. Smolke, "Higher-order Cellular Information Processing with Synthetic RNA Devices," *Science*, vol. 322 (5900), pp. 456--460, 2008.
- [102] E. Winfree, F. Liu, L. A. Wenzler, and N. C. Seeman, "Design and Self-Assembly of Two-Dimensional DNA Crystals," *Nature*, vol. 394, pp. 539-544, 1998.
- [103] E. Winfree and R. Bekbolatov, "Proofreading Tile Sets: Error Correction for Algorithmic Self-assembly," in *DNA Computing Lecture Notes in Computer Science*, vol. 2943, 2004, pp. 126-144.
- [104] Q.-H. Xu, S. Wang, D. Korystov, A. Mikhailovsky, G. C. Bazan, D. Moses, and A. J. Heeger, "The Fluorescence Resonance Energy Transfer (fret) Gate: a Time-resolved Study," *Proceedings of the National Academy of Sciences*, vol. 102 (3), pp. 530--535, 2005.
- [105] H. Yan, S. H. Park, G. Finkelstein, J. H. Reif, and T. H. LaBean, "DNA Templated Self-Assembly of Protein Arrays and Highly Conductive Nanowires," *Science*, vol. 301, pp. 1882-1884, 2003.
- [106] P. Yin, B. Guo, C. Belmore, W. Palmeri, E. Winfree, T. H. LaBean, and J. H. Reif, "TileSoft: Sequence optimization software for designing DNA secondary structures," in *Technical Report CS-2004-09, Dept. of Computer Science, Duke University*, 2004.
- [107] Y. Yokobayashi, R. Weiss, and F. H. Arnold, "Directed Evolution of a Genetic Circuit," *Proceedings of the National Academy of Sciences*, vol. 99, pp. 16587-16591, 2002.

- [108] B. Zhai, L. Nazhandali, J. Olson, A. Reeves, M. Minuth, R. Helfand, S. Pant, D. Blaauw, and T. Austin, "A 2.60pJ/inst Subthreshold Sensor Processor for Optimal Energy Efficiency," *VLSI Circuits, 2006. Digest of Technical Papers. 2006 Symposium on*, pp. 154--155, 2006.
- [109] T. Zhang, S. Mubeen, N. V. Myung, and M. A. Deshusses, "Recent Progress in Carbon Nanotube-based Gas Sensors," *Nanotechnology*, vol. 19 (33), 2008.
- [110] G. Zheng, F. Patolsky, Y. Cui, W. U. Wang, and C. M. Lieber, "Multiplexed electrical detection of cancer markers with nanowire sensor arrays," *Nat Biotech*, vol. 23 (10), 2005.
- [111] J. W. Zheng, P. E. Constantinou, C. Micheel, A. P. Alivisatos, R. A. Kiehl, and N. C. Seeman, "Two-dimensional Nanoparticle Arrays Show the Organizational Power of Robust DNA Motifs," *Nano Letters*, vol. 6 (7), pp. 1502-1504, 2006.

Biography

Constantin Pistol received his B.S. in Computer Science from University of Craiova, Romania, in 2004 and M.S. in Computer Science from Duke University in 2006. His research interests include computer architecture and the intersection of computer architecture and nanoscale computing systems. His PhD thesis explores system design for emerging computing technologies and in particular assembly methods, device technologies and architectural techniques for designing nanoscale sensor processors.

Publications

- [1] C. Pistol, W. Chongchitmate , C. Dwyer, A. R. Lebeck, “Architectural Implications of Nanoscale Integrated Sensing and Computing”, to appear in Fourteenth International Conference on Architectural Support for Programming Languages and Operating Systems (ASPLOS ‘09), pages 13-24, March 2009
- [2] C. Pistol, C. Dwyer, A. R. Lebeck, “Nanoscale Optical Computing using Resonance Energy Transfer Logic”, IEEE MICRO, pages 7-18, November/December, 2008
- [3] C. Pistol, C. Dwyer , “Scalable, Low-cost, Hierarchical Assembly of Programmable DNA Nanostructures”, IOP Nanotechnology, 18, 2007
- [4] C. Dwyer, A. R. Lebeck, C. Pistol, “Energy Transfer Logic on DNA Nanostructures: Enabling Molecular Scale Amorphous Computing”, 4th Workshop on Non-Silicon Computing (NSC-4), pages 33-40, June 2007
- [5] C. Pistol, C. Dwyer, A. R. Lebeck, “Design Automation for DNA Self-Assembled Nanostructures”, Proceedings of the 43rd Design Automation Conference (DAC), July, 2006
- [6] S. H. Park, C. Pistol, S. J. Ahn, J. H. Reif, A. R. Lebeck, C. Dwyer, T. H. LaBean, “Finite-size, Fully-Addressable DNA Tile Lattices Formed by Hierarchical Assembly Procedures”, Angewandte Chemie, Number 5/2006